

Local piezoelectric response and domain structures in ferroelectric thin films investigated by voltage-modulated force microscopy

Dissertation

Ph.D. thesis

Zur Erlangung des Akademischen Grades

to obtain the academic degree

doctor rerum naturalium (Dr. rer. nat.)

vorgelegt der

submitted to the

Mathematisch-Naturwissenschaftlich-Technischen Fakultät
(mathematisch-naturwissenschaftlicher Bereich)
Martin-Luther-Universität Halle Wittenberg

von

by

Catalin Harnagea

Gutachter:

1. Prof. Dr. Horst Beige
2. Prof. Dr. Ulrich Gösele
3. Prof. Dr. Lukas M. Eng

Halle (Saale), 04.05.2001

Table of contents

1. Introduction	3
2. Ferroelectricity and piezoelectricity	6
2.1 General	6
2.2 The piezoelectric effect in ferroelectric materials	7
2.3 Ferroelectric domains	10
3. Experimental.....	12
3.1 Basic principles of SFM.....	12
3.2 Probing ferroelectric domains by SFM	14
3.3 Piezoresponse-SFM setup	27
3.4 Investigated systems.....	30
4. Piezoresponse-SFM for local electromechanical probing of ferroelectric thin films.....	34
4.1 Analysis of the first harmonic signal in voltage modulated SFM.....	34
4.2 Imaging of the ferroelectric domain structure.....	37
4.3 Local measurements.....	38
5. Results.....	42
5.1 BaTiO ₃ single crystals – a verification of the method	42
5.2 New results on PZT films	47
5.3 Bismuth-layered perovskite thin films: Anisotropy of ferroelectricity.....	55
5.4 Patterned nanostructures	75
6. Discussion	83
6.1 The ferroelectric domain structure	83
6.2 Piezoelectric and ferroelectric hysteresis	86
6.3 Dependence of the local ferroelectric properties on the local crystallographic orientation	89
6.4 Size effect studies in ferroelectrics.....	91
7. Conclusions and outlook	95
Appendices.....	i
Appendix A: The method of the image charges applied to EFM of a dielectric layer with bottom electrode.....	i
Appendix B: Dependence of the piezoelectric coefficients on the testing directions	v
Appendix C: The effective piezoelectric coefficients in thin films – clamping by the substrate	viii
Appendix D: The matrix notation of the electromechanical coefficients	ix
References.....	x
Lebenslauf.....	xvii
Eidesstattliche Erklärung.....	xviii
Acknowledgement.....	xix

Abbreviations

2ME	2-methoxyethanol
BLSF(s)	Bismuth layer-structured ferroelectric(s)
CSD	Chemical solution deposition
EBDW	Electron beam direct writing
EFM	Electrostatic force microscopy
FeRAM	Ferroelectric random access memory
PZT	$\text{Pb}(\text{Zr}_x\text{Ti}_{1-x})\text{O}_3$
PLD	Pulsed laser deposition
RAM	Random access memory
STO	SrTiO_3
SBT	$\text{SrBi}_2\text{Ta}_2\text{O}_9$
SEM	Scanning electron microscopy
SFM	Scanning force microscopy
SPM	Scanning probe microscopy
TEM	Transmission electron microscopy
XRD	X-ray diffraction
YSZ	Yttria-stabilized zirconia

1. Introduction

Ferroelectric materials gradually enter into the design of microelectronic devices. The ability to increase the packing density of the ferroelectric structures and thus the capabilities of the device is primarily limited by the possibilities to manufacture very small structures in a controlled way, but also by the fact that such tiny ferroelectric structures may not preserve their macroscopic properties at this scale. Recently, the interest in finding a better alternative for random access memories (RAMs) in personal computers has pointed towards non-volatile ferroelectric RAMs (FeRAMs). The new devices should satisfy at least the present requirements for dielectric RAMs (DRAMs), plus non-volatility, a property that will save both energy and time, since the constant need of refreshing the memory state (as it is the case in nowadays DRAMs) disappear. On the more practical side, time will also be saved, as the lengthy transfer of information from the long-time mass storage devices to the dynamic memory (such as the initial boot of a computer after switching on, for instance) will vanish as well.

To compete with DRAMs, the lateral size of an individual non-volatile ferroelectric memory cell should be in the mesoscopic range, i.e. less than 100 nm. It is therefore necessary to understand and to control the processes that lead to a deterioration of the prospected performance of ferroelectric structures having such a small size. Presently, however, the understanding of the ferroelectric phenomena at these sizes is by far not complete and needs to be improved, as it can also be seen from the numerous publications in this field during the last decade.

Taking this into account, the scope of the research presented was to study ferroelectric phenomena on a local scale for different materials in view of their prospective use in non-volatile memories.

A summary of the fundamental elements of ferroelectric and piezoelectric phenomena needed to understand the principle of the experimental technique and the interpretation of the results is presented in Chapter 2.

Special attention has been paid to the description of the experimental technique used to achieve the scope of the present work. The method used for the study of the local ferroelectric behavior is the so-called “piezoresponse SFM”, a scanning probe technique based on the converse piezoelectric effect that is present in all ferroelectric materials. This technique allows both the detection and the modification of the ferroelectric state, using the same experimental setup, with a resolution down to 10 nm.

As it is at the heart of the experimental setup, the operating principles of a scanning force microscope (SFM) are reviewed in details in Chapter 3. A short review of the previous experiments and SFM-methods to image ferroelectric domains is also provided in order to put the problem in perspective and to demonstrate that the method chosen is the most suitable under the given circumstances, namely the necessity of imaging and modifying the ferroelectric state.

A separate chapter (Chapter 4) is dedicated to an extensive discussion of the possibilities that this technique provides to probe the local ferroelectric properties. For this purpose a careful analysis of the signals involved in the measuring process was included into Chapter 4. In particular, while various voltage modulated scanning force microscopy techniques are gaining in popularity for ferroelectric imaging, they are usually restricted to image displacements normal to the surface. By using the relatively new capability of imaging shear displacements in SFM, the concept of in-plane domain imaging has been developed. This mode enables to image displacements in the plane of the ferroelectric film surface, and therefore to extend the capabilities of piezoresponse SFM to ferroelectric domains whose polarization is oriented in the plane of the film.

The experimental results and a specific discussion of each of them are presented in Chapter 5. First, the capabilities of the experimental system were tested using barium titanate single crystals, whose properties are well known from the literature, both from macroscopic and microscopic characterization. The good agreement between the local measurements of single crystalline BaTiO₃ by piezoresponse SFM and the known published properties is an explicit confirmation of the correct operation of the setup, and therefore an overall validation of the experimental method.

Using this setup, ferroelectricity was then locally investigated on a series of ferroelectric thin films and structures of decreasing size:

1. First, continuous films of lead zirconate-titanate (PZT), one of the most frequently used ferroelectric material for device applications, were investigated. The polycrystalline PZT films consist of randomly oriented grains with sizes in the 100 nm to 600 nm range. The thickness of the films is in the same range, viz. 200 nm up to 600 nm.

2. Then, Individual protruding grains of various bismuth layer structured ferroelectrics (BLSFs) were investigated, a relatively new class of ferroelectric materials that feature a high endurance to switching fatigue, and a complex and highly anisotropic layer structure similar to that of the high-temperature superconductors. These materials are also called bismuth-layered perovskites or sometimes Aurivillius phases (after Bengt Aurivillius, the Swedish scientist that discovered and first studied them). These individual ferroelectric grains were part of epitaxial films with a mixed orientation; i.e. they consisted of individual protruding non-c-oriented grains embedded into a c-oriented matrix. The size of the non-c-oriented grains happens to be in the mesoscopic range (hundreds of nanometers) and is therefore well suited for this study. Also, due to the high anisotropy of the BLSFs, they provided a unique system to study the effects of the anisotropy on the ferroelectric properties and the dependence of the latter on the crystallographic orientation.

3. Finally, ordered periodic arrays of fine-grained individual ferroelectric structures having lateral sizes ranging from 1 μm down to 100 nm, were investigated. On these ordered arrays of mesoscopic structures, both fundamental problems, such as the possible disappearance of ferroelectricity below a critical size and more generally the dependence of the ferroelectric properties on the lateral size, as well as problems of high practical and technical relevance, such as cross-talk between adjacent structures, were addressed.

A more general discussion of the results obtained is provided in chapter 6, where different problems common to all of them are presented. Since sizes of the smallest mesoscopic structures investigated were approaching the experimental resolution limit, a discussion of the limitations of the method as well as of potential improvements is also included.

2. Ferroelectricity and piezoelectricity

2.1 General

Ferroelectrics are polar materials that possess at least two equilibrium orientations of the spontaneous polarization vector in the absence of an external electric field, and in which the polarization may be switched between those orientations by means of an electric field. The electric displacement takes the form (using the Einstein summation convention):

$$D_i = \varepsilon_0 E_i + P_i = \varepsilon_0 E_i + \varepsilon_0 \chi_{ij} E_j + P_{Si} = \varepsilon_{ij} E_j + P_{Si} \quad \text{Eq. 1}$$

where χ_{ij} is tensor of the susceptibilities, ε_{ij} is the linear dielectric tensor and P and P_S are the total and spontaneous ferroelectric polarization, respectively. Most ferroelectric materials undergo a structural phase transition from a high-temperature nonferroelectric (or paraelectric) phase into a low-temperature ferroelectric phase, of a lower crystal symmetry. The phase transition temperature is usually called the Curie point (T_c). In most cases, the dielectric constant above this temperature obeys the Curie-Weiss law: $\varepsilon = C(T - T_0)^{-1}$, where C is the Curie constant and T_0 the Curie temperature*.

Using a thermodynamic approach, it is possible to describe the important features of ferroelectric materials without taking into account the microscopic mechanisms of ferroelectricity. In this way, starting from the symmetry of the paraelectric phase**, it is possible to deduce the stable ferroelectric phase(s), the possible orientations of the polarization, and even to predict the possible orientations of domain walls inside the crystal in the ferroelectric phase^[1,2,3]. From the basic thermodynamic relations it follows that the stable phase under a given set of independent variables is the one which minimizes the corresponding free energy^[4]. Expressions that relate dependent and independent variables may be obtained using the usual thermodynamic formalism. Under isothermal conditions, with the electric displacement D , the elastic stress X , and the temperature T as independent variables, which is the situation in most of the experimental cases, the *elastic Gibbs free energy* function should be used^[3,5]:

$$G_1(T, X, D) = U - TS - X_{ij} x_{ij} \quad \text{and} \quad dG_1 = -SdT - x_{ij} dX_{ij} + E_i dD_i \quad \text{Eq. 2}$$

For small changes in D , X and T , the elastic Gibbs free energy can be expanded into a Taylor series around the equilibrium state $G_{10}(T)$ (in which $D = 0$, and $X = 0$), in terms of the independent variables T , X and D . Usually, the elastic Gibbs free energy is expressed with respect to the energy of the paraelectric state which is considered to be nonpolar, assuming that the same analytical function describes both the paraelectric and ferroelectric phases^[5].

* In the case of first order phase transitions the Curie point and the Curie temperature do not coincide. For more details, see Ref. 5.

** If a paraelectric phase does not exist, the higher symmetry prototype (from which the ferroelectric modification is derived) is used.

$$\begin{aligned}
 G_1(T, X, E) - G_{10}(T, X, E) = & \frac{\partial G_1}{\partial T} \Delta T + \frac{\partial G_1}{\partial D_i} D_i + \frac{\partial G_1}{\partial X_{ij}} X_{ij} + \frac{1}{2} \frac{\partial^2 G_1}{\partial T^2} \Delta T^2 + \\
 & + \frac{1}{2} \frac{\partial^2 G_1}{\partial D_i \partial D_j} D_i D_j + \frac{1}{2} \frac{\partial^2 G_1}{\partial X_{ij} \partial X_{kl}} X_{ij} X_{kl} + \frac{\partial^2 G_1}{\partial T \partial D_i} \Delta T D_i + \frac{\partial^2 G_1}{\partial D_i \partial X_{kl}} D_i X_{kl} + \\
 & + \frac{\partial^2 G_1}{\partial T \partial X_{kl}} \Delta T X_{kl} + \dots \text{higher order terms}
 \end{aligned} \quad \text{Eq. 3}$$

Each of the partial derivatives of the elastic Gibbs free energy (coefficients in the Taylor expansion) identifies a physical effect ^[6]. For instance, $g_{ijk} = (\partial^2 G_1 / \partial X_{ij} \partial D_k)$ is denominated strain- or voltage-related piezoelectric coefficient. Also, coefficients in the Taylor expansion transform as components of the associated tensor. For example, the piezoelectric coefficients like g_{ijk} transform as third-rank tensors when changing the system of coordinates. In most ferroelectric materials of interest the paraelectric phase is centrosymmetric, implying that all coefficients associated with odd-rank tensors are zero. This significantly reduces the number of terms that must be considered in Eq. 3. In the case of the elasto-electric coupling (piezoelectric effects), this means that all the piezoelectric coefficients derived from the linear terms (as g_{ijk} above) are zero. Since the terms in the expansion represent correction terms, it is usually sufficient to expand the elastic free energy up to the fourth- or sixth-order terms.

Finally, a stable state of the system under the conditions of fixed temperature, stress and electric field is obtained when the elastic Gibbs free energy G_1 is minimal.

$$G = G_1 - \vec{E} \cdot \vec{D} \quad \text{Eq. 4}$$

This is the starting point that allows the deduction of all main features of a ferroelectric system. Imposing the first derivative of Eq. 4 to be zero (conditions of stability) results in a set of equations that yield the polarization and the strains developed in a ferroelectric by a set of boundary conditions and external fields.

2.2 The piezoelectric effect in ferroelectric materials

“Piezo” originates from the Greek word *piezein*, meaning to press or to squeeze. In 1880, the Curie brothers found that quartz changed its dimensions when subjected to an electric field and conversely generated an electric charge when it was pressed.

Piezoelectric materials are a class of materials that can be polarized by applying a mechanical stress or an electric field. The class of the piezoelectric materials includes ferroelectrics. The direct piezoelectric effect is equivalent to the appearance of charges when the material is subject to a stress ^[7]. It is described by a linear relationship between the stress X_{ik} applied to a piezoelectric material and the resulting charge density D_i :

$$D_i = d_{ijk}^{\text{direct}} X_{jk}$$

where d_{ijk} is the third-rank tensor of piezoelectric coefficients, measured in [C/N].

Also the reverse effect is always present: Piezoelectric materials change their dimensions (they contract or expand) when subject to an electric field ^[7]. The converse piezoelectric effect is described by a linear relationship between the strain x_{ij} developed in a piezoelectric material and the applied electric field E_k :

$$x_{ij} = d_{kij}^{\text{converse}} E_k = (d_{ijk}^{\text{direct}})^t E_k$$

where t denotes the transposed “matrix”. The unit of the converse piezoelectric coefficient is [m/V]. The piezoelectric coefficients for the direct and converse piezoelectric effects are thermodynamically identical i.e. $d^{converse} = d^{direct}$. Because the strain and the stress are symmetrical tensors, the tensor of the piezoelectric coefficients is symmetrical with respect to the corresponding indices, $d_{ijk} = d_{ikj}$. The number of independent piezoelectric coefficients is thus reduced from 27 to 18. The number of independent elements of d_{ijk} may be further reduced by the symmetry of the material.

The piezoelectric coefficient measured in the direction of the applied field is usually called the *longitudinal* coefficient, and that measured in the direction perpendicular to the field is known as the *transverse* coefficient [7]. Other piezoelectric coefficients are denominated shear coefficients. It is worth mentioning that the piezoelectric coefficient d can be either positive or negative. Using the usual thermodynamic formalism (like the one described in the previous section), depending on the set of independent variables chosen, four sets of isothermal piezoelectric constitutive equations can be obtained (for the matrix notation used, see Appendix D):

$$\begin{cases} D_i = d_{im}^{T,E} X_m + \varepsilon_{ij}^{T,X} E_j \\ x_m = s_{mn}^{T,E} X_n + d_{im}^{T,X} E_i \end{cases} \quad \text{Eq. 5a}$$

$$\begin{cases} D_i = e_{im}^{T,E} X_m + \varepsilon_{ij}^{T,x} E_j \\ X_m = c_{mn}^{T,E} x_n - e_{im}^{T,x} E_i \end{cases} \quad \text{Eq. 5b}$$

$$\begin{cases} E_i = -h_{im}^{T,D} x_m + \beta_{ij}^{T,x} D_j \\ X_m = c_{mn}^{T,D} x_n - h_{im}^{T,x} D_i \end{cases} \quad \text{Eq. 5c}$$

$$\begin{cases} E_i = -g_{im}^{T,D} X_m + \beta_{ij}^{T,X} D_j \\ x_m = s_{mn}^{T,D} X_n + g_{im}^{T,X} D_i \end{cases} \quad \text{Eq. 5d}$$

The four types of coefficients are denominated as follows: d is either charge or strain coefficient, e is either charge or stress coefficient, h is either voltage or stress coefficient, and g is either voltage or strain coefficient [8], depending on the physical quantity that is calculated. For simplicity, d and g are usually called piezoelectric strain-coefficients, and e and h are called piezoelectric stress-coefficients [9]. The superscripts of the coefficients in Eq. 5 indicate the variables held constant during the partial derivation of the thermodynamic potential. The coefficients are mutually related by:

$$d_{im} = e_{in} s_{nm}^E = \varepsilon_{ij}^X g_{jm} \quad [m/V] \text{ or } [C/N] \quad \text{Eq. 6a}$$

$$e_{im} = d_{in} c_{nm}^E = \varepsilon_{ij}^x h_{jm} \quad [C/m^2] \text{ or } [V/N] \quad \text{Eq. 6b}$$

$$g_{im} = h_{in} s_{nm}^D = \beta_{ij}^X d_{jm} \quad [m^2/C] \text{ or } [N/V] \quad \text{Eq. 6c}$$

$$h_{im} = g_{in} c_{nm}^D = \beta_{ij}^x e_{jm} \quad [N/C] \text{ or } [V/m] \quad \text{Eq. 6d}$$

It is of practical interest to relate the piezoelectric coefficients to the spontaneous polarization. As already mentioned, if the paraelectric phase is centrosymmetric, then the resulting linear piezoelectric coefficients are zero. Because ferroelectrics are nonlinear

materials, higher order terms have to be taken into account in Eq. 3. The first term (with non-zero coefficient) that includes the elastic-electric coupling is the electrostrictive term, which for $E = 0$ takes the form:

$$\Delta G_1^{estr} = Q_{ijkl} X_{ij} P_{Sk} P_{Sl} \quad \text{Eq. 7}$$

where Q_{ijkl} are the polarization-related electrostrictive coefficients, components of the fourth rank electrostrictive tensor. First, this term implies that in ferroelectric materials the existence of the spontaneous polarization \mathbf{P}_S is always associated to a spontaneous strain x_S . This results from the differential form of Eq. 2 (containing the electrostrictive term) and the condition of stability $dG_I = 0$:

$$x_{Sij} = \left(\frac{\partial G_1}{\partial X_{ij}} \right) = Q_{ijkl} P_{Sk} P_{Sl} \quad \text{Eq. 8}$$

The spontaneous strain plays an important role in the process of the formation of stable ferroelectric domains and also in their switching.

If we now consider the (electrostrictive) spontaneous strain in Eq. 8 as a piezoelectric strain, it follows (index m in matrix notation):

$$x_m = \left(\frac{\partial G_1}{\partial X_m} \right) = Q_{mkl} P_{Sk} P_{Sl}$$

From Eq. 5d in the case of $X = 0$ and $E = 0$ we obtain:

$$g_{im} = \left(\frac{\partial E_i}{\partial X_m} \right) = \left(\frac{\partial^2 G_1}{\partial X_m \partial P_i} \right) = \frac{\partial}{\partial P_i} \left(\frac{\partial G_1}{\partial X_m} \right) = 2Q_{mik} P_{Sk}$$

Inserting g_{im} in Eq. 6a, it follows that:

$$d_{im} = \varepsilon_{ij} Q_{mjk} P_{Sk} \quad \text{Eq. 9}$$

In the particular case of the tetragonal symmetry (axis “3” is the polar axis), Eq. 9 reduces to* (as also deduced by Devonshire for barium titanate^[10]):

$$d_{33} = 2\varepsilon_{33} Q_{33} P_{S3} \quad \text{Eq. 10a}$$

$$d_{31} = 2\varepsilon_{33} Q_{13} P_{S3} \quad \text{Eq. 10b}$$

$$d_{15} = 2\varepsilon_{11} Q_{44} P_{S3} \quad \text{Eq. 10c}$$

It should be kept in mind that all the above statements are valid only for a ferroelectric single crystal in the monodomain state. This hypothesis is underlying the thermodynamic approach, and was set when the possible orientations of spontaneous polarization were established.

* The symmetry imposes $P_{S1} = P_{S2} = 0$, $\varepsilon_{11} = \varepsilon_{22}$, $\varepsilon_{ij} = 0$ for $i \neq j$, and the only non-zero electrostrictive coefficients are $Q_{11} = Q_{22}$, $Q_{12} = Q_{21}$, $Q_{13} = Q_{23}$, $Q_{31} = Q_{32}$, Q_{33} , $Q_{44} = Q_{55}$, Q_{66} .

2.3 Ferroelectric domains

In the absence of an external force, the direction of the spontaneous polarization in an ideal ferroelectric crystal can arise with equal probability along several crystallographic directions of the prototype (paraelectric) phase. Accordingly, after the transition to a ferroelectric state the crystal breaks up into separate regions that differ in the direction of the spontaneous polarization. The regions of the crystal with uniformly oriented spontaneous polarization are called ferroelectric domains. The region between two domains is called a domain wall. Domain walls that separate different orientations of the spontaneous polarization vector are called ferroelectric domain walls and those which separate different orientations of the spontaneous strain are called ferroelastic domain walls.

Ferroelectric domains form to minimize the electrostatic energy of the depolarizing fields and the elastic energy associated with mechanical constraints to which the ferroelectric material is subjected during the transition from the paraelectric to the ferroelectric phase. Depolarizing fields develop whenever a nonhomogeneous distribution of the spontaneous polarization appears, for instance, during the formation of the ferroelectric phase. Also, the fall-off of the polarization at a grain boundary usually causes strong depolarizing fields of the order of 10 kV/cm. Due to these high values, the depolarizing fields cause the single-domain state of a ferroelectric to be energetically unfavorable. As a consequence, the electrostatic energy associated is minimized by splitting the ferroelectric into domains with opposite polarization. Alternatively, the charges associated with the depolarizing fields may be neutralized by conduction of free charges through the crystal or coming from the surrounding of the material.

Regarding the domain formation, Fousek and Janovec^[2] have established a criterion to predict the possible domain wall orientations between two allowed polarization directions in a perfect infinite single crystal:

- During the transition to the polarized state, the crystal distorts. This distortion can be predicted from the magnitude and direction of the spontaneous polarization, and from the piezoelectric and electrostrictive coefficients in the paraelectric phase.
- Two domains having different orientations of the spontaneous polarization will have a common domain wall only along the planes for which the two distortions of the lattice match exactly. These planes are therefore possible domain walls for the crystal.

Another condition that should be fulfilled at the domain wall is the *electric neutrality*. Unless the crystal is conductive, the normal component of the spontaneous polarization should be continuous through the domain wall; otherwise, the electrostatic energy will make it very unstable.

The domain structure that develops in single crystal perovskites is well known. The spontaneous polarization can be oriented only along three mutually perpendicular crystallographic directions (in the tetragonal phase). This gives rise to two types of domain walls: walls that separate domains with oppositely oriented polarization (called *180°-walls*), and those which separate regions with mutually perpendicular polarization (called *90°-walls*). The *90°-walls* are both ferroelectric and ferroelastic domain walls, because they separate regions with different orientation of the polarization and of the strain.

The application of the above criteria applied to tetragonal perovskites shows that the 180° domain walls can be any cylindrical surface separating regions with the spontaneous polarization parallel to the polar axis. No other restrictions are limiting their position or orientation. The allowed 90° domain walls are parallel to the $\{110\}_{\text{tet}}$ family of crystal planes. The continuity of the normal component of the spontaneous polarization results in the so-called head-to-tail configuration, as depicted in Figure 1.

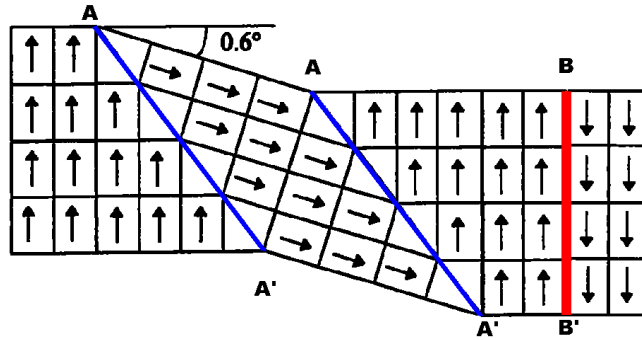


Figure 1 Ferroelectric domain walls in a perovskite ferroelectric. A-A' lines represent 90° domain walls, and the B-B' line a 180° domain wall (the tetragonality is highly exaggerated).

The ferroelectric domain structure is the most important factor that determines the ferroelectric properties of a ferroelectric material, together with domain nucleation and domain wall mobility. The way how the material splits up into domains at the formation of the ferroelectric phase depends very much on the mechanical and electrical boundary conditions imposed on the sample, as well as on the nature of the sample itself.

3. Experimental

3.1 Basic principles of SFM

3.1.1 Operating principle

The operation principle of a scanning probe microscope (SPM) is based on the detection of the position of a soft cantilever-type spring with a sharp tip mounted at its end. The forces acting on the tip after it has approached the sample surface cause a deflection of the cantilever according, in a first approximation, to the Hooke's law. This bending is controlled by a feedback loop, which regulates the vertical position of the tip with respect to the sample surface. By keeping the deflection constant while scanning the sample, a three-dimensional map of the surface topography can be obtained.

Usually, as shown in Figure 2, the vertical tip position is read using a laser beam, which is reflected by the end of the cantilever and detected using a differential optical converter. The arrows in Figure 2 emphasize the “trajectory” of the feedback loop: SFM tip, laser beam, detector, controller, Z scanner and sample. The key point of the system is the fact that the feedback loop contains the “tip-sample interaction” element.

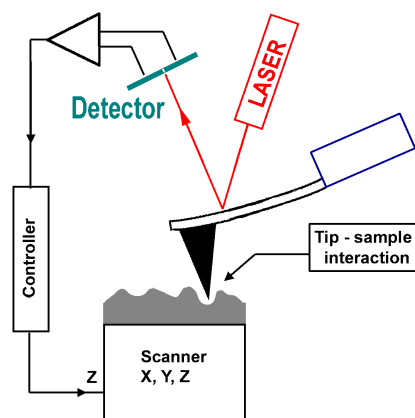


Figure 2 Principle of the SPM-based techniques.

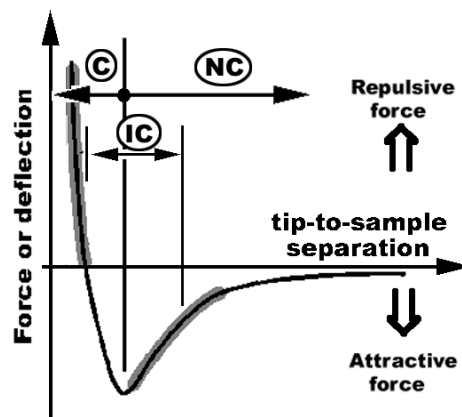


Figure 3 Force versus tip-sample separation. “C”, “NC”, and “IC” denote the contact, non-contact, and intermittent contact regions of the curve.

There are two main modes of operation that determine the type of interaction between the SFM tip and the sample: contact and non-contact. In contact mode, the probing tip senses the short-range repulsive forces exerted by the surface. The interaction between tip and sample can be estimated plotting the cantilever deflection against the elevation above the surface of the Z scanner, the so-called *force–distance* curve. The shape of a typical force curve is shown in Figure 3. A tip approaching the surface first senses the long-range forces. This region of the curve is used in non-contact mode imaging. The forces are usually Van der Waals forces, but any other type of interaction between the SPM tip and the surface of the sample should be

included, depending on the given tip and sample. For instance, if the SPM tip has a magnetic moment, the long-range attractive and repulsive magnetic forces are sensed and the magnetic domain structure at the surface can be visualized. Further approaching the tip, the interaction force becomes repulsive and the cantilever is deflected in the opposite direction. This region is used in the contact mode technique.

Another important type of measurement used in this work is directly related to the detection of lateral forces acting on the SPM tip. In principle, this is done in the contact mode of operation. With the lateral force technique, the probe is scanned perpendicularly to the long axis of the cantilever. The torsion of the cantilever supporting the probe will increase or decrease, depending on the frictional characteristics of the surface (a greater torsion results from an increased friction).

3.1.2 Topography imaging with SFM

As mentioned above, to image the topography of a sample the tiny forces between a sharp tip and the sample surface are utilized. In contact mode (cf. Figure 3), the tip elevation is adjusted via the feedback loop in order to follow the surface height using the deflection signal, which is in fact the cantilever bending caused by repulsive forces.

For example let us suppose that the tip is scanned at a constant altitude above a flat surface. The tip being in contact, there is always a repulsive force that bends the cantilever, with a constant value called “setpoint”. If there are no variations in the cantilever bending, the tip is scanned at the same altitude, and the tip height representing the topographic data render a flat surface. If the tip arrives at a protuberance of the surface, the cantilever feels a higher contact force and bends more than before. The deflection signal increases, and as a consequence, the feedback controller raises up the tip until the deflection signal equals the setpoint again. If the tip encounters a pit during its scan then the feedback process will lower the tip elevation because the contact force (and therefore the deflection signal) is decreased in this case. The elevation of the tip therefore reflects the surface topography and is used to image it. In fact the principle explained above is used for imaging in all modes of operation.

In the non-contact mode, the tip feels the attractive forces exerted by the surface and the setpoint value in this case represents a bending in the opposite direction than in the repulsive mode. If the tip meets a surface protrusion, the attractive force increases and the feedback control system raises up the tip until the attractive force takes the setpoint value. This mode of operation is quite difficult to achieve, and very easy to destabilize. The amount of force available to be used is much smaller than in the repulsive mode (see Figure 3).

The operating modes described up to now were static. In the dynamic modes the same principle is used, but the signal that is monitored by the feedback loop is the amplitude of the cantilever vibration, induced mechanically with a piezoelectric oscillator (at the cantilever resonance for a maximum sensitivity).

In the dynamic non-contact mode the amplitude of the cantilever oscillation increases if the surface has an elevation and the feedback control adjusts the tip elevation until the amplitude reaches the setpoint value again. This mode is an improvement of the non-contact static mode, with an increased sensitivity.

Another mode of topographic imaging is the intermittent-contact mode (also called “tapping” mode), which is an improvement of the contact mode, developed to decrease the

interaction of the tip with the surface. The cantilever with the tip is oscillated at its resonance frequency and the height is adjusted so that the tip touches the sample surface only for a short period of time. If the tip encounters an elevation, the oscillation amplitude will decrease and the feedback control raises up the cantilever until the oscillation amplitude reaches the initial value.

3.2 Probing ferroelectric domains by SFM

SFM-based methods of ferroelectric domain imaging make use of basic properties of ferroelectrics, namely of their elastic or piezoelectric behavior and/or of the presence of surface charges, associated with the permanent built-in electric polarization. In very specific cases, the topography caused by the domain structure is sufficient to deduce the direction of the spontaneous polarization. A static surface charge, proportional to the normal component of the polarization, can be detected when the microscope is operated in the non-contact (attractive) mode. By monitoring the piezoelectric vibration of the ferroelectric sample caused by an external AC voltage, the domain structure can be visualized in the SFM piezoresponse mode, when the probing tip is in contact with the sample.

3.2.1 Domain imaging with SFM contact and non-contact static modes

Before explaining the proper domain imaging modes, the historically first attempts to investigate domains with SFM should be reviewed. These techniques are termed “static” because no dynamic interaction (mechanic or electrostatic) between the SFM probing tip and the ferroelectric domains is involved during the imaging process. True atomic resolution was achieved on flat surfaces of different materials^[11], even under ambient conditions^[12].

Domain imaging in the topography mode

Morphological domain contrast can result as a consequence of different phenomena, according to the specific material properties. Topographic features of the sample surface can be imaged either in contact or in non-contact mode, the interpretation of the domain images does not depend on the type of interaction used to obtain the topographic information. Therefore the results considered in this section were obtained either in contact, non-contact or intermittent contact modes of operation. The very high vertical resolution of SFM proved to be useful to investigate the surface morphology and to relate it to the ferroelectric domain structure. It should be mentioned that true atomic resolution was achieved in the topography mode at the surface of ferroelectric crystals^[13,35].

A particular example is the case of triglycine sulfate (TGS), which is one of the most frequently studied ferroelectric crystals. It was shown that steps form at domain boundaries during the crystal cleavage due to the structural difference between the positively and negatively charged ends of the domains^[14,15,16]. Bluhm et al.^[15,16], using the SFM topography mode, have found that the step height is different on the opposite cleavage faces. The difference was explained by the different relative shift of atom positions at the surface of opposite domains. Due to the different etching behavior of positive and negative domains in TGS^[17] topographic imaging of this crystal was used for the identification of the domain polarity in a number of studies^[14,18,19,20,21]. In the case of the TGS crystal, the cleavage plane is perpendicular to the polar axis, therefore the imaged surface was thought to interact

electrostatically with the conductive or non-conductive SFM tip. However, ferroelectric domains have been imaged even if the cleavage plane of the crystal is parallel to the polar axis, as in the case of K_2ZnCl_4 [22]. In the latter case, the topographic contrast was proven to be due solely to the transverse piezoelectric deformation of the ferroelectric domains.

In case of the tetragonal phase of perovskite ferroelectrics, the polarization vector can be aligned along six directions, which are equivalent in the cubic paraelectric phase. Along the polarization direction the unit cell is slightly elongated leading to the tetragonal distortion of the unit cell. In a (001) single crystal plate, the domains with the polarization perpendicular to the plane of the plate are called *c*-domains and the domains with the polarization in the plane of the plate are called *a*-domains. In the regions between the *a*- and *c*-domains (the so-called 90° domain walls) the tetragonality causes a distortion of the lattice, which results in a tilt angle between the surfaces of the two domains. Figure 1 shows a schematic cross-section view of such a plate containing *a*- and *c*-domains. The tilt angle between the surfaces of the two types of domains can be estimated from the tetragonal distortion as $\theta = 2\arctg(c/a) - 90^\circ \approx 0.6^\circ$. This allows the deduction of the domain structure of ferroelectric perovskites from the topography of the crystal surface, taking into account the criteria presented in Sect. 2.3. Using these assumptions, domain structures were successfully deduced and analyzed from SFM topographic images in $BaTiO_3$ [23,24,25], $PbTiO_3$ [26,27] crystals and also in $PbTiO_3$ ceramic [28] and epitaxial PZT (20/80) thin films [29]. Also, by applying pulse voltages to the SFM tip while scanning in contact mode, the domain structure could be modified by means of nucleation and growth of opposite *c*-domains [30,31,32]. In these studies it was necessary to mount the ferroelectric crystal on an electrode in order to apply electric fields to the sample. The observation of different *c*-domains using the topography mode of SFM was possible *via* static piezoelectric deformation caused by the application of a small DC voltage between the tip and a bottom electrode.

Domain imaging in the friction mode

It was assumed that ferroelectric domains may induce a lateral force contrast *via* electrostatic tip-sample interaction. During the movement of a non-conducting tip across the ferroelectric sample surface, a certain amount of charges accumulates [31] or an electric dipole forms [33] on the probing tip. The moving charged tip senses different lateral forces above ferroelectric domains with opposite orientations. The same experiment performed with a grounded conducting tip (which does not retain any charge) did not reveal any domain contrast. As a consequence, it was thought that this proves the electrostatic nature of the interaction. The observed reversal of domain contrast for opposite scanning directions [19] supported the tribological effect to be present in the imaging mechanism.

Later on, however, it appeared that the ferroelectric domains can more likely induce a lateral force contrast due to the structural differences of the surfaces of oppositely polarized domains [34]. Bluhm et al. demonstrated for both guanidinium aluminum sulfate hexahydrate (GASH) and TGS crystals that the domain contrast in friction mode is not governed by electrostatic interaction between the tip and the surfaces. For the GASH surface, they found indeed a reversal of the domain contrast for forward and backward scan directions, but the magnitude of friction forces did not show opposite signs for opposite scanning directions, as it should. For the case of TGS, the results were more difficult to interpret, since the lateral force was found to be highly anisotropic, i.e. a strong dependence of the domain pattern on the

scanning angle was found. Moreover, if the electrostatic interaction would be responsible for the domain contrast, then the latter should reverse when the surface is scanned first with positive and then with negative voltages applied to the tip. In the experiments performed in inert atmosphere switching the voltage from -10V to $+10\text{V}$ resulted only in a change of the offset of the friction signal. Therefore, even if the electrostatic interaction cannot be completely ruled out, it does not entirely explain the mechanism of domain contrast in the friction mode of SFM.

It should also be noted that SFM friction imaging is a technique very sensitive to the properties of the tip-to-sample interface and therefore special care has to be taken when interpreting the tribological contrast as revealing ferroelectric domains. Adhesion layers, wetting, contamination, interfacial and surface chemistry can easily obscure the electrostatic interaction. The method works very well on freshly cleaved surfaces, if the cleavage plane is perpendicular to the polar axis. This is the case for GASH and TGS for which this method, although controversial, was successful^[35]. A comparative characterization of the *a*- and *c*-domains in epitaxial PbTiO_3 and BaTiO_3 thin films on MgO (100) substrates was also possible, revealing the smaller transformation strain and larger compressive stress in BaTiO_3 at the Curie temperature^[36].

In conclusion, it should be emphasized that there are obvious limitations on the applicability of the SFM topographic and friction modes for the imaging of ferroelectric domains. These methods can be applied only for crystals with cleavage planes, since any treatment of the surface during sample preparation inevitably eliminates the subnanometer structure of morphological steps associated with the ferroelectric domain structure. Also, domain imaging by inducing static piezoelectric strain with a DC voltage is almost impossible to perform if the surface has a roughness of several nanometers, comparable with the deformation induced by a reasonable DC voltage of 10 V.

3.2.2 SFM dynamic non-contact modes

As mentioned in Sect. 3.1.1, the SFM system can probe not only the surface topography, but any type of interaction between the SFM tip and the sample. Since the feedback loop keeps the amplitude of the cantilever oscillation constant, any modification of the interaction force will lead to a variation of both the feedback and output signals. Therefore, if a non-topography-related interaction is governing the feedback loop, the topography can not be monitored anymore, but only the sources of the probed interaction. This inconvenience is usually ruled out simply, by scanning over the same line twice, with two different feedback signals, one dominated by the topography and the other by the non-topographic interaction. In the case of ferroelectric domain imaging, the electrostatic interaction between the probing tip and the electric field at the sample surface controls the feedback loop.

Domain imaging in the dynamic non-contact mode

In the SFM dynamic non-contact mode of operation, the cantilever is vibrating near its resonance frequency at a distance of 5 nm to 100 nm above the sample surface, being driven by a piezoelectric oscillator. The topographic imaging principle, which was only simply described in Sect. 3.1.2, is explained in terms of a shift in the resonance frequency due to the tip-to-

sample interaction. As the tip is scanned over the surface, the resonance frequency of the cantilever is modified in function of the distance between tip and sample surface. A change of the resonance frequency results in a change of the response amplitude of the cantilever at the driving frequency. Using a lock-in technique the amplitude of the oscillation is detected and is used as an input for the feedback loop to adjust the z -position of the tip so that the elevation above the surface is maintained constant.

In the case of the ferroelectric samples, an additional shift of the resonance frequency appears due to the electrostatic interaction between the biased conductive tip and the electric field at the surface. When the vibrating tip enters a region with a non-homogeneous electrostatic field, the effective spring constant of the cantilever changes and this results in an extra shift of its resonance frequency. An image of the electric field gradient is therefore obtained in the dynamic mode ^[19]. Moreover, it was pointed out that only the component normal to the cantilever axis affects the resonance frequency ^[37] and usually it is assumed that, for most of the geometries, only the z -component of the gradient is important. Using this method, the lowest detectable force gradient was estimated by Lüthi et al. ^[19] to be 10^{-3} N/m.

The first experiments using the electrostatic interaction to control the feedback loop of an SFM were performed to detect localized charges deposited on insulators by Stern et al. ^[38] at IBM. A study of ferroelectric domains using the non-contact dynamic mode, was first reported only one year later by the same group ^[39]. Since an electric field gradient above a flat ferroelectric surface can exist near the domain walls, this method proved to be sensitive enough to image ferroelectric domain walls at a polished surface of the ferroelectric-ferroelastic material $\text{Gd}_2(\text{MoO}_4)_3$.

It should be mentioned that the image contrast depends essentially on the external bias voltage applied to the probing tip and on the tip material. By varying the bias voltage, the contrast of domain wall boundaries can be eliminated and a contrast between opposite domains can be observed ^[19]. A similar approach can provide a detection mechanism for previously written ferroelectric domains ^[40].

The voltage modulated non-contact mode

In order to improve the sensitivity of the method described above and to distinguish the signal given by the surface charge from other possible sources of the force gradient, it was suggested to apply a small AC voltage between the bottom electrode and the probing tip ^[39]. The frequency of this additional voltage should be far away from the cantilever resonance, in order to avoid any interference with the mechanical oscillation of the cantilever used in the feedback loop. The AC voltage results in alternating positive and negative charges on the tip. The tip-sample electrostatic force will thus also be periodic, causing a synchronous cantilever vibration, which can be detected using a lock-in technique with a much better signal-to-noise ratio than in the case of a DC bias. By monitoring the first harmonic signal, information about the surface charge distribution can be obtained. Another advantage of this method is that it is sensitive to the charge only and allows the determination of its sign.

This technique was further improved for surface potential imaging by using the AC-voltage-driven oscillation as a feedback signal to adjust the DC bias. Since the procedure is very similar to the one used by Lord Kelvin to determine the surface potential, the method was denominated Kelvin Probe Microscopy (KPM) ^[11,41,42,43].

A serious drawback of the techniques described in this section is that they are sensitive not only to the electric field but also to the other interactions between the tip and the surface (such as the Van der Waals forces). Therefore the data recorded should be deconvoluted to obtain the information on the ferroelectric domain structure [20]. If the experiments are performed under ambient conditions, the capillary force due to the adsorbed water layer should also be taken into account, since it would reduce the cantilever amplitude. Also, as it is well known, the electric field gradient strongly depends on the curvature of the surface. As a result, in the case of domains of irregular shape and corrugated surface topography, the electric field gradient signal is in fact a superposition of topography, damping on the surface, Van der Waals forces and the “true” signal, and accordingly it might be very difficult to interpret the images.

3.2.3 SFM dynamic contact mode

Also called voltage-modulated SFM, or piezoresponse-SFM, this method has proven to be the most suitable method to *study* and to *control* the ferroelectric domain structure at the nanometer scale. The main advantage is that it simultaneously allows the modification and detection of the ferroelectric polarization on a local level.

Evolution of piezoresponse-SFM

This technique was first used in 1991* by H. Birk et al. [44] who measured the piezoelectric coefficient in a ferroelectric copolymer of vinylidene fluoride and trifluorethylene using a scanning tunneling microscope (STM). The copolymer film was sandwiched between an aluminum layer and a 20 nm thick gold electrode, both used for applying voltages to the film and to enable the STM operation. Piezoelectric surface oscillations were induced using an AC voltage (10 V, 20 Hz) applied between the electrodes and detected with a lock-in amplifier connected to the feedback signal of the STM. When operating in constant current mode, the STM tip is kept at a constant distance from the sample and the feedback signal represents the vertical position of the sample surface. This new method proved to be useful to measure the local longitudinal piezoelectric coefficient and to show its hysteresis. One year later, the same group [45] succeeded in polarizing and imaging micron-sized ferroelectric domains in copolymer films without the top electrode, using atomic force microscopy combined with a lock-in technique, by detecting the local vibrations of the sample surface.

The first application of piezoresponse-SFM to the study of ferroelectric films of lead zirconate titanate (PZT) was reported in 1994 by Franke et al. [46]. One year later the signals involved in this technique were analytically calculated using a simple one-dimensional model [47,48]. The characterization of domain reversal in PZT films by recording *local hysteresis loops* was first reported by Hidaka et al. [49]. Systematic studies of domain dynamics, retention and fatigue effects have been carried out for thin films of PZT-based materials [50,51]. Also, investigations of ferroelectric domains at the surface of barium titanate (BaTiO₃), triglycine sulfate (TGS) and potassium trihydrogen phosphate (KTP) bulk single crystals were successfully performed [52,53,54]. The well-known domain structure of BaTiO₃ facilitated the validation and development of the detection of in-plane ferroelectric domains [55] leading to the mapping of all three components of polarization at the ferroelectric surfaces [56].

* to the best knowledge of the author.

However, the first results concerning the observation of the ferroelectric domain structure of other thin film materials than PZT were only reported in 1998 for $\text{SrBi}_2\text{Ta}_2\text{O}_9$ by Gruverman and Ikeda^[57], and in 1999 for $\text{BaBi}_4\text{Ti}_4\text{O}_{15}$ and $\text{Bi}_4\text{Ti}_3\text{O}_{12}$ by our group^[58,59,60].

Principle of piezoresponse-SFM

The piezoresponse-SFM technique is based on the converse piezoelectric effect, which is a linear coupling between the electrical and mechanical properties of a material. Since all ferroelectrics exhibit piezoelectricity, an electric field applied to a ferroelectric sample results in changes of its dimensions. Moreover, in most ferroelectric materials the piezoelectric effect can be interpreted as the electrostriction phenomenon biased by the spontaneous polarization^[8] leading to the conclusion that the piezoelectric coefficient and the spontaneous polarization are directly related (see Sect. 2.2).

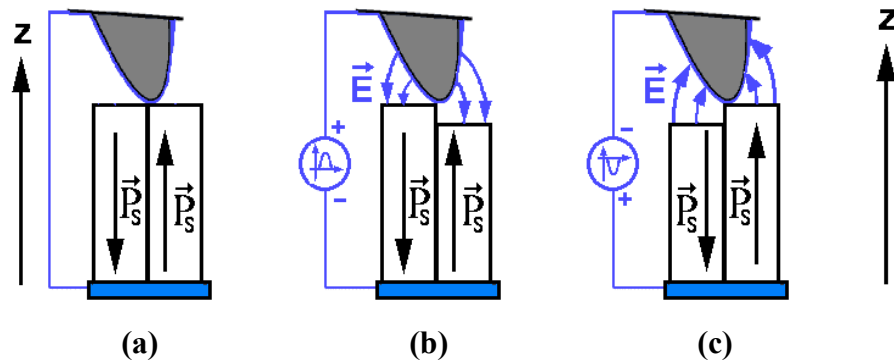


Figure 4 Principle of piezoresponse SFM (a) No topographic contrast if no voltage is applied. (b) A change in thickness occurs for a positive voltage applied to the tip (or during the positive half periods of an AC voltage). (c) Opposite thickness changes for a negative voltage (or during the negative half periods).

To detect the polarization orientation the SFM tip is used as a top electrode, which can be moved over the sample surface. To illustrate the imaging mechanism let us consider the simplified example circuit shown in Figure 4, with the ferroelectric sample sandwiched between a bottom electrode and the conductive SFM tip. Also let us consider two ferroelectric domains having opposite orientations of polarization, perpendicular to the sample surface. In Figure 4a no voltage is applied between the electrodes and the two ferroelectric domains have the same dimension in z-direction, only governed by the spontaneous strain which is the same for the two domains (since it has a quadratic dependence on polarization, as shown in Sect. 2.2). When a voltage is applied to the tip, the electric field generated in the sample causes the domains with the polarization parallel to the field to extend and the domains with opposite polarization to contract. The images (b) and (c) in Figure 4 illustrate the z-deformation of the domains when a positive, respectively negative voltage with respect to the bottom electrode is applied to the tip. To describe, in a first approximation, the electric field-induced displacements of the sample surface, we consider the following assumptions:

- The surface displacement is equal to the entire piezoelectric displacement induced in the sample; that is, the back surface of the ferroelectric is fixed^[61]. Any non-zero compliance of the bottom electrode would reduce the surface displacements.

- The electric field is uniform inside the ferroelectric sample, in the region underneath the SFM tip.
- The positive z-axis is as shown in Figure 4a, i.e. it is oriented from the bottom electrode towards the SFM tip.
- The voltages are given with respect to the bottom electrode.
- The spontaneous polarization is normal to the film plane.

Using the constitutive equations for the piezoelectric effect (Eq. 5a in Sect. 2.2) and the above assumptions, the following relation can be obtained ($X = 0$ was assumed):

$$\Delta z = -d^* V \quad \text{Eq. 11}$$

$$\text{where } \begin{cases} d^* = d_{33} & \text{for positive domains, } P_z > 0 \\ d^* = -d_{33} & \text{for negative domains, } P_z < 0 \end{cases}$$

The negative sign derives from the negative electric field caused by the application of a positive voltage to the tip; that results in a negative displacement of the surface when a positive voltage is applied to a positive domain.

A usual numeric value for the piezoelectric coefficient, $d_{33} = 50$ pm/V and applied voltage 4 V (a value limited by the coercive field of the film), result in a piezoelectric deformation of 0.2 nm which has to be detected (Eq. 11). This value is very close to the lower resolution of a usual SFM, and such a displacement can be very easily obscured by topographic features of 5 nm to 10 nm. Therefore, a DC voltage method is not suitable to monitor the ferroelectric domains on rough surfaces. Using an AC method combined with lock-in detection considerably improves the signal-to-noise ratio. By replacing the voltage in Eq. 11 with $V = V_{AC} \sin(\omega t)$ the surface movements induced underneath the tip are given by:

$$\Delta z(t) = \begin{cases} \Delta z^+(t) = -d_{33} V_{AC} \sin(\omega t), & P_z > 0 \\ \Delta z^-(t) = d_{33} V_{AC} \sin(\omega t), & P_z < 0 \end{cases}, \text{ or}$$

$$\Delta z(t) = \Delta z_0 \sin(\omega t + \Phi), \quad \text{Eq. 12}$$

Where the superscript $^+$ and $^-$ denote positive and negative domains, respectively, and:

$$\begin{cases} \Delta z_0 = d_{33} V_{AC} \\ \Phi = \pi & \text{for positive domains, and} \\ \Phi = 0 & \text{for negative domains.} \end{cases} \quad \text{Eq. 13}$$

Therefore, opposite orientations of polarization along the z-axis cause the sample surface to vibrate out of phase under a small AC voltage. The name “*voltage-modulated SFM*” of this method originates from the fact that during the scanning process, the SFM tip passes across different ferroelectric domains which modulate the carrier of information (the AC oscillation in this case) with their mechanical response, according to the local polarization orientation. Figure 5 illustrates the demodulation process.

The detection of the surface vibrations (or demodulation of the information on the polarization state) can be performed using a standard lock-in technique, as described below. The vertical position of the SFM tip (or its deflection) is usually monitored in SFM techniques using a laser beam, which is reflected by the cantilever on which the SFM tip is mounted. Using an optical detector the cantilever bending is converted into an electrical signal (the deflection

signal) and is further processed by the SFM controller. In piezoresponse-SFM, the deflection signal also contains the induced oscillations of the sample surface transmitted to the tip-cantilever. These electrical oscillations can be simply extracted from the global deflection signal using a lock-in amplifier. The lock-in detection rules out any other harmonic components of the deflection signal and the piezoelectric oscillations are in this way separated from the topography. The signal detected by the lock-in amplifier is usually referred to as the *piezoresponse* signal ^[29] and is directly related to the amplitude and phase of the surface vibration *via* the detector sensitivity δ :

$$v_{\omega} = \delta \Delta z_0 \cos(\Phi) \quad \text{Eq. 14}$$

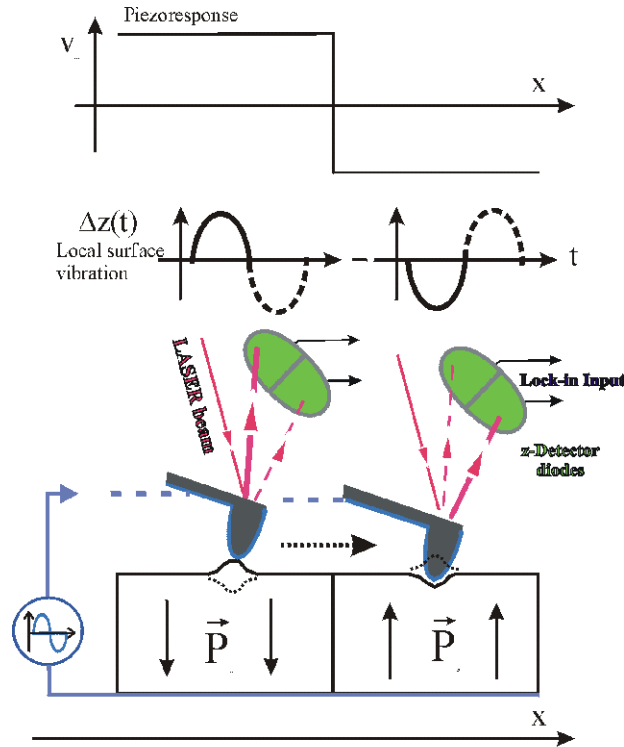


Figure 5 Demodulation of the information on the polarization state from the piezoresponse signal. The latter is modulated by the spatial variations of the piezoelectric coefficient.

The piezoresponse signal expressed in Eq. 14 contains an information about the polarization orientation of the area under the SFM tip *via* the phase shift Φ and also about the magnitude of the piezoelectric coefficient, provided that the phase factor can take only the two values indicated in Eq. 13 over the entire sample surface. This signal can be detected using a simple, single phase, lock-in amplifier. Using a dual lock-in amplifier it is possible to measure simultaneously the amplitude and the phase of the signal, therefore to study other phenomena such as the local piezoelectric losses. However, special care has to be taken regarding the analysis and interpretation of the phase signal.

Detection of the in-plane polarization by piezoresponse-SFM

Using the converse piezoelectric effect it is also possible to detect an in-plane component of the polarization vector (parallel to the sample surface). The basic principle of this detection consists

in the existence of piezoelectric shear deformations (Figure 6). If the polarization vector is perpendicular to the electric field, there is no piezoelectric deformation along the field direction, but a shear strain appears in the ferroelectric, leading to displacements of the sample surface parallel to itself, along the polarization direction. In the case of piezoresponse-SFM the in-plane displacements of the surface are transferred *via* friction to the SFM tip as lateral movements. The component of these movements perpendicular to the cantilever axis induces a torsion of the cantilever end, which can be detected using the capability of the SFM to measure the cantilever torsion.

The shear deformation depends on the polarization orientation and for the case of tetragonal perovskites with extended electrodes and the geometry illustrated in Figure 6 ($\vec{P} \parallel \vec{c} \parallel x$, $\vec{E} \parallel -\vec{a} \parallel -z$, and *cantilever axis* $\parallel \vec{b} \parallel y$, with xyz the coordinate system, and abc the crystallographic axes of the ferroelectric crystal) can be expressed as:

$$x_5 = -d^{**} E_z \quad \text{Eq. 15}$$

$$\text{where } \begin{cases} d^{**} = d_{15} & \text{for positive domains, } P_x > 0 \\ d^{**} = -d_{15} & \text{for negative domains, } P_x < 0 \end{cases}$$

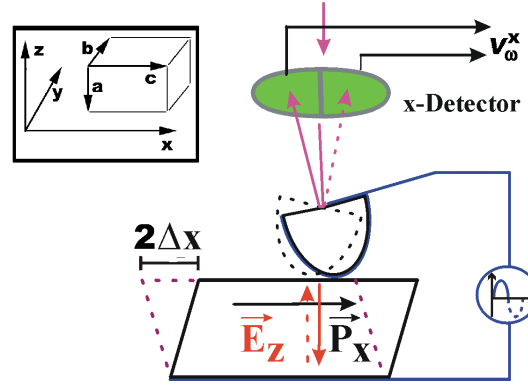


Figure 6 Detection of in-plane polarization. The inset shows the choice of the coordinate system and the crystallographic orientation of the ferroelectric crystal (the cantilever axis is parallel to the y-axis).

As in the case of detection of the domains with out-of-plane polarization, an AC field induces in-plane oscillations phase shifted by 180° in regions with opposite orientations of polarization.

$$\Delta x(t) = \Delta x_0 \sin(\omega t + \Phi), \quad \text{Eq. 16}$$

$$\text{where } \begin{cases} \Phi = \pi & \text{for positive domains, } P_x > 0 \\ \Phi = 0 & \text{for negative domains, } P_x < 0 \end{cases}$$

The surface vibrations described by Eq. 16 induce torsional oscillations of the cantilever with the same frequency. Due to the complex nature of the friction interaction it is difficult to describe them quantitatively. However, the phase shift of the oscillations above antiparallel domains describes the latter correctly, as it will be demonstrated in the analysis of the first

harmonic signals presented in Sect. 4.1. Therefore, in the case of in-plane detection the piezoresponse signal has a similar form as Eq. 14:

$$v_{\omega}^x = C \cos(\Phi)$$

where the constant C contains the detector sensitivity, the friction transmission factor, and the amplitude of the shear piezoelectric displacements.

It should be noted that a similar shear deformation is present along both the x-and y-axes. However, due to the cantilever asymmetry, domains having polarization along the y-axis can be recorded only by physically rotating the sample by 90° .

Two important features of the shear-piezoresponse signal should be mentioned. The first one is that the amplitude and phase only very weakly depends on the scan speed and does not depend on the scan direction. As it is well known for the friction (lateral force) technique, the deflection signal of the cantilever torsion increases almost linearly with the scan speed and reverses the sign when the scan direction changes. This is a normal behavior, since the friction torque is reversed for opposite scanning directions. However, the phase of the (additional) in-plane piezoresponse signal is not affected by the change in sign of the global friction signal.

Another important characteristic of the in-plane piezoresponse detection is that the signal is present even if the SFM tip is fixed on the surface. In the friction technique, only the dynamic friction coefficient between the SFM tip and the surface has been used, to date, for surface characterization. Estimation or comparison of static friction coefficients would require very tiny and accurate lateral movements of the scanner, a possibility which has not yet been implemented by SPM manufacturers. That is, when the tip is fixed on the surface, the static friction signal has no significant meaning. In spite of this fact, the amplitude of the shear piezoresponse signal is the same if the tip is stationary or scanned with a low speed.

The two features mentioned above are proofs that the origin of the first harmonic signal extracted from the friction signal is a real movement of the sample surface parallel to itself and that it is not picked-up from the circuitry of the electronic box. Moreover, by applying bias voltages to the tip it is possible in some situations to modify the polarization orientation of the in-plane domains, causing changes of the piezoresponse signal.

3.2.4 Theoretical approach to the tip-to-ferroelectric sample interactions

Understanding the tip-to-sample electrostatic interactions represents a key challenge in the field of electrostatic force microscopy (EFM). This comes from the fact that the electrostatic sensor has a complex shape: a cantilever with a conical or pyramid-shaped tip ending in a spherical apex. Since SFM is based on the detection of the cantilever movements, the models are focused on the description of the forces acting on the tip^[62]. Several attempts to describe the conductive tip-dielectric system with or without a bottom electrode can be found in the literature. Mainly, the models are developed along three directions. In this section a brief description of each model will be given.

The layered capacitor model

If only the qualitative analysis of the phenomena is required, then the simplest approach consists in modeling the tip and the sample with the bottom electrode as a capacitor^[47,48]. This

approach proved to be useful for the analysis of the signals implied in electrostatic^[39,63] and Kelvin force microscopy^[41,64,65].

In a first approximation, the volume under the tip-sample contact area can be considered as a capacitor composed of two layers (Figure 7). The upper layer with thickness h and permittivity ϵ_i represents the interface between the tip and the sample. The lower ferroelectric layer, which represents the sample itself, is described by the thickness t , the field-independent component of polarization P and the permittivity ϵ_f (which describes the linear component of polarization). In the case of non-contact EFM the upper dielectric is represented by the air gap, whereas for contact EFM, it can be a thin water layer adsorbed at the surface^[66].

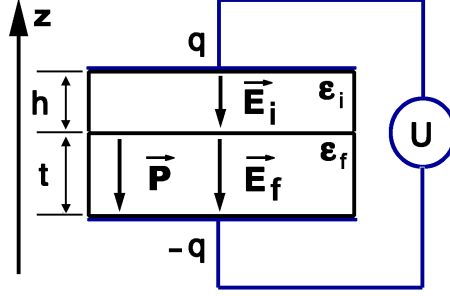


Figure 7 Simple layered capacitor model for the estimation of the deflection signals in EFM.

The electrostatic force (also called Maxwell stress force) acting on the tip can be easily found using Eq. 17, where the integral extends over the entire volume V of the capacitor. Since the normal component of the force acting on the tip is to be calculated, the derivation with respect to the tip elevation h has to be taken^[47,48].

$$F^{el} = -\frac{\partial}{\partial h} W^{el} = -\frac{\partial}{\partial h} \left(\frac{1}{2} \int_V \vec{E} \cdot (\vec{D} - \vec{P}) dV - qU \right) \quad Eq. 17$$

In the expression of the free energy, the term $-\vec{E} \cdot \vec{P}/2$ represents the energy density due to the fixed (spontaneous) polarization, and the term $-qU$ represents the energy supplied by the voltage source to the system. The force can be calculated using the system of equations given in Eq. 18 (for the designations see Figure 7).

$$\begin{cases} D = \epsilon_i E_i = \epsilon_f E_f + P \\ U = h \cdot E_i + t \cdot E_f \end{cases} \quad Eq. 18$$

In EFM experiments, the voltage applied to the tip has the form:

$$U = V_{DC} + V_{AC} \sin(\omega\tau) \quad Eq. 19$$

Considering that the cantilever deflection is proportional to the force *via* Hooke's law, the signals measured by a lock-in amplifier are directly proportional to the harmonic components of the force acting on the cantilever. These harmonic components can be calculated by solving the system Eq. 18 for the electric fields, introducing them in Eq. 17 and using Eq. 19. The result is presented in Eq. 20:

$$F = F_0 + F_\omega + F_{2\omega}, \quad \text{where} \quad F_{k\omega} = \frac{2}{T} \int_0^T F(\tau) \sin(k\omega\tau) d\tau$$

$$\begin{cases} F_0 = -\alpha \left[\left(V_{DC} + \frac{P}{\varepsilon_f} t \right)^2 + \frac{1}{2} V_{AC}^2 \right] \\ F_\omega = -\alpha \left(V_{DC} + \frac{P}{\varepsilon_f} t \right) V_{AC} \sin(\omega\tau) \\ F_{2\omega} = \frac{1}{4} \alpha V_{AC}^2 \sin\left(2\omega\tau + \frac{\pi}{2}\right) \end{cases} \quad \text{Eq. 20}$$

The parameter α is given in Eq. 21, where C represents the equivalent small signal capacitance of the system, and $T = 2\pi/\omega$ is the period of the AC voltage.

$$\alpha = \frac{S}{\varepsilon_i \left(\frac{t}{\varepsilon_f} + \frac{h}{\varepsilon_i} \right)^2} = -\frac{\partial C}{\partial h} \quad \text{Eq. 21}$$

Analyzing the spectral components of the electrostatic force (Eq. 20) it is possible to qualitatively explain the EFM signals, and also their relevance for ferroelectric domain imaging. A discussion of the first harmonic signals involved in voltage modulated SFM can be found in Sect. 4.1.

The method of image charges

Another approach to describe the tip-sample electrostatic interaction is to consider the tip as a conductive sphere above the surface and to solve the electrostatic problem “conductive sphere-dielectric layer-conductive plane”. The principle of the technique, as proposed by Goto and Hane, is to successively perform electrical imaging using the following three models: A point charge and a dielectric plane, a point charge and a conductive plane, and a point charge and a conductive sphere^[67]. The electrical imaging for these simple models is described in the literature^[68]. The potential of the sphere is set to the value V , and the conductive plane is grounded (it is kept at potential zero). V represents the voltage applied to the tip with respect to the bottom electrode. The procedure for the technique is as follows: First, an initial charge q_0 (Figure 8) is placed at the center of the sphere.

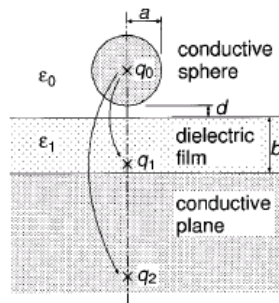


Figure 8 The method of image charges applied to EFM.

Next, two image charges, q_1 and q_2 (Figure 8), are created from q_0 . The charges q_1 and q_2 are determined independently by the conventional charge image method^[68] and are located in the

film and in the conductor, respectively. From each q_1 and q_2 , two more image charges are created. The production of image charges is continued in a similar manner until the total charges in the sphere and plane converge. The tip-sample capacitance is given by dividing the total charges (real charges) by the tip-sample voltage V , and the force acting on the tip can be found in a similar manner as described in the previous paragraph.

A variant of this model, named *the equivalent charges model*, is based on the principle of distribution of equivalent charges, or the image method of equipotential surfaces. According to this principle, a conductor in electrostatic equilibrium can be replaced with a set of fictive charges inside it, in such a manner that one of the equipotential surfaces follows exactly the shape of the conductor^[69]. Particularly, a conductive conical tip can be easily simulated with a distribution of charges placed on the cone axis. To solve the electrostatic problem of the real conductive tip and the dielectric sample, each of these charges has to be imaged as described above. This extension of the technique proved that the tip shape (pyramidal or conical for example) is not important, but that the lateral surface of the tip significantly contributes to the tip-sample capacitance for tip elevations higher than several nanometers above the sample surface.

The finite element method

A third approach to solve the electrostatic interaction between an SFM tip and a dielectric layer uses the finite element technique to compute exactly the potential and the electric field distribution. This method seems to be the most precise and also the most difficult. It requires an appropriate description of the geometry of the setup, which means that the respective shapes of the conductive tip and of the dielectric surface have to be mapped. To achieve a satisfactory spatial resolution for the solution without introducing errors due to the choice of the integrating domain, and also to maintain the mapping network at a reasonable size, Lanyi et al.^[70] solved the problem for the cylindrical symmetry of a conical tip. Therefore a two-dimensional geometry can be applied with adequate boundary conditions for a restricted area around the tip apex to find out the equipotential surfaces and/or the electric field lines.

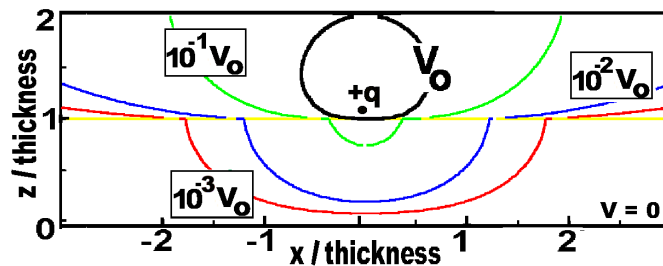


Figure 9 Equipotential lines of a point charge above a dielectric layer on a conductive plane, calculated with the method of image charges.

In this work a simplified variant of the image charges method was used to analyze the potential and electric field distribution induced by the SFM tip inside the sample. The theoretical calculations for an electrostatic system composed of a charge above a dielectric layer on a conductive plane are presented in Appendix A. The equipotential surfaces projected on the vertical plane containing the charge are shown in Figure 9. The finite element method for a simple geometry was also employed to qualitatively verify this result.

3.3 Piezoresponse-SFM setup

The experimental setup used in this work is schematically shown in Figure 10 and consists of a scanning probe microscope system, a lock-in amplifier, an AC voltage source, and a DC voltage supply. The scanning probe microscope (SPM) is a commercial Dimension 5000 microscope from Digital Instruments. For piezoresponse measurements the SFM was set to operate in contact mode, at a constant interaction force between the tip and the sample surface [71]. The value of the contact force depends on the spring constant of the cantilever, i.e. on its geometry and elastic properties.

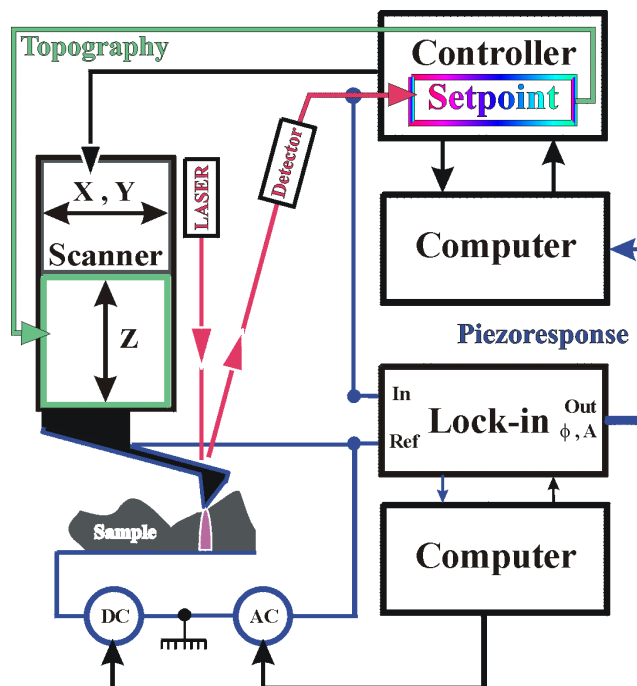


Figure 10 Experimental setup used for piezoresponse measurements.

In the constant force regime the feedback loop adjusts the vertical position by keeping a constant deflection of the cantilever so that not only the tip, but also the Z-scanner follows the local elevation of the sample surface. In this mode of operation the deflection signal, which represents the cantilever bending converted into an electrical signal by the optical detector, has a relative large constant value (of the order of 1 V, depending on the setting for the setpoint) over which small variations are superimposed (several mV). These variations are caused by the finite reaction time of the feedback loop and are proportional to the derivative of the feedback signal with respect to the time, i.e. if the scan speed is kept constant they represent the local slope of the sample surface along the scan direction.

For piezoresponse imaging, a small AC voltage has to be locally applied between the SFM tip and the bottom electrode of the sample, and the induced oscillations have to be detected, as described in Sect. 3.2.3. To extract the surface vibrations, a digital lock-in amplifier from EG&G Instruments, model 7260 was used. The signals were picked up from

intermediate processing stages* of the global deflection signal inside the electronic box controlling the SFM head. Since the lock-in internal noise limit is $2nV/\sqrt{Hz}$ [72] the measurement noise of $1.4\mu V/\sqrt{Hz}$ was determined by the electronic circuitry inside the SFM electronic box.

In most of the experiments, the internal oscillator of the lock-in amplifier was used as the AC source to induce the mechanical oscillations detected. The choice of the amplitude and frequency of the testing AC voltage depends on the specific experimental conditions. These conditions include two contradictory aspects:

- The AC amplitude has to be as small as possible, for a “non-destructive” testing, i.e. no switching of the ferroelectric polarization underneath the tip must be caused by the AC voltage. This implies that the amplitude has to be lower than the local coercive voltage of the ferroelectric domain, which may be different for each grain and even for each domain within the same ferroelectric crystallite [58]. As predicted by Gruverman et al. [29] and proven experimentally by our group [73], the occurrence of a polarization switching under the tip (with the frequency of the AC testing voltage) leads to a decrease of the piezoresponse signal and therefore makes the interpretation of piezoresponse data more difficult.

- To enhance the signal-to-noise ratio, the testing voltage has to be as high as possible in order to get a high amplitude of the mechanical vibration and thus a high piezoresponse signal. The main source of noise during the acquisition of the piezoresponse images is the global deflection signal itself, from which the first harmonic signal is extracted. The deflection signal, which is used by the SFM system as a feedback to maintain a constant force between tip and sample, is proportional to the scanning speed and to the derivative of the surface height with respect to the scan direction.

For samples with a high roughness, the deflection signal exhibits very sharp high peaks. These fast variations of the deflection signal may have harmonic components with the same frequency as the AC testing voltage and also amplitudes comparable with the piezoresponse signal. This noise may be overcome by using a low scanning speed and a high frequency probing voltage. However, this leads to a long recording time for the acquisition of the image. This is clearly demonstrated in the experiment illustrated in Figure 11, where the signals involved in piezoresponse imaging of a $\text{Bi}_4\text{Ti}_3\text{O}_{12}$ grain are shown for two different scanning speeds. The topography signal of a grain of $\text{Bi}_4\text{Ti}_3\text{O}_{12}$ divided into two ferroelectric domains was not influenced by changing the scan speed from $1\mu\text{m/s}$ to $0.2\mu\text{m/s}$, but the deflection and piezoresponse signals show considerable reduction of noise.

The frequency of the testing signal has to be chosen far from any possible perturbing oscillations that may appear in the system, such as the resonance frequencies of the cantilever. Depending on sample, tip material, and cantilever spring constant, the AC testing voltage used had amplitudes between 0.5 V and 5 V and frequencies between 900 Hz and 75 kHz.

The internal source of a Keithley 6517 electrometer was utilized to apply DC bias voltages to the ferroelectric sample. The output voltage resolution of 5 mV when operating in the 100 V range, and the maximum output current of 10 mA were perfectly suited for the poling experiments performed during this work [74]. The lock-in amplifier, the AC source and the DC voltage source were all fully controlled by a computer via an IEEE 488 general

* Connections indicated by the manufacturer.

purpose interface bus, using adequate programs developed in house using the data acquisition and analysis software TESTPOINT (Capital Equipment Corp.).

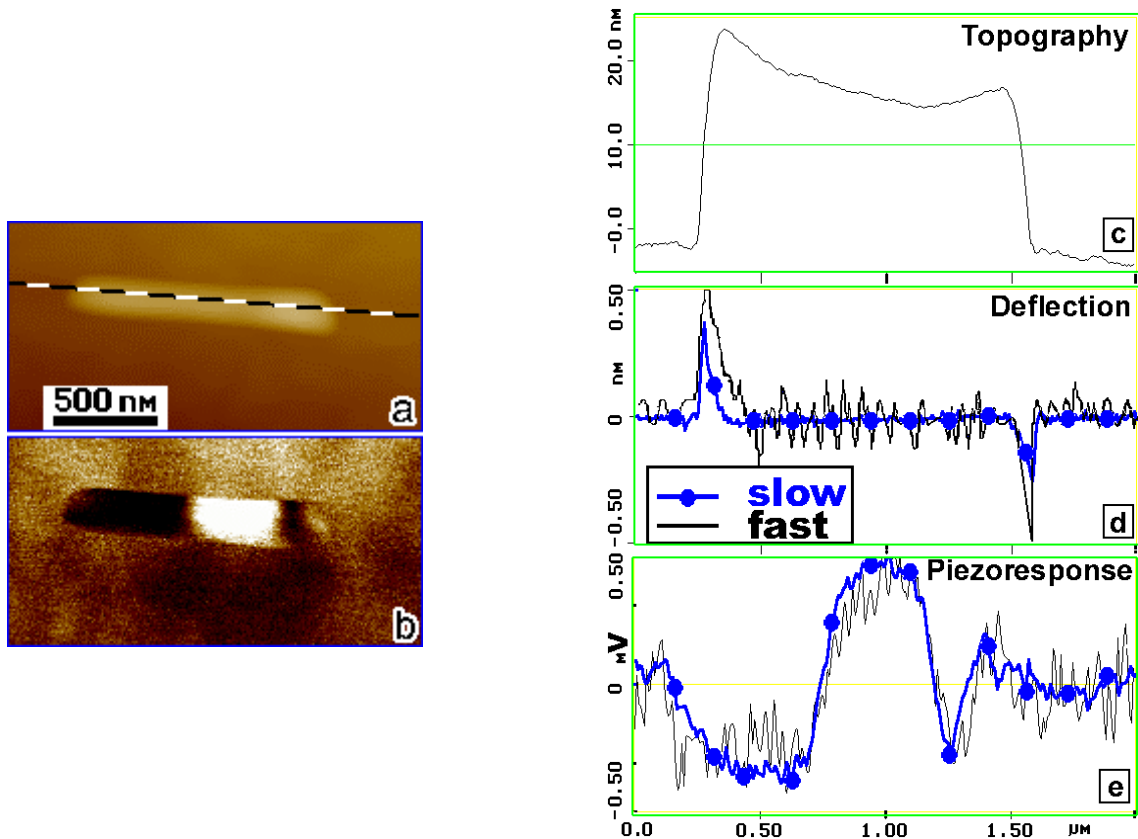


Figure 11 The signals involved in piezoresponse imaging. (a) Topographic image (the height signal) of a $\text{Bi}_4\text{Ti}_3\text{O}_{12}$ grain (the black-white dashed line has been added). (b) The domain structure (z-piezoresponse signal). (c–e) The height (c), the vertical deflection (d), and the piezoresponse (e) signals along the dashed line in (a). The lines with dots in (d) and (e) were acquired with a much lower scan speed than that used for the measurement of the thinner lines.

The most important component of the SFM setup is the SFM tip, which senses the sample surface. Different types of SFM probes were used in this work.

Silicon nitride cantilevers are the standard for contact mode AFM measurements, because this material is hard to wear, works well with most of the samples, allows the use of a very low contact force between the tip and the sample surface (less than 10 nN), and they are rather cheap. However, they need a conductive coating for use in electric force microscopy, in particular for piezoresponse measurements. Difficulties with metal coating of silicon nitride** prevented their exclusive use in these measurements. In general, the silicon nitride probes are suited for low-contact-force piezoresponse imaging^[57], but not for the quantitative ferroelectric characterization of the films.

Highly doped silicon cantilevers with a resistivity of 0.02 Ωcm have spring constants between 4 N/m and 50 N/m depending on the cantilever geometry^[75]. The forces on the

** Soft cantilevers easily bend when coated. Stress control of the coating requires a very special equipment. The tip sharpness also deteriorates considerably. Moreover, the conductive layer may be removed at the tip apex after several scans, causing a drastic deterioration of the piezoresponse images.

sample can be derived from the spring constants and they were between 0.05 μN and 10 μN . These SFM probes were mostly used in the present work due to the following reasons:

- The high doping level with boron acceptors assures a good electrical conductivity of the probe, without any metal coating. The quality of the electrical contact remains constant during the whole experiment, even if the apex geometry changes during the scanning.
- A high spring constant of the cantilever means a high mechanical resonance frequency, which allows the use of a high frequency for the AC testing voltage.
- For piezoelectric measurements in atomic force microscopy, it was proved that the effects of the electrostatic interaction between the tip-cantilever and sample-bottom electrode systems are highly reduced^[76] by using cantilevers with high elastic constant.

The lower limit for the lateral resolution achieved is directly related to the radius of the tip apex, and it was estimated to be about 10 nm – 20 nm for the soft cantilevers, and 30 nm – 50 nm for the stiff cantilevers.

All experiments described in this work were done under ambient conditions, at room temperature.

3.4 Investigated systems

3.4.1 Epitaxial thin films

Epitaxial ferroelectric thin films of $\text{SrBi}_2\text{Ta}_2\text{O}_9$ (SBT), $\text{Bi}_4\text{Ti}_3\text{O}_{12}$, and $\text{BaBi}_4\text{Ti}_4\text{O}_{15}$ were deposited by pulsed laser deposition (PLD) onto epitaxial layers of electrically conductive LaNiO_3 . The epitaxial LaNiO_3 layer served both as a template favoring the epitaxial growth of the ferroelectric film and as a bottom electrode for the electrical characterization. The conductive LaNiO_3 epitaxial layers were grown either on top of (100)-oriented SrTiO_3 (STO) single crystals or on top of (100)-oriented single-crystalline silicon substrates previously coated with a stack of epitaxial CeO_2 and YSZ buffer layers. The CeO_2 /YSZ bilayer serves as a template to promote the epitaxial growth of the LaNiO_3 electrode layer on Si(100), the LaNiO_3 layer promoting the epitaxial growth of the desired bismuth-layered perovskite film^[77,78].

All the films and layers were grown by PLD employing a KrF excimer laser ($\lambda = 248 \text{ nm}$) at a laser repetition rate of 5 or 10 Hz. The depositions of all the films were performed in a pure oxygen atmosphere in a continuous sequence without breaking the controlled atmosphere conditions. The films were grown on substrates heated at high temperatures estimated to lie between 675°C and 685°C for YSZ and between 650°C and 670°C for the other materials. After the deposition of the bismuth-layered perovskite film the epitaxial heterostructure was slowly cooled down to room temperature in 13.3 Pa of pure oxygen. The deposition parameters used, as well as the typical thickness obtained for the different deposited materials, are summarized in Table 1.

The structure of the films was studied by X-ray diffraction (XRD) using a Philips X'Pert MRD four-circle diffractometer and plan-view and cross-section TEM. The morphology of the films consists of a c-oriented matrix with embedded grains of another orientation. The detailed XRD analysis of all the bismuth-layered thin films showed that the

grains have $(110)_{orth}$ and $(100)_{orth}$ orientations and are embedded into the (001) -oriented (i.e. c -oriented) film matrix ^[79]. This observation is fully consistent with the SFM and TEM investigations as shown in Figure 12.

Deposition parameters	YSZ	CeO ₂	LaNiO ₃	Bi ₄ Ti ₃ O ₁₂	SBT	BaBi ₄ Ti ₄ O ₁₅
Repetition rate (Hz)	10	10	5	10	10	10
Pulse energy (mJ)	450	350	350	350	350	350
Energy density (J/cm ²) (on the target)	3	2.7	2.7	2.7	2.7	2.7
Heater temperature (°C)	820	800	800	800	800	800
Substrate temperature (°C) (estimated)	680	665	665	665	665	665
Oxygen pressure (x7.5 Pa)	10 ⁻²	100	300	100	100	100
Film thickness (nm)	≈50	≈20	≈50	≈400	≈150	≈300

Table 1 Summary of the deposition conditions used for the growth of epitaxial YSZ, CeO₂, LaNiO₃, Bi₄Ti₃O₁₂, SBT, and BaBi₄Ti₄O₁₅ films.

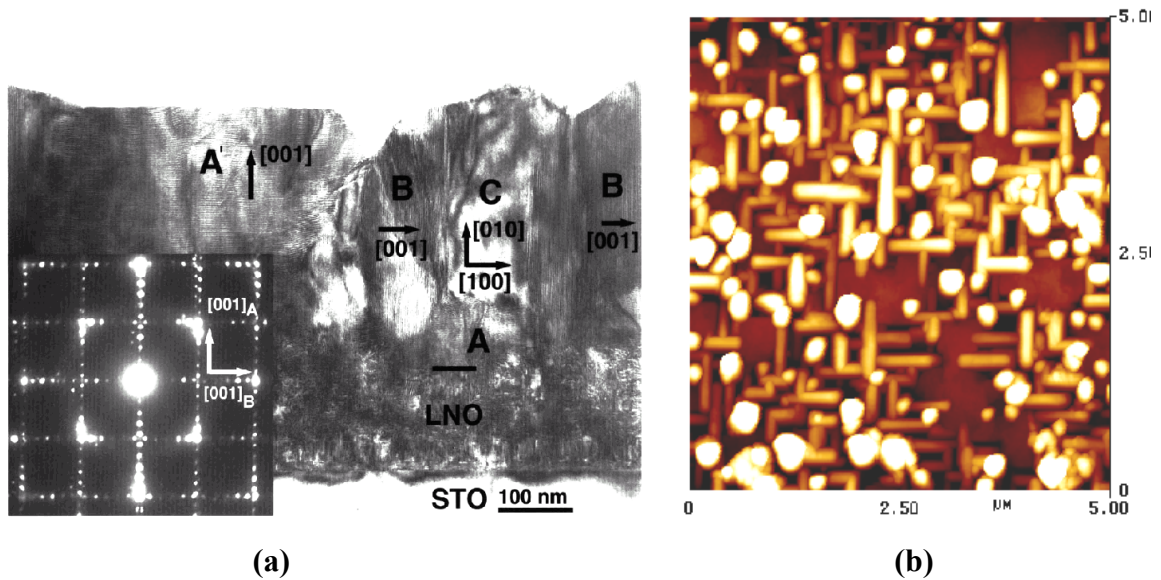


Figure 12 Typical characteristics of the epitaxial films (here BaBi₄Ti₄O₁₅/LaNiO₃/STO): **(a)** cross section TEM image of rectangular-shaped crystallites. The image shows the c -oriented grains (A, A') and also the $(110)_{orth}$ -oriented grains (B and C). The inset displays a selected area diffraction pattern corresponding to both (001) - and $(110)_{orth}$ -oriented regions. **(b)** SFM topography image of a region similar to that of (a). Note that tetragonal indexing is used in (a), so that, e.g., $[010]_t = [110]_{orth}$.

3.4.2 Polycrystalline PZT films

PZT thin films were deposited using the chemical solution deposition (CSD) method. The PZT precursor solution was prepared with Pb acetate, Ti- and Zr-isopropylate as metal precursor, and with 2-methoxyethanol (2ME) as solvent. Pb acetate was dissolved in 2ME, dehydrated at 125°C and then cooled to about 80°C. Separately, Ti and Zr isopropylate were dissolved in 2ME and the solutions were heated up to 125°C under stirring to evaporate water and any reaction by-products. The Ti and Zr solutions were stabilized against hydrolysis by reaction with acetylacetonate. After cooling down to 80°C, Pb, Ti and Zr precursor solutions were mixed and the final solution was heated to 120°C under continuous stirring and kept under these conditions until a concentration of about 0.1 mol⁻¹ was achieved. After cooling down to room temperature, the obtained PZT precursor solution was filtered with a 0.22 µm teflon filter.

The PZT thin films were obtained by solution spinning onto the substrates at 2000 rpm for 35 s. The metalorganic films were dried at 120°C for 1 min. and successively pyrolysed on a hot plate at 300°C for 5 min. For the specific concentration (of the solution) used, the thickness of one coating was about 150 nm. The spinning-pyrolysing sequence was repeated several times to increase the film thickness to the desired value. Finally the PZT films were crystallized by conventional thermal annealing for 30-60 min. performed in air at temperatures ranging from 550°C to 650°C.

3.4.3 Patterned nanostructures

Regular SrBi₂Ta₂O₉ (SBT) and PZT structures with lateral sizes under 100 nm were fabricated using electron beam direct writing (EBDW)^[80]. Electron beam lithography is one of the next-generation lithography processes allowing a resolution down to several tens of nanometers,. EBDW is a maskless lithography process widely used for writing metallic and oxide nanostructures using metalorganic precursors^[81] and alleviates the etching of the ferroelectric thin film, which is known to be an unsolved problem at these dimensions^[82]. Chemical reactions are locally induced in a metalorganic thin film by irradiation with an electron beam having sufficient energy and dose and the desired pattern is written by scanning the electron beam over the sample. The pattern is developed by dissolving the unexposed area in a specific solvent and further transformed into metal or oxide by thermal annealing^[83,84].

Test patterns of SBT and PZT cells with lateral dimensions between 1 and 0.125 µm were exposed into a corresponding metalorganic film using a commercial electron beam lithography system (ELPHY Plus) adapted to a JEOL JSM 6400 scanning electron microscope (SEM) working at an acceleration voltage of 40 kV. Exposure was performed at electron doses varying from 1500 to 6000 µC/cm² for PZT and 600 to 1200 µC/cm² for SBT. The structures were developed by immersing the exposed sample for 1 min. in toluene, and were then dried by blowing with nitrogen.

After developing, the metalorganic mesas were subsequently transformed into an oxide by annealing in air for 5 min. at 300 °C and further crystallized into the ferroelectric phase by annealing at temperatures ranging from 600 to 850 °C.

Representative structures consisting of periodic patterns of ferroelectric cells yielding a memory density of 1 Gbit/cm² are presented in Figure 13. The cells are well defined in shape

and are polycrystalline with grains having sizes of 20 nm or less (smaller for PZT than for SBT). During the crystallization process, the smallest SBT structures lose their rectangular shape while PZT structures maintain their shape even after a 50% shrinkage.

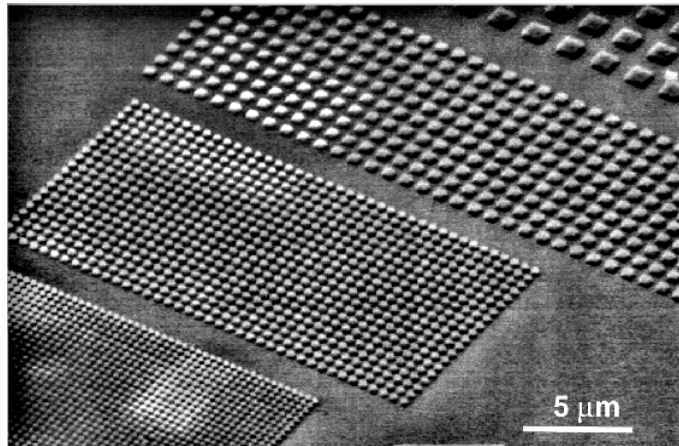


Figure 13 Metalorganic SBT test structures developed in toluene after e-beam exposure with an electron dose of $3 \mu\text{C}/\text{cm}^2$.

4. Piezoresponse-SFM for local electromechanical probing of ferroelectric thin films

The aim of this chapter is to analyze the possibilities of using the method of piezoresponse SFM not only to image the domain structure, as it was used up to now, but also to locally characterize the ferroelectric properties with a resolution of several nanometers. This expansion consists in describing some techniques that may be used to obtain *quantitative* information on the physical quantities involved in piezoelectric probing.

First of all, it is very important to establish the origin of the demodulated signals, especially the first harmonic component. With other words, it is important to know whether and how it is possible to probe the true electromechanical properties of ferroelectric samples. The next section ascertains that the first harmonic signal in the experiments presented in this work reflects the sample surface movements and not the electrostatic interaction between the tip and the electric field at the sample surface.

4.1 Analysis of the first harmonic signal in voltage modulated SFM

As has been shown in the sections 3.2.3 and 3.2.4, there are two types of forces governing the tip movement above the ferroelectric sample ^[85,48], namely the repulsive contact force and the electrostatic force.

The piezoelectric displacements of the sample surface are given in Eq. 12 (Sect. 3.2.3) and the first harmonic of the Maxwell stress force in Eq. 20 (Sect. 3.2.4). Both of these forces act simultaneously on the tip when operated in contact mode, therefore the first harmonic of the tip deflection is the superposition of their effects. Whether the tip movement is governed by the electrostatic interaction or by the surface displacements can be determined from the phase of the first harmonic, as it will be shown in the following.

The AC voltage was always applied to the SFM tip so that the phase shifts correspond to those calculated previously. To assure a proper ground of all the equipment in the setup, the DC voltages were applied to the bottom electrode (exactly as shown in Figure 10, Sect. 3.3), and not to the tip. However, the position of the DC source does not change the phase signal measured. For a region (ferroelectric domain) with polarization oriented downward (top-to-bottom) and an AC voltage applied to the tip, during the positive half-periods (electric field in the film directed downward, thus parallel to the polarization), the piezoelectric deformation is an extension, and the surface will move upward. Therefore, the piezoelectric signal is *in phase* with the applied AC voltage. At the same time, the first harmonic of the Maxwell stress (see F_ω in Eq. 20, Sect. 3.2.4, with α always positive) and the AC voltage are *out of phase*.

The above considerations lead to the conclusion that if the electrostatic interaction causes the cantilever deflection, *the tip does not follow the vertical displacements of the sample surface*, but oscillates out of phase with the induced piezoelectric deformations! Whether the tip vibrates in phase (therefore in permanent contact) with the ferroelectric surface or oscillates out of phase depends on the balance of the contact and electrostatic forces. The experiments presented in this work were performed using stiff cantilevers with high spring constants of $k = 40 \text{ N/m}$, which imply contact forces in the range from $2 \mu\text{N}$ up

to $10 \mu N$. The Maxwell stress force F_ω estimated from Eq. 20 using $S = \pi (20 \text{ nm})^2$, $t = 200 \text{ nm}$, $h = 1 \text{ nm}$, $\epsilon_f = 200 \epsilon_0$, $\epsilon_i = 2 \epsilon_0$, $V_{AC} = 2 \text{ V}$ and $P = 20 \mu C / cm^2$ is found to be $0.12 \mu N$, and therefore is about ten times smaller than the usual repulsive contact force.

The above estimation, however, needs to be validated experimentally. To demonstrate that in this work the first harmonic signal reflects the piezoelectric effect, the following experiment was performed: The SFM tip was positioned above a certain region of the sample surface, showing an in-phase oscillation of the first harmonic deflection with respect to the AC voltage applied. Therefore the polarization of the respective region was oriented downward. For practical reasons, the phase offset was always set to 180° , so that the piezoresponse signal from positive domains is positive. Above this point, the SFM tip was then scanned in the z-direction, using the force curve measurement procedure of the SFM controller. The DC deflection and the first harmonic component of the cantilever deflection were recorded at three values of the bias voltage: $V_{DC} = 0$, $V_{DC} = 2 \text{ V}$ and $V_{DC} = -2 \text{ V}$. The local coercive field of the ferroelectric sample probed in this experiment was $V_{coer} = 8 \text{ V}$, therefore the bias did not switch the ferroelectric domain ($V_{AC} = 2 \text{ V}$). The results are shown in Figure 14 as deflection versus z-scanner position plots.

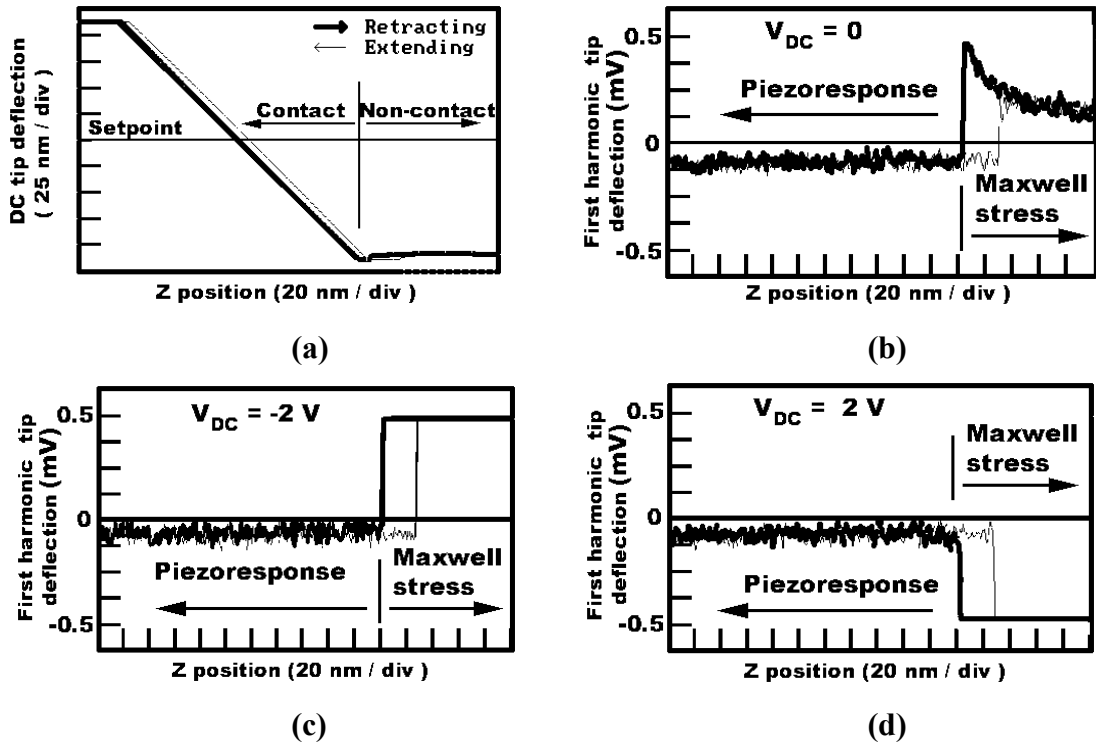


Figure 14 Deflection versus z-scanner position above a negative ferroelectric domain (polarization downward) in a BaTiO_3 single crystal: **(a)** DC component (force curve). **(b,c,d)** First harmonic component at different V_{DC} : **(b)** $V_{DC} = 0$, above the surface (non-contact) the signal is 180° phase shifted with respect to the signal when the tip is in contact with the surface. **(c)** $V_{DC} = -2 \text{ V}$, and **(d)** $V_{DC} = 2 \text{ V}$. The first harmonic signal in contact mode is not influenced by the DC bias. These measurements prove the piezoelectric nature of the first harmonic signal in contact mode.

The DC component of the deflection was not influenced, within the experimental errors, by the DC voltage, and the plot in Figure 14a represents a usual force curve (compare

with Figure 3 in Sect. 3.1.1). Above the sample surface, in non-contact, only the electrostatic interaction is present in the first harmonic signal. For $V_{DC} = 0$ the phase shift changes from 0° to 180° (Figure 14c, the first harmonic changes from positive to negative) as the tip approaches the surface and is pushed into it, *in complete agreement with the expected phase shifts* of the two signals for a negative domain (see Eq. 12 in Sect. 3.2.3 and Eq. 20 in Sect. 3.2.4).

Moreover, as can be seen in Figure 14c-d, the bias voltage has a strong influence on the first harmonic, in agreement with the strong dependence of F_ω on V_{DC} in Eq. 20*. In contrast, in the contact region of the curves, the first harmonic signal is independent of the bias voltage (with the restriction that it is lower than the coercive voltage, of course). This is an incontestable proof that the electrostatic interaction has no visible influence on the signal and the tip truly follows the surface vibrations when operated in contact mode.

The cantilever torsion and therefore the lateral deflection signal could, in principle, also be influenced by an electrostatic interaction [55]. Figure 15 proves that the x-deflection signal is non-zero *only* when the tip is in contact with the surface and the polarization is in the film plane.

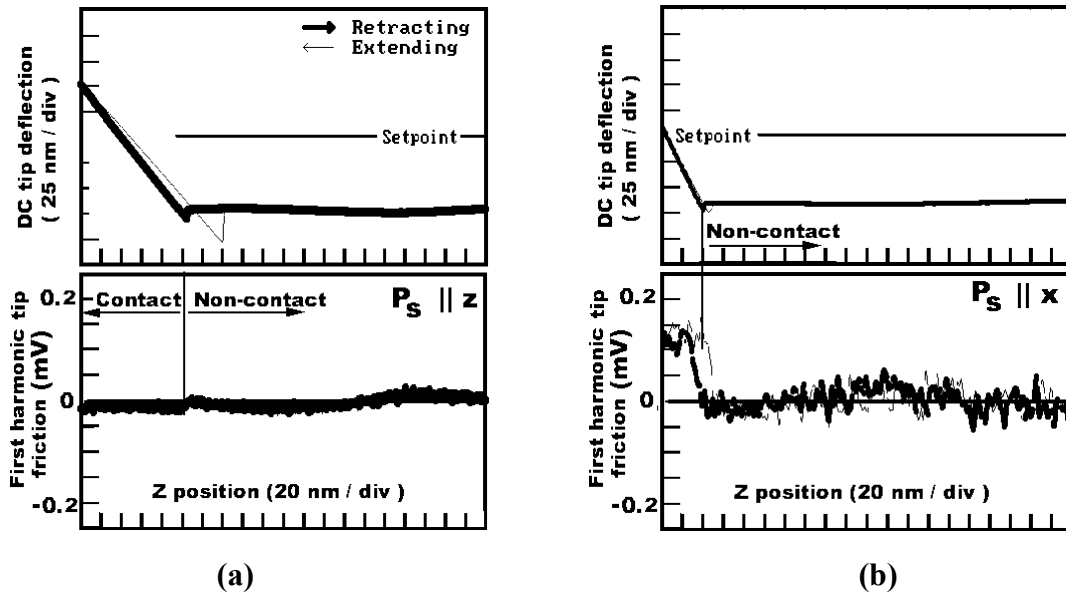


Figure 15 First harmonic component of the x-deflection signal (lower plots) versus z-position of the scanner: **(a)** above a domain with polarization perpendicular, and **(b)** above a domain with polarization parallel to the sample surface (BaTiO₃ single crystal). The upper plots show the tip-to-sample contact position. Above the sample, in the non-contact region, the x-deflection signal is always zero.

In conclusion, when the tip is in contact with the surface, *only the piezoelectric effect* is responsible for the first harmonic of both the in- and out-of-plane cantilever deflections.

* Because the DC bias is applied to the bottom electrode, the sign of V_{DC} in Eq. 20 has to be changed from positive to negative.

4.2 Imaging of the ferroelectric domain structure

As it was demonstrated in the previous section (4.1) the first harmonic component of both deflection signals (corresponding to the vertical and lateral movements) indeed represents the induced piezoelectric vibrations of the ferroelectric sample. Therefore, the first harmonic signals recorded above a given point of the surface describe the two components of polarization perpendicular to the cantilever axis at that point.

To obtain the distribution of ferroelectric domains at the surface of a sample using SFM it is necessary to associate the position of the SFM tip to the signal containing information about the ferroelectric state. This can be most easily achieved using one of the built-in input channels of the SFM system. Alternatively, the same task can be fulfilled using a second computer to collect and store the (x, y) position from the SFM scanner, and the piezoresponse signal (i.e. domain information). The image of the domains is usually visualized by associating different colors to different levels of the signal.

Out-of-plane domains

Monitoring the first harmonic of the z-deflection signal while scanning the surface results in an image of the effective longitudinal piezoelectric coefficient d_{zz} . Using Eq. 12 and Eq. 14 (Sect. 3.2.3), the relationship between the measured signal v_{ω}^z and d_{zz} is given by Eq. 22:

$$v_{\omega}^z = \delta d_{zz} V_{AC} \quad \text{Eq. 22}$$

where δ , the sensitivity of the optical detector, is in fact the conversion factor between the mechanical displacement of the SFM tip and the electric deflection signal.

An information about the polarization state is obtained from the linear relation between the piezoelectric coefficient and the spontaneous polarization. It is well known that for ferroelectric materials having a tetragonal symmetry (point group 4mm) and with a centrosymmetric paraelectric phase the piezoelectric effect can be considered as the electrostriction effect biased by the spontaneous polarization \mathbf{P}_S as shown in Sect. 2.2 (Eq. 10a). If the region being probed is not *c*-oriented (\mathbf{P}_S is not normal to the film plane), an effective piezoelectric coefficient has to be considered. As shown in Appendix B, magnitude and sign of the piezoelectric coefficient along a certain direction (denoted d_{zz}) is related (but not directly or simply related) to the angle between the spontaneous polarization and the normal to the film surface. Therefore, the distribution of d_{zz} represents in fact a more or less faithful* image of the out-of-plane polarization distribution at the sample surface, at least for the materials that belong to the 4mm point group symmetry.

In-plane domains

The first harmonic of the lateral deflection signal being proportional to the shear piezoelectric coefficient (see Eq. 16), the above considerations hold for the in-plane domains, too. As it was deduced thermodynamically for the same tetragonal symmetry in Sect. 2.2, the shear piezoelectric coefficient d_{15} is given in Eq. 10b for the case of the cantilever axis

* depending on the balance between d_{33} , d_{31} , and d_{15} in Eq. A 7 (Appendix B).

perpendicular to the spontaneous polarization, which is parallel to the film plane (geometry shown in Figure 6, Sect. 3.2.3). In the general case where the spontaneous polarization is oriented in the film plane along an arbitrary direction relative to the cantilever (see the xyz system of coordinates in Figure 6), an effective shear coefficient d_{xxz} is detected. Magnitude and sign of d_{xxz} depend on the angle between the x -axis and the spontaneous polarization^[86].

Therefore, the in-plane domains can be visualized in the same manner as the out-of-plane domains, a mapping of d_{xxz} being a more or less distorted image of the in-plane polarization. However, special care has to be taken when interpreting the in-plane domains if the scan direction is not along one of the principal crystallographic directions, due to the complex nature of the friction-induced cantilever vibrations.

4.3 Local measurements

The usual macroscopic techniques used for the measurement of the electromechanical properties^[7,87,88] cannot be applied in the case of SFM, due to the fact that the geometry of the region being measured is depending on its position. In this case, the SFM conductive tip represents in fact a nanometer-sized movable top electrode used for probing the sample surface by applying an AC voltage. This top electrode can be fixed over any desired place of the sample surface, in order to explore only that area. Taking into account that the sample is tested by detecting the induced mechanical oscillations, several procedures can be used to measure the local properties.

4.3.1 Local piezoelectric coefficient

The local piezoelectric coefficient can be determined with a high accuracy by sweeping the amplitude of the testing AC voltage from zero up to the local coercive voltage of the sample. The piezoelectric constant can be easily calculated from the slope of the linear dependence expressed in Eq. 22 (Sect. 4.2). In the case of ferroelectrics, as soon as the AC amplitude is higher than the local coercive voltage, the polarization starts to switch with the same frequency as the AC voltage, leading to a decrease of the first harmonic response.

4.3.2 Stress dependence of piezoelectric coefficient

The influence of the mechanical stress on the longitudinal piezoelectric coefficient can be studied by varying the contact force between the tip and the sample while recording the piezoresponse signal. Since the stress applied strongly depends on the real contact area, which is very difficult to estimate, the contact force dependence is used instead. The range of contact forces that can be used depends on the elastic constant of the cantilever.

In general, the piezoelectric coefficient decreases when the stress (or the contact force) increases*.

* In the thermodynamic treatment of ferroelectricity, an increase of the stress X is equivalent to an increase of the temperature T (Eq. 2, Sect. 2.1), therefore the ferroelectric is closer to its paraelectric phase and has a smaller spontaneous polarization (and implicitly also a smaller piezoelectric coefficient).

4.3.3 Hysteresis loops

The most important characterization and also a proof of ferroelectricity is the presence of a piezoelectric *hysteresis*. This measurement is generally performed using a DC bias source connected in series with the AC voltage source. The hysteresis loops are obtained by sweeping the bias voltage and recording the piezoresponse signal. There are two main procedures that may be used:

1. *In-field hysteresis*. In the first procedure, the probing AC voltage is superimposed on the DC bias which is varied in steps from zero to V_{max} , then decreased down to V_{min} and increased again up to V_{max} , in order to measure the piezoelectric coefficient as a function of the DC field applied *simultaneously*. Each step of the bias has a duration t_{bias} (Figure 16a). The loop obtained in this manner is further referred to as *in-field* hysteresis loop and represents a normal $d - E$ curve ^[89], as it is often used for the characterization of the macroscopic piezoelectric properties of thin films.

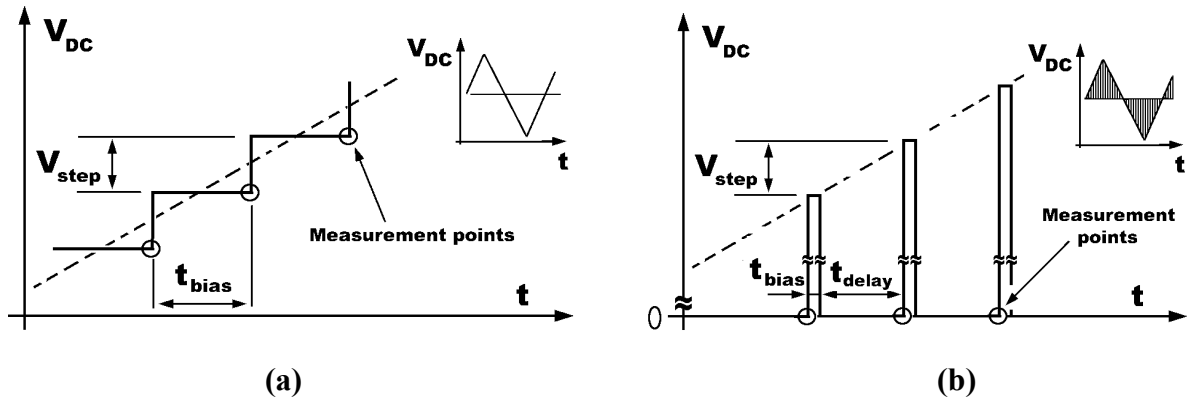


Figure 16 The waveform of V_{DC} in hysteresis loop measurements: (a) for the in-field loops, and (b) for remanent loops

2. *Remanent hysteresis*. In the second procedure, the DC bias voltages are in fact pulses with a duration t_{bias} and an interval of time t_{delay} between them. The piezoresponse signal is recorded and stored just before the application of the next polarizing pulse (Figure 16b) ^[49,90]. The amplitudes of the pulses are varied in steps in the same way as in the first procedure. Using this measuring method, the electrostatic interactions between tip-cantilever and the bottom electrode are avoided during the measurement and only the *remanent* piezoelectric coefficient is measured as a function of the DC voltage pulse *previously* applied to the sample. The loop obtained accordingly is further referred to as *remanent* hysteresis loop. This kind of measurement reveals the retention characteristics of ferroelectric thin films.

Whereas the remanent loop is saturated for high values of the poling voltage, the in-field loop contains a linear part. The linear part can be used to estimate the electrostriction coefficient of the material, as shown in the next section.

It should be mentioned that rather recently the remanent hysteresis loop procedure was applied to macroscopic measurements, too ^[91]. Its main scope was to minimize leak charges and therefore to obtain more realistic polarization data even in very leaky ferroelectric samples.

4.3.4 Estimation of the electrostriction coefficient

The electrostrictive effect is present in all materials, regardless of the symmetry and is an example of nonlinear coupling between elastic and electrical fields. Generally, if an electric field E_i is applied to a material, the electrostrictive strain S_{ij} is defined by:

$$x_{ij} = M_{ijkl} E_k E_l \quad \text{Eq. 23}$$

The electrostrictive effect can also be expressed in terms of the induced polarization:

$$x_{ij} = Q_{ijkl} P_k P_l \quad \text{Eq. 24}$$

where the polarization-related electrostrictive coefficients Q_{ijkl} are given by:

$$M_{ijpq} = \chi_{ip} \chi_{lq} Q_{ijkl} \quad \text{Eq. 25}$$

In the case of ferroelectric materials, however, Eq. 23 and Eq. 24 are not simultaneously valid, due to the strong nonlinear dependence of the susceptibility tensor χ_{ij} on the electric fields. Experimental data have shown that the polarization-related electrostrictive coefficients Q_{ijkl} are, within the experimental errors, independent on temperature^[92] and electric field^[93,94]. For this reason they are mostly used for the description of the electromechanical properties of ferroelectric materials, though they were found to depend on the number of polarization switches in some cases^[95].

For a single-crystal ferroelectric in the monodomain state, Eq. 10a (Sect. 2.2) between the electric-field-induced strain along the z-axis x_{33} and the spontaneous polarization P_S is extended to include the effect of an applied electric field as follows^[96,97]:

$$x_{33} = \epsilon_{33} Q_{33} (2P_S + \epsilon_{33} E_3) E_3 \quad \text{Eq. 26}$$

The first term represents the linear, piezoelectric strain with respect to the external electric field E_3 . The second term is the pure electrostriction component of the strain. In Eq. 26 the electrostriction coefficient is written using the matrix notation.

The experimental setup used for piezoelectric measurements with a SFM allows the application of an AC signal biased by a DC voltage, and the detection of a certain harmonic (usually the first) of the mechanical response of the sample. Next, these experimental aspects will be taken into account to demonstrate a possibility for the estimation of the electrostriction coefficient. If we replace in Eq. 26 the electric field as shown in Eq. 27:

$$E_3 = E_{DC} + E_{AC} \sin(\omega t) \quad \text{Eq. 27}$$

the total strain induced can be written as:

$$x_{33} = x_0 + x_\omega \sin(\omega t) + x_{2\omega} \sin\left(2\omega t - \frac{\pi}{2}\right), \quad \text{where} \quad \text{Eq. 28}$$

$$\begin{cases} x_0 = \epsilon_{33} Q_{33} (2P_S + \epsilon_{33} E_{DC}) E_{DC} + \frac{1}{2} \epsilon_{33}^2 Q_{33} E_{AC}^2 \\ x_\omega = 2\epsilon_{33} Q_{33} (P_S + \epsilon_{33} E_{DC}) E_{AC} \\ x_{2\omega} = \frac{1}{2} \epsilon_{33}^2 Q_{33} E_{AC}^2 \end{cases} \quad \text{Eq. 29}$$

The longitudinal piezoelectric coefficient can be obtained as the amplitude of the first harmonic of the strain divided by the amplitude of the driving AC electric field:

$$d_{33} = \frac{x_{\omega}}{E_{AC}} = 2\epsilon_{33}Q_{33}(P_S + \epsilon_{33}E_{DC}) \quad \text{Eq. 30}$$

In Eq. 30 it can be seen that, for a constant ferroelectric polarization P_S , the dependence of the piezoelectric coefficient on the DC electric field is linear. On a $d(E)$ in-field hysteresis curve, the slope of this linear component can be obtained by differentiating Eq. 30 with respect to E_{DC} , for those regions of the hysteresis loop, for which the ferroelectric polarization is not switching (at saturation).

$$\frac{\partial d_{33}}{\partial E_{DC}} = 2Q_{33}\epsilon_{33}^2 \quad \text{Eq. 31}$$

The electrostriction coefficient can be estimated from the slope of the saturated regions of the in-field piezoelectric hysteresis loops provided the permittivity is known from other measurements. In principle, the electrostriction coefficient could be estimated from the second harmonic, too, if the noise level is low enough. The strain to be measured is proportional to the product $E_{DC}E_{AC}$ if the first harmonic is used, whereas it is proportional to E_{AC}^2 if the second harmonic is detected. The problems that arise are, first, that the AC voltage has to be smaller than the coercive voltage (to prevent switching), and second, that a higher AC voltage may produce breakdown in the film. In contrast, using a high DC voltage avoids these problems.

5. Results

5.1 BaTiO₃ single crystals – a verification of the method

Barium titanate, the ferroelectric activity of which was independently discovered in 1944 by von Hippel et al. [98] and in 1945 by Wul and Goldman [99], is one of the best-studied ferroelectric materials, due to its simple structure, large permittivity, and chemical stability. The crystal structure is cubic perovskite above the Curie temperature, and slightly distorted below. At room temperature, the crystal structure is tetragonal, having an electric dipole along the polar axis. To minimize the total energy, the crystal splits up into domains, which can have the spontaneous polarization along one of the three crystallographic directions. Moreover, the charge neutrality condition restricts the *equilibrium* domain structure, allowing only 180° or non-charged 90° domain walls. Therefore, due to its predictable and simple domain structure, BaTiO₃ is a perfect material to check the capabilities of piezoresponse SFM.

5.1.1 Macroscopic measurements

Several pieces of a Remeika-grown BaTiO₃ (100) single crystal* [100] were glued with silver paste on a conductive support, which plays the role of the bottom electrode. At first the macroscopic properties were measured using a silver paste as top electrode.

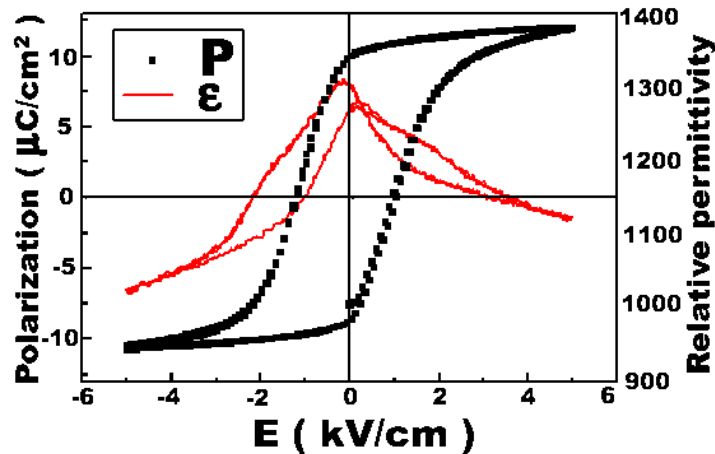


Figure 17 Macroscopic measurement of the polarization and permittivity hysteresis loops of a BaTiO₃ (100) single crystal. The sample proved to possess a non-negligible surface percentage of *a*-domains.

Figure 17 shows the polarization and the permittivity as a function of the bias voltage. The polarization hysteresis loop was measured using a usual Sawyer-Tower circuit [101] with a linear capacitor $C_0 = 4.74 \mu\text{F}$ (about $4 \cdot 10^4$ times higher than the small signal capacitance of the $8.3 \cdot 10^{-3} \text{ cm}^2$ tested area of the sample). The frequency of the cycling bias was the same (2.5 mHz) for both polarization and permittivity hysteresis loops. The permittivity was

* Samples were provided by Prof. Lukas M. Eng (IAPP – TU Dresden)

measured with a small AC field (0.05 kV/cm at 9.7 kHz) superimposed on the DC bias. The rather small value of the saturation polarization of $12 \mu\text{C}/\text{cm}^2$ and the high permittivity of 1300 can be attributed to the presence of a large percentage of a -domains. These domains do not contribute to switching because the switching of one of them would imply a sequence of additional reversals that would be energetically unfavorable (due to the high stress involved). However, the ferroelectric characteristics are in the range reported by other authors ^[102]. As it will be shown later, the piezoresponse images indeed revealed that the a -domains cover a large part of the crystal surface.

5.1.2 Ferroelectric domain structure

Figure 18 shows the topography and the deduced components of polarization at the sample surface. Topographic data show surface steps, about 30 nm in height, which have no correlation with the actual ferroelectric domain structure. Most probably, at the crystal growth stage, these steps indeed reflected the pattern of 180° domains, but the present equilibrium domain structure is very different ^[103].

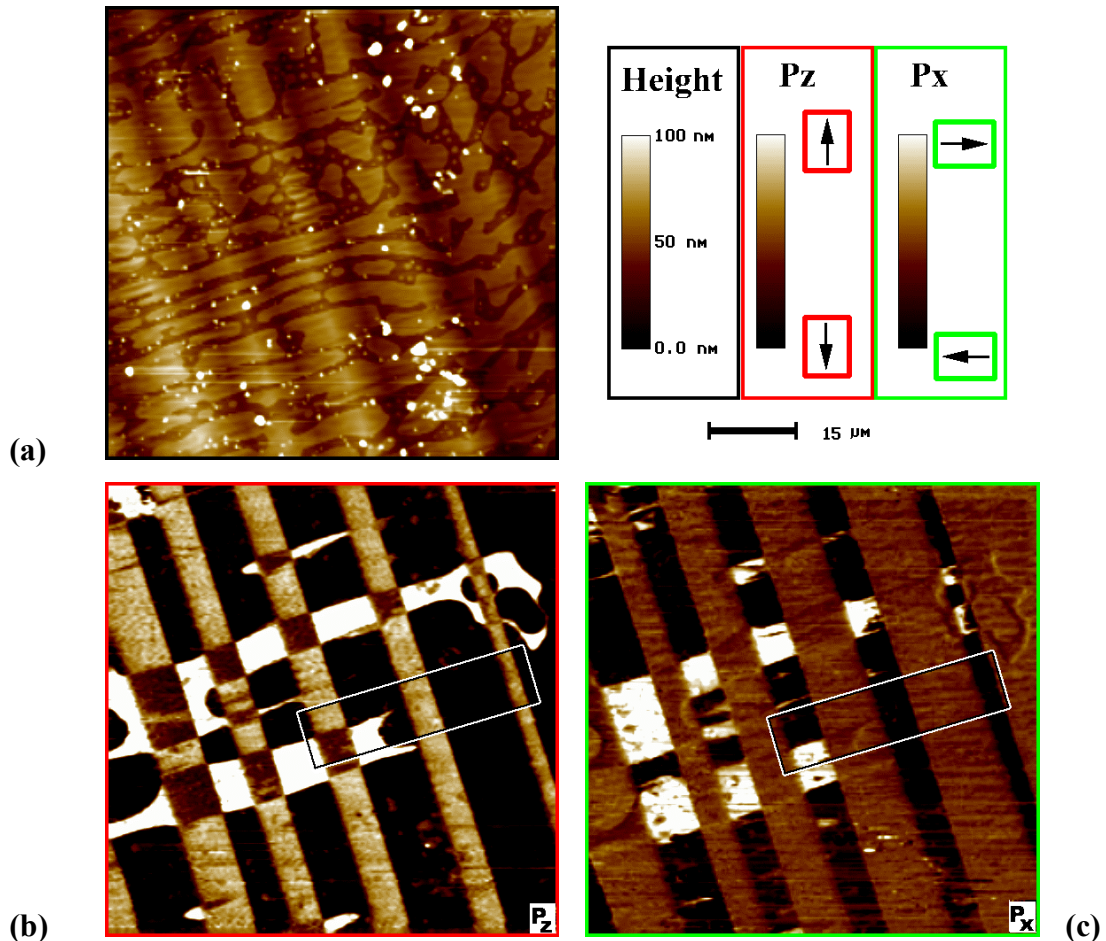


Figure 18 (a-c) Topography (a), out-of-plane (b) and in-plane (c) piezoresponse images at the surface of a barium titanate (100) single crystal (scan size: $75 \mu\text{m}$). The legend shows the deduced polarization orientations.

The images (b) and (c) in Figure 18 display the out-of-plane and in-plane ferroelectric domains at the BaTiO₃ surface for the same region. Even at the first look the complementarity of the two images is visible: regions with high P_Z -contrast (black or white color in image b) exhibit zero P_X -contrast (gray color in image c). In other words, a certain point of the surface can have a polarization either perpendicular *or* parallel to the surface, in complete agreement with the crystallographic orientation of the sample.

The polarization direction was deduced from the phase shifts of the signals. To analyze the compatibility of the in-plane and out-of-plane domain structures deduced from the images with the additional conditions of a stable domain structure in perovskites, the area framed in these images is zoomed in Figure 19 and a three-dimensional sketch of the ferroelectric domains is drawn. The head-to-tail configuration is fulfilled for each 90°-domain wall over all areas that were probed. It was also deduced that 180°-domain walls are always parallel to the spontaneous polarization direction, that is they can cross continuously the a - and c - domains, but they are not allowed to end within an a -domain since this will break the condition of charge neutrality.

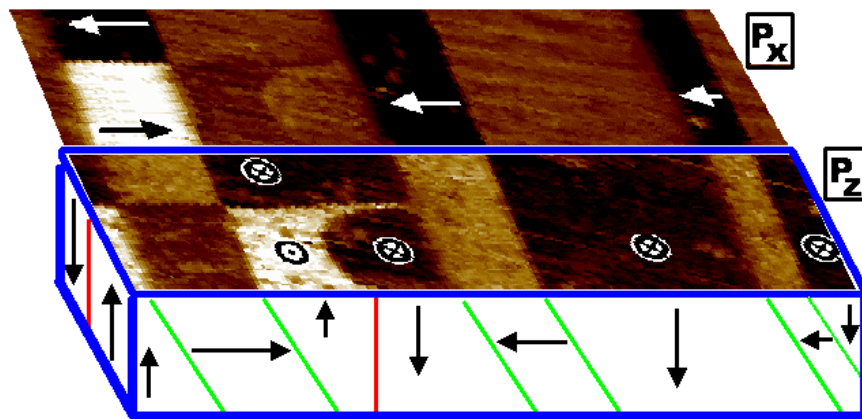


Figure 19 The ferroelectric domain structure in the rectangular region framed in Figure 18b-c, as deduced from the out-of-plane and in-plane piezoresponse images.

5.1.3 Control of ferroelectric domains

Simply detecting a signal and converting it into colors was not considered sufficient to yield full confidence in the system capabilities. In the particular case of piezoresponse SFM the tip movements are strongly dependent on the interaction with the surface and this may cause image artifacts. For the case of ferroelectric materials the detection system can be further checked by modifying the domain structure, applying a DC bias to the sample. Comparing the piezoresponse images before and after switching should give additional confidence in the setup. For instance, many of the BaTiO₃ samples investigated were in the single domain state and thus no contrast in the piezoresponse image was detected. Therefore, evidence of domain switching is a complementary requirement for the verification of the method.

Writing ferroelectric domains over large areas was achieved by scanning the sample surface at an applied bias voltage which exceeded the coercive voltage. The result of one such experiment is shown in Figure 20. The sample (probed in different places of the surface) was

single domain (negatively polarized) and no contrast could be detected. First an area of $50 \times 25 \mu\text{m}^2$ was switched upward while scanning the surface with a voltage of 80 V on the bottom electrode. The middle of this domain was then switched back by applying a pulse voltage of -80 V, 0.5 s with the tip fixed above the surface. The images (a) and (b) in Figure 20 represent the topography and the out-of plane piezoresponse images, respectively, recorded simultaneously after the domain “writing”. An important aspect is that *no change in the topography is associated with the 180° polarization switching*, that is, the 180° domain walls are free of stress. The domain formation in BaTiO₃ single crystals was systematically analyzed in Ref. [104]. The lateral size of the domains was found to depend strongly on the magnitude of the electric field and the pulse length. The $5 \mu\text{m}$ lateral size of the domain produced by the negative pulse in this experiment agrees with the dependence of domain size on pulse duration found in Ref. [104].

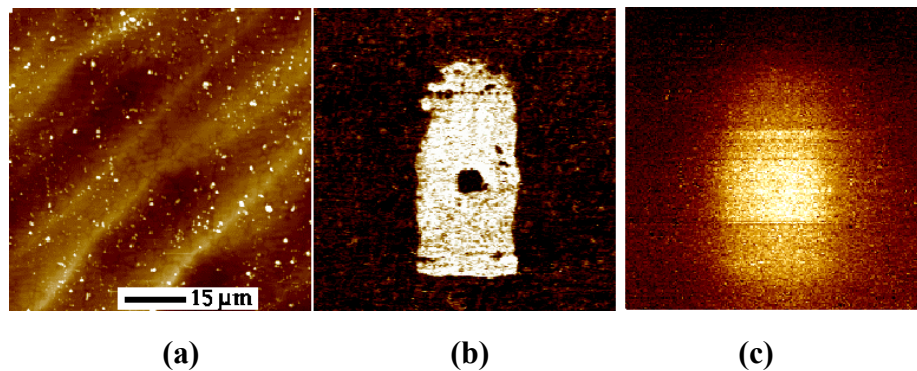


Figure 20 Switching the out-of-plane polarization at the BaTiO₃(001) surface. (a) Topography, z-scale 200 nm. (b) piezoresponse image and (c) non-contact EFM image after switching. Note the low resolution of non-contact EFM due to the field spreading and screening charges.

The same area was then scanned again in the non-contact mode with AC modulation (EFM-mode). As shown by the image in Figure 20c, the large ferroelectric domain is still visible, but with a very low lateral resolution. The small domain in the center is not resolved anymore. This can be explained by the fact that a certain amount of charges accumulated at the surface from the ambient atmosphere screen the polarization at the surface [29]. Also, the decrease and spreading of the electric field, and implicitly of the electric field gradient, above the surface has the same consequence [105,106].

The lateral resolution is an important parameter that has to be taken into account when interpreting domain images. In contact mode it is limited only by the contact area, which usually doesn't exceed 100 nm in lateral size, and therefore this mode is superior to the non-contact detection modes, as readily exemplified in Figure 20b-c.

5.1.4 Local measurements

Local piezoelectric hysteresis loop measurements above a *c*-domain are presented in Figure 21. The values of the piezoelectric coefficient are calculated using Eq. 22 as described in Sect. 4.2 and ranges from 4 to 6 pm/V. A few possible reasons for the very small values measured, compared to 86 pm/V in bulk BaTiO₃ are discussed in Chapter 6 (Sect. 6.2).

Analyzing the shape of the hysteresis loops in Figure 21, the effect of the measuring procedures, described in Sect. 4.3, can be easily noticed. The in-field loop contains a linear part, which reflects the field-induced polarization, i.e. the effect of the permittivity (second term in Eq. 26, Sect. 4.3). At this point it may be objected that the linear part should not exist, since it is known from the macroscopic measurements that the permittivity decreases at high fields (as also happened in BaTiO₃, Figure 17). The dielectric nonlinearity, however, is associated with domain wall contributions^[8]. In nanoscale measurements, the small area that is probed is supposed to be single domain, and it is very unlikely that the domain wall contribution is involved in the switching processes induced under the SFM tip. This implies that the macroscopically measured permittivity cannot be substituted in Eq. 26, Sect. 4.3 to determine the dependence of the longitudinal piezoelectric coefficient on the applied electric field. For this purpose the *intrinsic* permittivity has to be considered^[107,108], which is related to the lattice polarizability and not to the domain wall motions. As a consequence, the saturation parts of the piezoelectric loop appear linear. In contrast, the remanent loop shows a well-defined saturation of the piezoelectric coefficient that agrees well with the zero field value of the in-field loop.

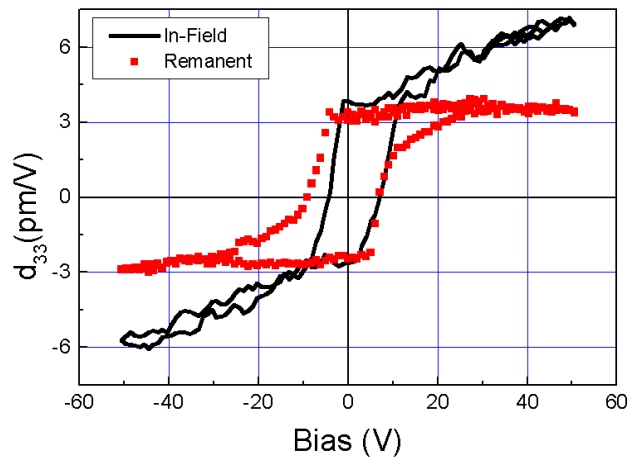


Figure 21 Nanoscale piezoelectric hysteresis loops at the surface of BaTiO₃(001). The cycling parameters are: $N_{pis}/\text{cycle} = 200$; $T_{bias} = 0.4$ s, for both loops, and $T_{delay} = 2$ s for the remanent loop. The testing voltage had an amplitude of $V_{AC} = 2$ V and a frequency $f = 19.4$ kHz.

It is important to note the differences in the shape of the loops near the coercive field, in the region where switching occurs. While the field is applied, the polarization under the tip switches rather fast, resulting in a steep slope of the loop at the coercive field. If the electric field is only shortly applied, it results in a sharp but incomplete reversal of the signal, above which the saturation value is reached with a smaller slope. This can be explained by the fact that a domain is only nucleated by a pulse having the amplitude of the coercive voltage, but the size of this domain is smaller than the region contributing to the piezoresponse signal, resulting in *stable* intermediate piezoresponse values. Further application of pulses leads to a growth of the domain, which needs more energy to further grow as its size increases, and therefore to a decrease of the slope above the coercive voltage. This is in agreement with other switching experiments on BaTiO₃ single crystals^[85, 104].

In conclusion, measurements on BaTiO₃ single crystals have proven that

- the signals detected are related to the converse piezoelectric effect and not to the charges on the surface or to other artifacts;
- the orientation of the polarization is correctly deduced from the piezoresponse signals;
- the numerical values calculated from piezoelectric data are considerably lower than the known (bulk) values, but the measuring conditions were shown to be extremely different from the usual ones. In principle, it should be very easy to “calibrate” the setup and to scale all piezoelectric measurements considering BaTiO₃(100) as a standard, but such a simple approach would hardly describe the rather complex nature of the measurement procedure.

5.2 New results on PZT films

A problem of current interest in ferroelectric research is to know how the domain structure and the other properties of a material are modified if the ferroelectric material, in thin film or ceramic form, consists of very small grains. This question is particularly significant for PZT, a solid solution between the simple perovskites PbZrO₃ and PbTiO₃, in view of its broad application in different fields of technology. For instance, the piezo-scanner of the SFM head itself is made out of a PZT ceramic. And PZT is still a candidate for use in the prospective FeRAMs, with certain special electrodes. For basic properties and further reading, see Ref. [102].

The composition of the PZT films used in this study was 30/70 (Zr:Ti atomic ratio), therefore the crystallographic symmetry was tetragonal. The films were deposited on Pt/SiO₂/Si substrates, and for macroscopic measurements Pt top electrodes were sputter-deposited onto the surface.

5.2.1 Macroscopic measurements

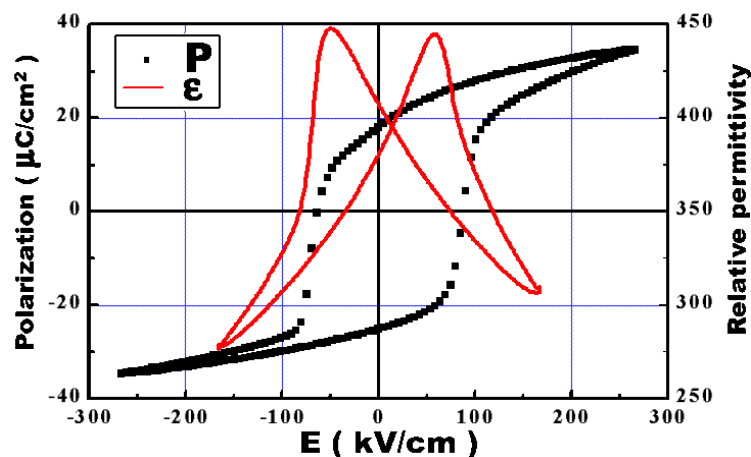


Figure 22 Macroscopic measurements of the polarization and permittivity hysteresis loops of a PZT (30/70) thin film.

Macroscopic ferroelectric measurements presented in Figure 22 reveal a coercive field and a remanent polarization of the order of $2E_c = 150 \text{ kV/cm}$ and $2P_r = 44 \mu\text{C/cm}^2$, respectively, comparable to the literature values for films with similar composition [109,110]. The asymmetry of the loops seen in Figure 22 was not found in the nanoscopic measurements. Therefore, it may be attributed to the different types of interfaces between the film and the bottom and top electrodes caused by the different ambient conditions during the formation of the two contacts: the depositions of the film on the bottom electrode, and that of the top electrode on the film.

5.2.2 Ferroelectric domain structure

The film morphology studied by SFM and SEM exhibits grains with a lateral size from 300 nm up to 600 nm and a surface roughness of 10 nm . Since the film thickness is 500 nm , it is reasonable to conclude that the films have a columnar structure, making the study of ferroelectric domains easier.

When studied by piezoresponse SFM the films show a complex domain structure implying the presence of both 180° and 90° domain walls. The images in Figure 23, acquired with a very sharp tip at a low contact force* of $0.4 \mu\text{N}$, illustrate the existence of a very fine domain structure with lateral domain sizes of less than 10 nm .

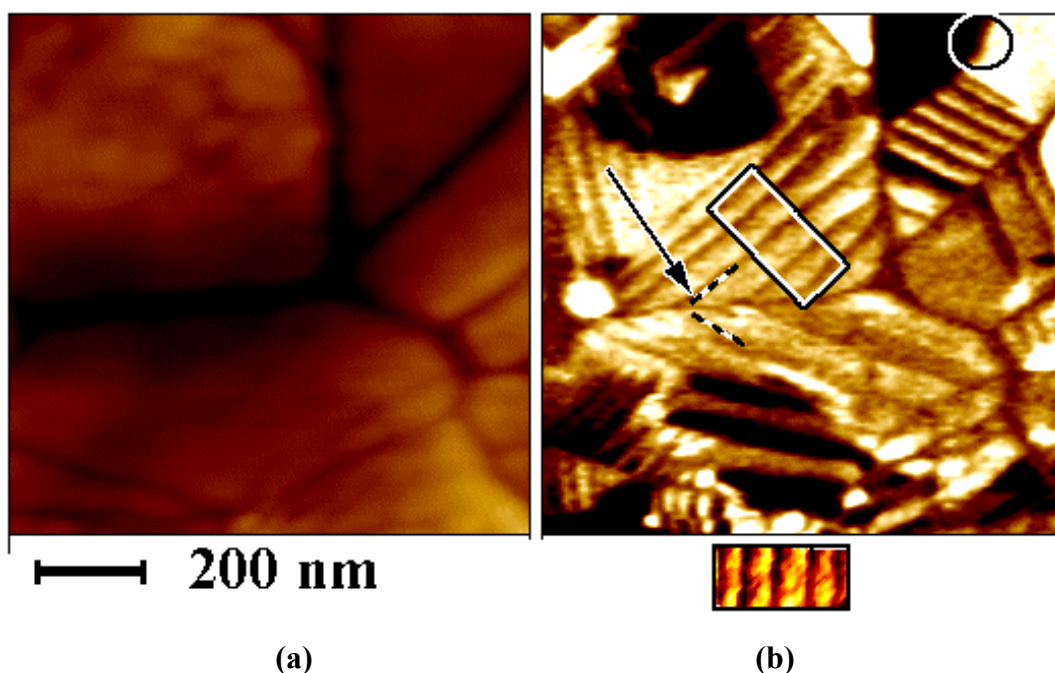


Figure 23 (a,b) Topography (a) and out-of-plane piezoresponse (b) images of an as grown PZT (30/70) film revealing a complex domain structure, with mainly 90° domain walls. A 180° domain wall is marked with a circle in the upper right corner. The contrast inside the rectangular frame is similar to the one in Figure 19 and belongs to an *a-c*-type configuration of the domain structure (with 90° domain walls).

* If the contact force between tip and surface is high, the radius of the tip apex deteriorates rapidly (most probably already at the engagement) from $5 - 10 \text{ nm}$, as guaranteed by the manufacturer, up to $30 - 50 \text{ nm}$, lowering the lateral resolution.

Although the image of Figure 23b shows the out-of-plane domains, different levels of the signal are associated with different z-components of the polarization (more details, see Appendix B). Therefore, regions with another polarization orientation than normal to the surface can be deduced from the contrast intensity. An important feature that can therefore immediately be observed is that both out-of-plane and in-plane ferroelectric domains coexist within the same grain of less than $1 \mu\text{m}^3$, just as in the case of large single crystals of BaTiO_3 .

It is noticeable that 90° domain walls often pass continuously through the grain boundary, as, e.g., at the boundary marked with an arrow. It appears also that domain walls do not necessarily coincide with grain boundaries, some domains may extend into the adjacent grains. This fact is better illustrated in Figure 24, where the arrow shows a grain boundary crossed by a positive domain. These observations indicate a strong coupling between the (ferroelectric or ferroelastic) domains that belong to different, adjacent grains. Other details of Figure 24 are discussed in the next sections.

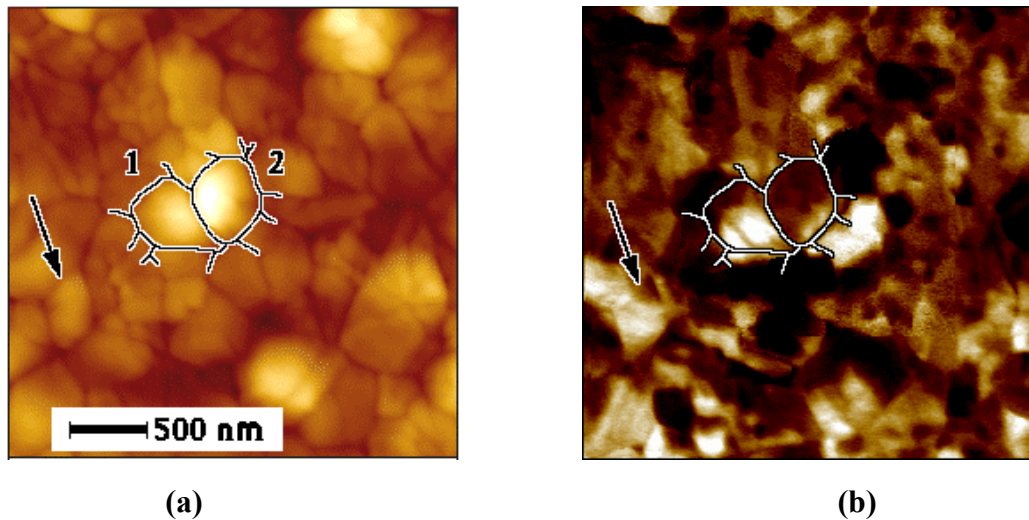


Figure 24 (a,b) Topography (a) and out-of-plane piezoresponse (b) images of an as grown PZT film. The arrow shows a domain extending over two grains.

5.2.3 Characterization of individual grains

A local ferroelectric characterization was achieved by positioning the SFM tip on top of selected individual grains and recording piezoelectric hysteresis loops. A ferroelectric behavior was found for all the grains that were probed, however, the hysteresis parameters and loop shape significantly vary from grain to grain, even for adjacent grains. The results for the two grains outlined and numbered in Figure 24 are now presented.

The hysteresis loops of the two grains are shown in Figure 25. The cycling parameters used are $N_{pts}/\text{cycle} = 200$, $T_{bias} = 0.3$ s, for all loops, and $T_{delay} = 2$ s for the remanent loops. The values of $7 \text{ pm}/V$ (grain No. 1) and $15 \text{ pm}/V$ (grain No. 2) calculated for the saturation piezoelectric coefficients are 10 – 20 times smaller than the bulk values but are similar to those reported from other SFM measurements^[66,90,111] and about 2 – 4 times smaller than macroscopic values measured in thin films^[107,112].

The in-field and remanent hysteresis loops give an information on the evolution of the domain under the tip induced by an applied poling voltage. Analyzing the hysteresis loops in Figure 25, it is obvious that switching of domains under a continuously varying electric field occurs at a lower field, but with a smoother slope than in the case of the remanent loop. The latter one contains information about the “relaxed” state of ferroelectric domains that were formed with a given pulse. The results show that there is a strong dependence of the switching on the waveform of the electric field applied and that switching occurs much faster under a pulse with an amplitude which is higher than the coercive field. It is believed that if a low electric field (below the coercive field) is applied over a (very) long time period the polarization will eventually switch^[8,113], or, equivalently, the coercive voltage will be smaller for longer applied voltages^[114,115]. In the present measurements, however, no significant differences were found for bias times longer than the lower limit of 0.1 s*.

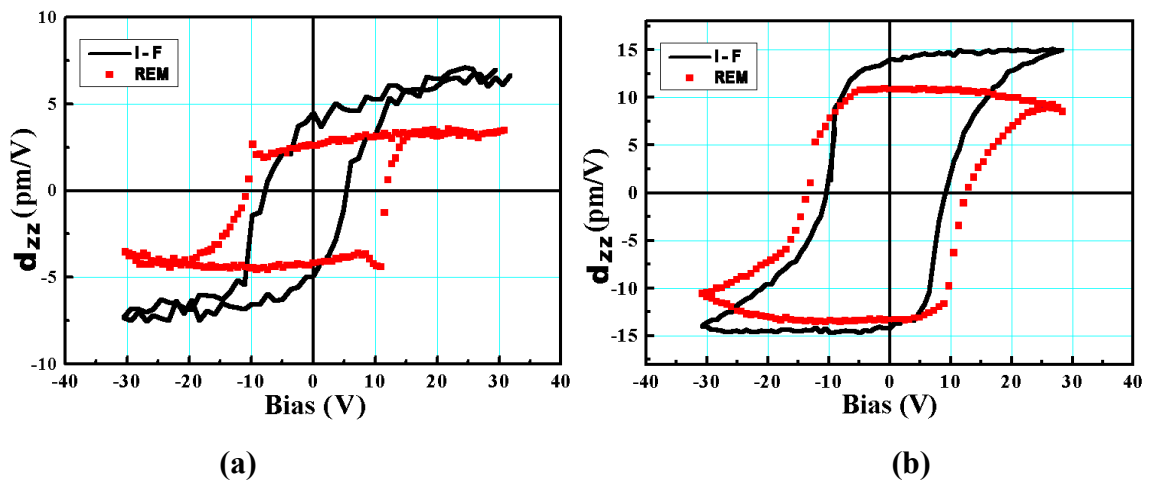


Figure 25 In-field (I-F) and remanent (REM) piezoelectric hysteresis loops of the grains indicated in Figure 24: (a) grain No. 1, and (b) grain No. 2.

The relationship between the magnitude of the piezoresponse signal and the spontaneous polarization is an important problem in piezoresponse imaging, relation that can be established assuming different crystallographic orientations of the grains. In the following, the *exact* dependence of the piezoresponse on the crystallographic orientation will be exemplified using the two grains shown in Figure 24. Comparing the parameters of the remanent hysteresis loops (Figure 26a), it appears that although the grain No. 1 of Figure 24b seems to exhibit an initial piezoresponse signal larger than grain No 2, the saturation piezoelectric coefficient induced by the applied field is less than 40 % of that of grain No. 2. Piezoresponse images acquired after poling (not shown here) have indeed confirmed that the contrast of grain No. 2 is higher than that of grain No. 1.

To explain the difference in the magnitude of the piezoresponse of the two grains (at *saturation*), let us assume that they have a different orientation, and the *c*-axis of the two grains (and thus also the spontaneous polarization) form the angles θ_1 respectively θ_2 with the normal to the film plane. The magnitude of the effective piezoelectric coefficient depends on

* Usually the time constant of the lock-in amplifier has to be set to 20 ms. The manufacturer recommends a waiting time about 10 times longer to obtain an accurate measurement.

the angle between the measurement direction and the crystallographic c -axis as described in Appendix B, $d_{zz} = d_{zz}(\theta)$. For the case of a tetragonal symmetry and the particular values of d_{33} , d_{31} and d_{15} for tetragonal PZT(60/40) in standard orientation, the maximum of $d_{zz}(\theta)$ appears for $\theta = 0$ and is $d_{zz}(0) = d_{33}$. If now we take into account that the piezoresponse is always measured along the direction normal to the film plane (direction associated with the z -axis in Figure A 4a in Appendix B) and that experimentally $d_{zz1} < d_{zz2}$, it results $\theta_1 > \theta_2$ for the orientations of the two grains. Figure 26b illustrates how the crystal orientation dependence of the longitudinal piezoelectric coefficient can be used to explain the variations in magnitude of the piezoresponse signal. In the calculation the data given in ^[116] were used.

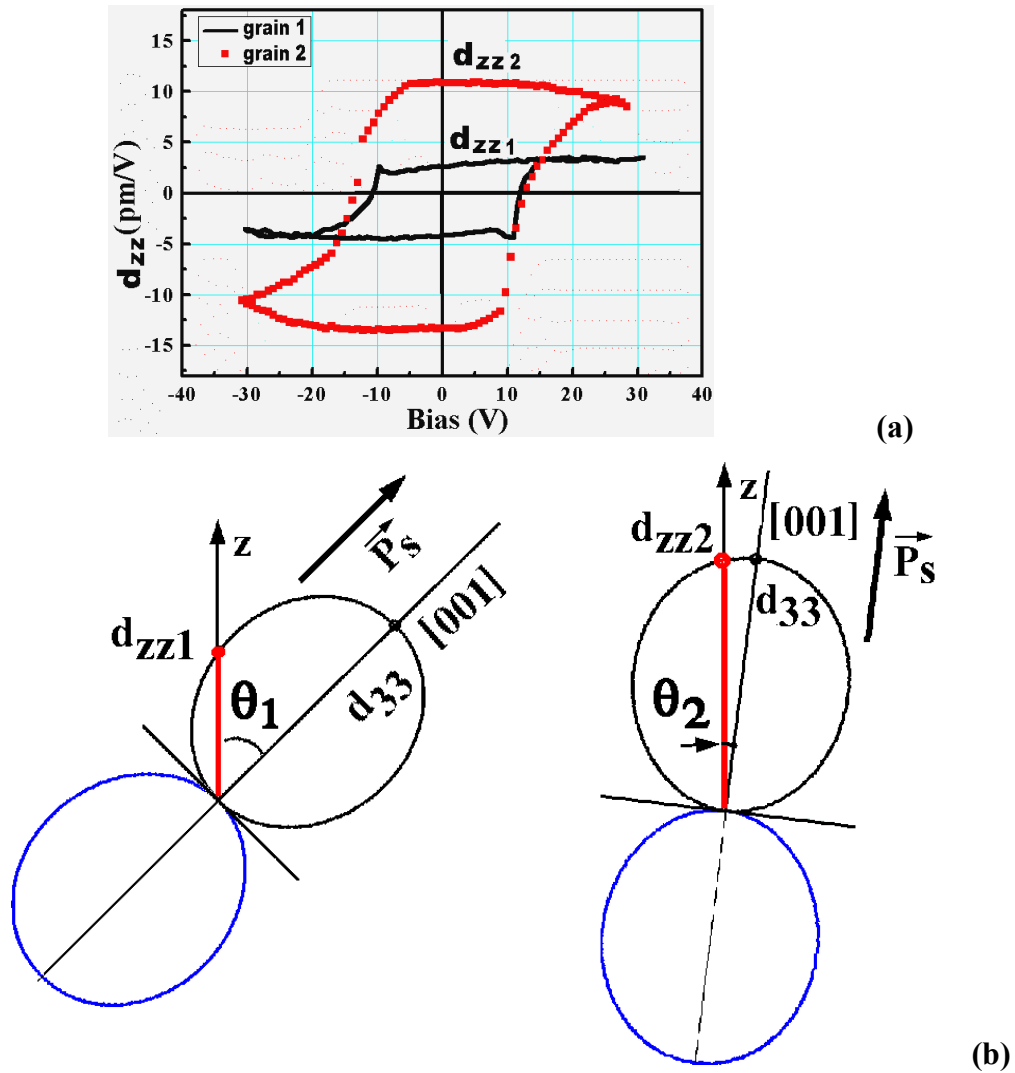


Figure 26 (a) Comparison between the remanent piezoelectric loops of the grains marked in Figure 24. (b) Drawings illustrating the variation of the measured effective piezoelectric coefficient with the crystallographic orientation of the grains.

It should be kept in mind that the above conclusion holds only for the saturated regions of the loops and does not take into account the polarization switching. However, *for a given orientation*, the effective piezoelectric coefficient is still proportional to the spontaneous polarization, since all coefficients d_{33} , d_{31} and d_{15} are directly related to P_s , according to Eq. 10 ^[10,117]

The above considerations can be summarized as follows: Up to now it was well known that the magnitude of piezoresponse depends on the crystallographic orientation of the grain, but the exact origin of this dependency has not been pointed out. Usually it was suggested that the piezoresponse depends on the component of the spontaneous polarization normal to the film plane ^[104,118]. However, here it is established that the exact nature of the relationship $d_{zz}(\theta)$ is governed by the transformation rules of the whole piezoelectric tensor, which only in the case of a tetragonal symmetry is closely related (*but not proportional!*) to $P_Z = P_S \cos(\theta)$. For instance, for the case of rhombohedral PZT it is expected that piezoresponse is at maximum for an orientation close to $[100]$, and not for the $[111]$ -orientation, ^[119] along which the spontaneous polarization is directed (eventually after poling).

5.2.4 Approaching the ferroelectric switching

Of particular interest in the study of the ferroelectric switching processes is to determine how the domain formation and their evolution occur under certain conditions, in particular under electric field pulses. In the case of SFM measurements, due to the long time necessary for the acquisition of the images, this can be achieved only if the investigated process is slow enough. Alternatively, if several *equivalent* places of the sample are available, they can be exposed to different voltage pulses and the images of the induced domains can give information about the switching scenario. Such places can be easily found on single crystalline samples, but in the case of polycrystalline films, because of their inhomogeneity, this is practically impossible.

However, information about polarization reversal can be obtained by correlating the voltage applied to the investigated site with the subsequent domain image of the surrounding region. To ensure a definite and reproducible ferroelectric history of the grain, the grain should be cycled between the positive and negative saturation states (as they appear in the hysteresis loop) and only afterwards the sweep voltage should be stopped at the value of interest. Additionally, it has to be assumed that all polarization states remain the same from one major cycle to another.

Such an experiment is presented in Figure 27 and Figure 28. Experiments have shown that grains of 500 nm or less in lateral size are entirely switched when they are in the saturated positive or negative state. Figure 27b shows the domain structure of the same grains from Figure 24, corresponding to the positive saturation of grain No. 1 and the negative saturation of grain No. 2. Compared with the domain image of Figure 24b the growth of the induced domains into the adjacent grains is obvious (both positive and negative regions cross the grain boundaries and extend into the neighboring grains).

An image of the polarization reversal process can be obtained if the bias voltage sweep is stopped during the sweep in the vicinity of the coercive voltage on the hysteresis loop. This approach is presented in Figure 28. Having the SFM tip positioned at the place marked \square in the topographic image of Figure 28a, the bias cycling was stopped after having first ended one complete loop, at $V_{bias} = 15 V$, coming from the negative saturation, as indicated on the hysteresis loop in Figure 28b. The piezoresponse image of Figure 28c recorded subsequently

can be considered as an intermediate stage of the grain switching towards the positive state^{*}. The formed positive domain, about 200 nm in length and 130 nm in width, indicates that the switching processes occur through nucleation and growth of opposite domains. In this case, the nucleation center is exactly the place where the electric field was applied.

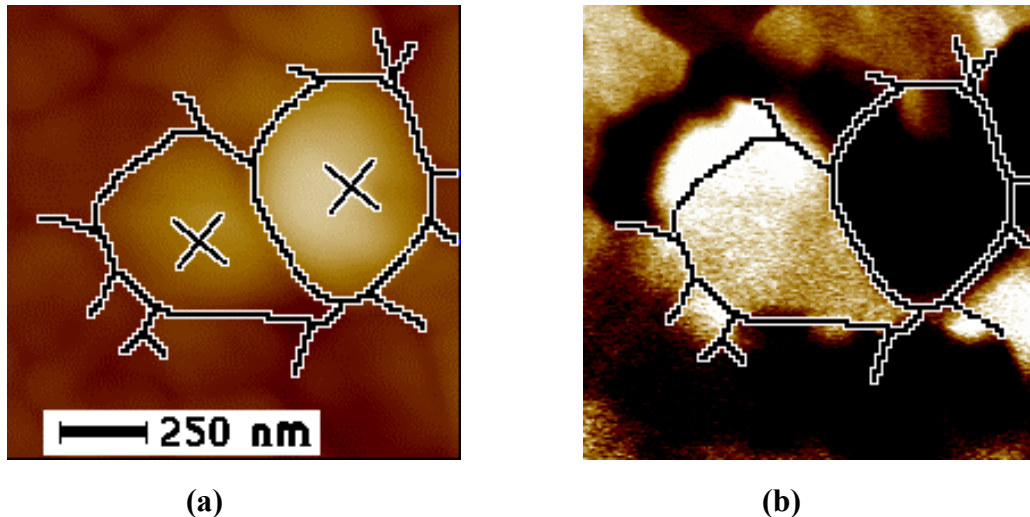


Figure 27 (a,b) Topography (a) and out-of-plane piezoresponse (b) images showing the full poling of the grains shown in Figure 24 (negative poling of grain No. 1 and positive poling of grain No. 2). The induced domains extend over the entire grain, even if the SFM tip was positioned at the center of each grain, as indicated by the crosses. Moreover, the domains cross the grain boundary and grow into the neighboring grains.

The switching scenario was found to depend on the probing location. The grain was again brought to negative saturation, and the same procedure was applied only 100 nm away, at point 2 in Figure 28a. Figure 28d shows the resulting domain image after interrupting the positive poling near the coercive field. A completely different domain has grown this time, suggesting that nucleation has occurred at the probing place too, but the nucleated domain has taken a triangular shape, extending up to the grain boundary and merging with a small positive domain in the neighboring grain (indicated by arrow). This domain, which does not appear in previous images (for example in Figure 27b) was formed during the repeated switching of the grain No. 2 (as seen on intermediate images, not shown here). Being located at the intersection of three grain boundaries, it may be assumed that it has been trapped in what seems to be a stable position. Such a pinned center is known to extend in lateral size by trapping other domains that participate in the switching process^[5]. In fact this could be the incipient state of the fatigue process, seen on the mesoscale.

In conclusion, the switching experiments revealed that switching occurs *via* nucleation and growth of opposite domains, processes that are well known. The most important result is that the switching scenario was found to be very much dependent on the specific location where polarization reversal nucleates, and that this dependency was found to extend over hundreds of nanometers without any reliable possibility to avoid it.

^{*} However, it should be remembered that this is not a real *dynamic* switching, since this is a (meta)stable domain state.

The further shrinkage of ferroelectric devices, down in the submicron range, requires a very good homogeneity of the ferroelectric properties at this scale. As our results show, the switching properties are not at all homogeneous on this scale, so that polycrystalline films are not suitable for this purpose.

This is the reason why our attention further on has been focused on another type of films, namely *epitaxial* ferroelectric films.

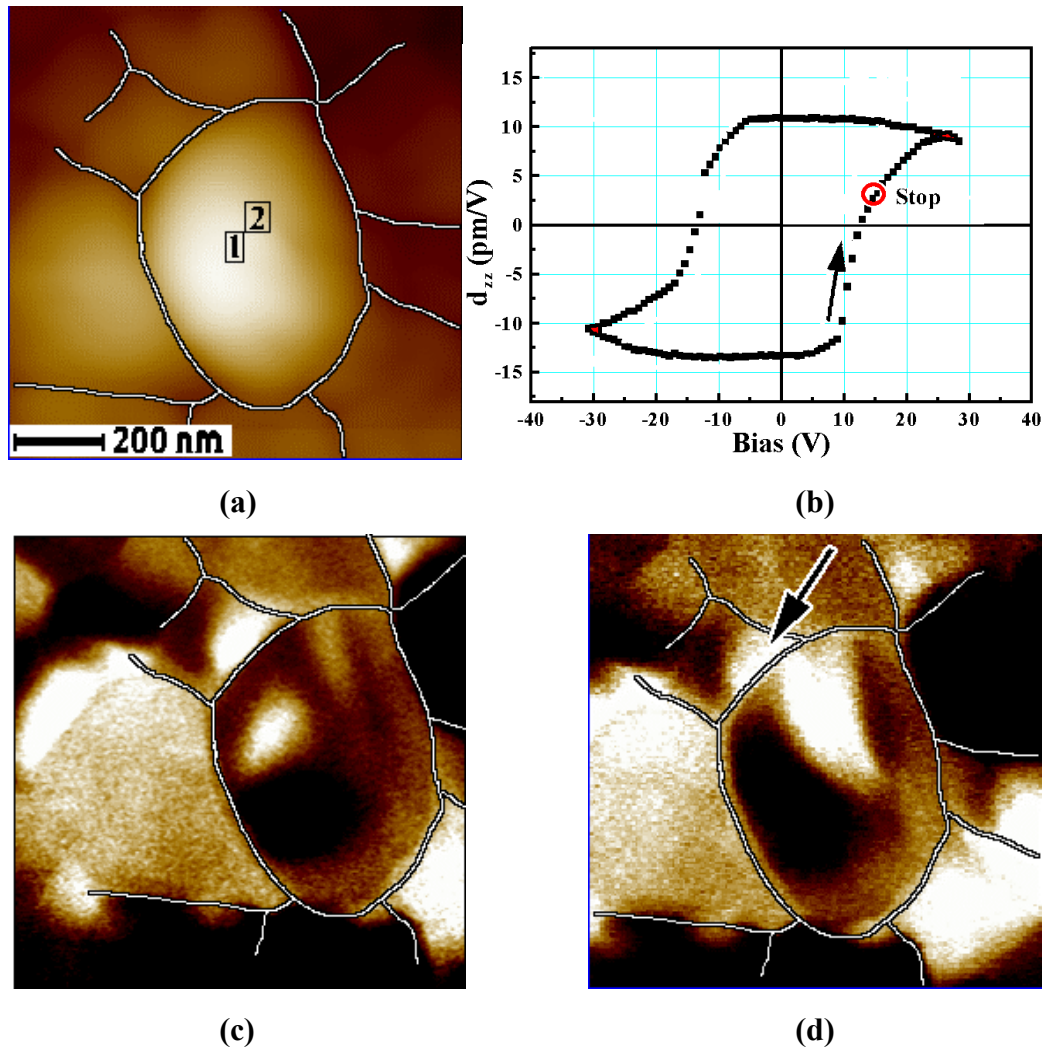


Figure 28 Polarization reversal in a PZT grain and dependence on the tip position. **(a)** Topography, showing the grain and the places where the tip was positioned during the hysteresis loop cycling. **(b)** Hysteresis loop of the grain, showing the position of the last voltage applied before imaging. **(c,d)** Out-of-plane domain images showing intermediate stages towards the positive switching corresponding to the tip positions **1** and **2**, respectively.

5.3 Bismuth-layered perovskite thin films: Anisotropy of ferroelectricity

5.3.1 Why bismuth-layered perovskites?

In memory applications of ferroelectric materials, writing and in many cases reading of the data imply a switching of the polarization. Each capacitor cell of the prospected ferroelectric RAM should therefore maintain the switching characteristics over its lifetime, i.e. for at least 10^{12} switching cycles [120]. One of the most important limitations of ferroelectric films with a simple perovskite structure like the $\text{Pb}(\text{Zr},\text{Ti})\text{O}_3$ family is the decrease in the amount of switchable polarization as a function of the number of switching cycles, a process called “fatigue”. Typically, the amount of the charge switched (the difference between the two remanent polarization values multiplied by the capacitor area) decreases by a factor of two after 10^7 switching cycles [120,121,122], a process which causes failure in reading the state of the memory cell.

One way to overcome this problem to some extent is to replace the commonly used metallic electrodes of the capacitor cell. By using oxide electrodes instead of metal electrodes the screening of the applied electric field by charges (e.g. oxygen-vacancies from the film) accumulated at the electrode-ferroelectric interface is avoided [123,124], but this often leads to DC-leaky capacitor devices [125,126].

Another way to provide a competitive memory device is to replace not the electrode, but the ferroelectric material. The most promising candidates for use in FeRAMs, to replace the PZT-based materials, are the *Bi-based layer-structured ferroelectric oxides (BLSFs)*. The latter are known to be free of polarization fatigue up to 10^{12} cycles of polarization switching [124,127]. The high fatigue resistance of these oxides seems to be due to two factors. First, their highly anisotropic crystal structure imposes the spontaneous polarization to be along (or almost along) the crystallographic a_{orth} direction, thus considerably reducing the number of 90° domain walls. The latter are known to be responsible for the main fatigue mechanism in materials with large tetragonal distortion [128,129,130]. Second, the crystal chemical structure of the BLSFs seems to prevent an extensive oxygen vacancy diffusion towards the metal electrodes which, in turn, reduces the accumulation of space charges in the ferroelectric material. This is advantageous, since under repetitive switching any free charges may accumulate at the domain walls, thus pinning them and therefore reducing the number of domains participating in the switching [124]. A further advantage is an ecological one, namely that the use of BLSF will reduce the usage of lead or lead-containing products in the industry. Therefore, although the spontaneous polarization of the BLSFs is smaller than that of the PZT-based materials, they are seen as the most promising candidates for use in microelectronics.

5.3.2 Crystal structure and macroscopic properties of BLSF materials

The BLSF oxides were discovered in a comprehensive study of bismuth compounds by Aurivillius in 1949 [131]. This family of compounds (also named the Aurivillius family) has the general formula $(\text{Bi}_2\text{O}_2)^{++}(\text{A}_{n-1}\text{B}_n\text{O}_{3n+1})^{--}$. The structure consists of $(\text{Bi}_2\text{O}_2)^{++}$ layers interleaved

with n perovskite-like oxygen octahedra. “ n ” is further referred to as the “Aurivillius parameter”.

It was found that the Bi^{3+} ions in the Bi_2O_2 layers could hardly be substituted by other ions so that the Bi_2O_2 layers are very stable. In contrast, the A- and B-type ions in the perovskite layers are easily replaced by a large number of univalent, divalent and trivalent cations. The ferroelectricity in these compounds was only later discovered, by different groups [132,133,134,135]

In the high temperature phase (paraelectric phase) all members of the family have a tetragonal structure. At room temperature it was found that the crystal structure of most of the BLSFs can be described by an orthorhombic unit cell. A difference was found, however, between compounds with an odd and an even Aurivillius parameter. It appears that compounds with odd n have the point group symmetry $B2cb^*$, whereas even-layered members belong to the point group $A2_1am$ [136]. Sometimes, for simplicity, a pseudotetragonal description is used [133,134]. In this study the orthorhombic description is exclusively used.

The spontaneous polarization in the BLSFs lies mostly in the plane of the Bi_2O_2 layers. For strontium bismuth tantalate ($\text{SrBi}_2\text{Ta}_2\text{O}_9$, SBT, $n = 2$), which is one of the most studied materials in the family, refinements of the structure revealed that the polarization is exactly along the crystallographic a -direction [137,138]. The structure of SBT is shown in Figure 29, viewed along the b -axis (a), and along the a -axis (b), respectively.

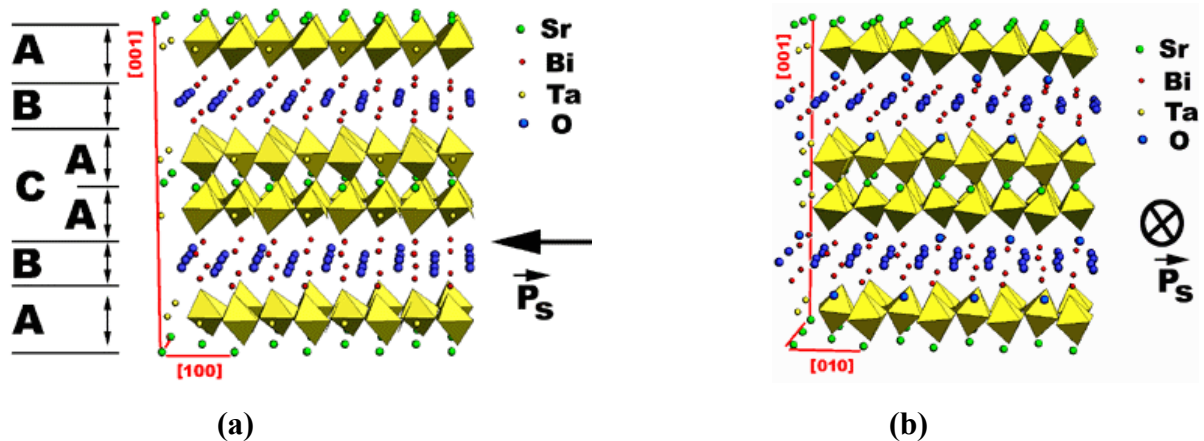


Figure 29 Crystal structure of $\text{SrBi}_2\text{Ta}_2\text{O}_9$: (a) view along the crystallographic b direction, and (b) view along the crystallographic a direction. Crystallographic data from Ref. [137]. “A” denotes the oxygen octahedra layer (TaO_6), “B” the bismuth oxide planes (Bi_2O_2), and “C” shows the entire perovskite layer. The asymmetric distortion of the oxygen octahedra is clearly visible in (a) suggesting a non-zero component of polarization parallel to the $[100]_{\text{orth}}$ -direction.

The orientation of the spontaneous polarization is explained as follows: Each oxygen octahedron is slightly distorted and tilted and possesses an electric dipole. The dipoles in the unit cell are symmetric with respect to the mirror plane (which is parallel to the a - c plane, Figure 29b), and thus the overall dipole momentum of the cell along the b -axis is zero. Along the a -axis (Figure 29a), the tilts of different oxygen octahedra in an “A” layer are the same, so that they generate an effective dipole momentum [139]. In even members, the absence of a

* Except for $\text{Bi}_4\text{Ti}_3\text{O}_{12}$, which actually is of the monoclinic point group m .

dipole component along the c -axis is explained by the presence of a mirror plane parallel to the a - b plane [139,140,141,142]. In contrast, odd members of the BLSF family are expected to possess a component of the spontaneous polarization along the c -direction, since they do not have such a mirror plane. This fact was experimentally proven for $n = 1, 3$ [139] and 5 [143] from macroscopic measurements.

As presented in Sect. 3.4.1 the films investigated were grown by PLD and consist of regions with a c -orientation and regions with a mixed orientation. The mixed-oriented regions have $(110)_{orth}$ - and $(100)_{orth}$ -oriented grains, which, as a rule, can be distinguished by their shape (Figure 12b), embedded into the (001) -oriented film matrix. Since the spontaneous polarization of the even- n -members of the Aurivillius family is along the $[100]_{orth}$ -axis, in SBT and $\text{BaBi}_4\text{Ti}_4\text{O}_{15}$, only the non- c -oriented grains are expected to contribute to the ferroelectric response of the film area under the probing electrode.

Figure 30 compares macroscopic hysteresis loops of an epitaxial SBT film obtained from the different types of regions mentioned above. While the loop acquired in a region having non- c -oriented grains shows a clear hysteresis, the dielectric response of the c -oriented matrix is almost entirely linear. Similar results were obtained for epitaxial films of different materials [144,145], confirming the expectations and demonstrating the need to obtain epitaxial films with non- c -orientation for use in high-quality devices.

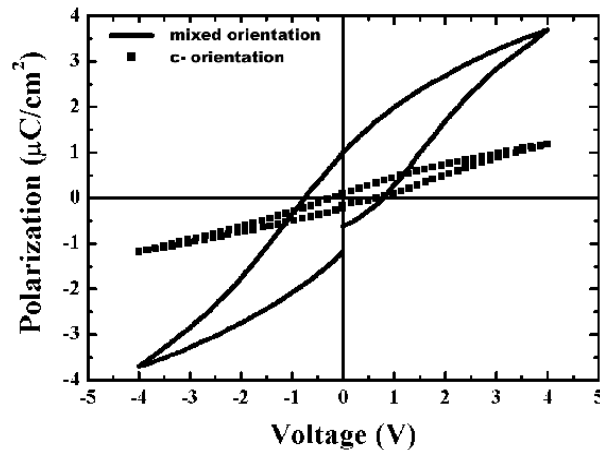


Figure 30 Macroscopic ferroelectric hysteresis loop of an epitaxial SBT film in a region with a large density of (100) - and (110) -oriented grains and in a region mostly c -oriented.

Taking into account the high anisotropy of the crystal structure, it appears to be of great importance to study and to characterize the ferroelectric domains and their switching in thin films of the BLSFs. In this section results will be presented concerning the ferroelectric domain structure observed at the surface of thin films of three members of the BLSFs, having the Aurivillius parameters: $n = 2$ (SBT), $n = 3$ ($\text{Bi}_4\text{Ti}_3\text{O}_{12}$) and $n = 4$ ($\text{BaBi}_4\text{Ti}_4\text{O}_{15}$).

5.3.3 $\text{SrBi}_2\text{Ta}_2\text{O}_9$ films

Studies of strontium bismuth tantalate ($\text{SrBi}_2\text{Ta}_2\text{O}_9$, SBT) films in view of memory applications started less than one decade ago, when the fatigue endurance of this material was discovered [146]. The rapid increase of interest due to the perspectives of this material for

application in FeRAM technology is proven by about 500 publications reporting on the properties of SBT. However, only a few of them (about 2%) represent studies of the ferroelectric domain structure.

In contrast to previous piezoresponse measurements of SBT films ^[57,147,148,149], the samples investigated in this work are of particular importance, because they allow independent probing of the distinct non-*c*-oriented grains and of the *c*-oriented background.

Ferroelectric domains in SBT grains

Figure 31 shows topography and piezoresponse images of an epitaxial SBT film in a region having a mixed orientation. The topographic images (Figure 31a,c) show grains having lateral sizes between 100 nm and 450 nm protruding out of a flat background by 10 nm to 40 nm. The corresponding piezoresponse image (Figure 31b) shows as a first important feature that a strong signal, and therefore piezoelectric activity (black or white contrast in the image), is present *only* at the places corresponding to grains in the topographic image. In contrast, *no signal* can be detected from the *c*-oriented background and in the image it appears gray.

Within the grains, the polarization component perpendicular to the film plane can be either positive (polarization oriented upward, i.e. bottom to top) or negative. However, measurements performed above different places and on several samples have shown that the preferred *initial* polarization state is negative (z-component of polarization oriented top to bottom). Similar conclusions were drawn from piezoresponse measurements performed on similar samples (with another setup configuration) by Gruverman et. al. ^[149].

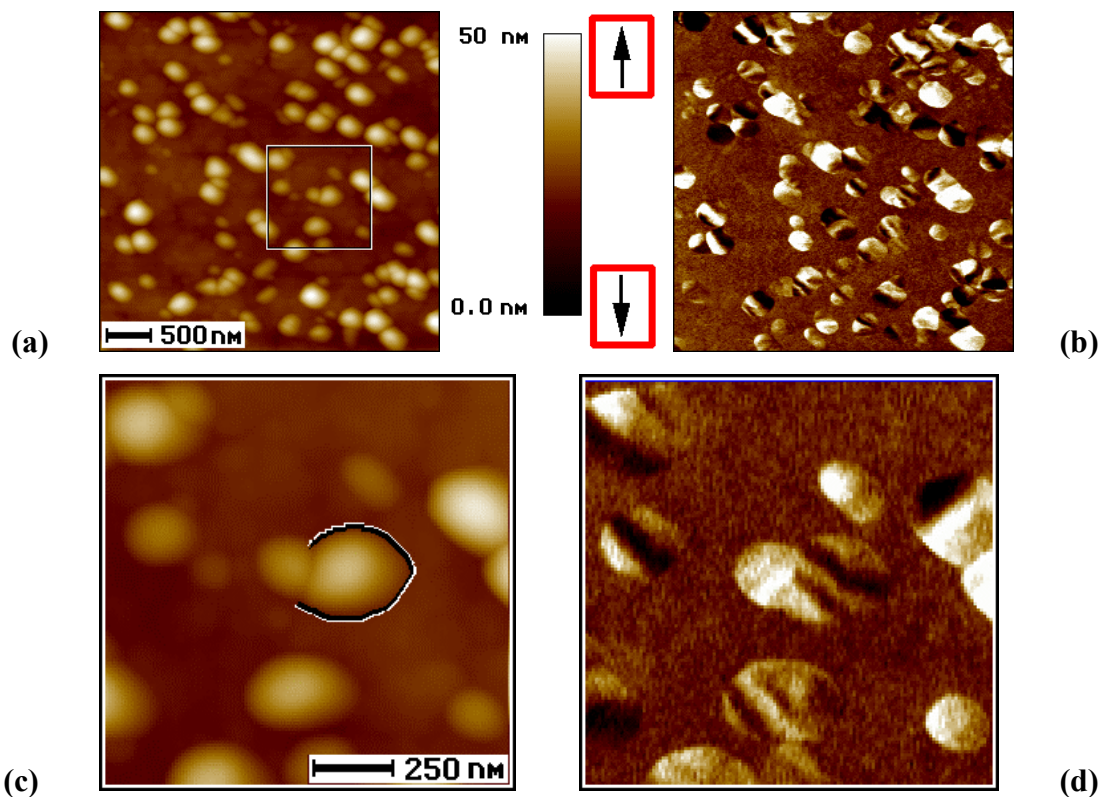


Figure 31 Topography (a, c) and out-of-plane piezoresponse images (b, d) of an SBT film. Images (c) and (d) are higher magnifications of the square outlined in (a). The grain marked in (c) is divided into five ferroelectric domains.

Analyzing the domain structure of the grains it appears that they can be in the monodomain state or can be split into two or more domains (Figure 31d). The central grain outlined in Figure 31c, for instance, is divided into five domains with alternating polarization. The smallest domain resolved up to now in SBT films was 30 nm in lateral size, a value limited by the contact area between tip and sample. An important and somewhat strange feature is that domain walls are (almost) always perpendicular to the longer edge of the grain. According to our careful analysis concerning the epitaxial relationships between grain and substrate^[79], the domain walls appear to be parallel to the c -axis of the crystallite.

As in the case of the PZT films (Sect. 5.2) the piezoelectric contrast was found to vary from one grain to another. In Figure 31d it is indeed evident that grains may have a very strong piezoelectric response (like the two coupled grains in the right part of the image) or they can show a weaker contrast, like the grain marked in (c). A potential explanation is that strong and weak contrasts are determined by different crystallographic orientations of the grains. The (100) -grains should exhibit a higher difference between the positive and negative domains than the (110) -oriented grains. There are two reasons which favor this explanation:

- First, the piezoelectric coefficient is supposed to be at maximum in the direction parallel to the spontaneous polarization (and therefore the contrast of (100) grains should be higher).
- Second, the 180° domain wall between two domains in a (110) -oriented grain is unlikely to be perpendicular to the surface. Therefore, under the probing tip there may be two or more domains each of them having different contributions to the piezoelectric signal. Since for the 180° domain walls these contributions will be out of phase, the piezoelectric response of the (110) -oriented grains is reduced. The 90° domain walls can be perpendicular to the film plane, but they are supposed to be rare in SBT.

However, the difference in the contrast of the grains might come from the inhomogeneity of the films, namely from the different depths of the grains. Cross-section TEM analysis showed that some grains extend down to the bottom electrode, whereas others reach a depth of only 100 nm within the 200 nm thickness of the c -oriented matrix^[79]. As a result, the voltage drop on the c -oriented “dielectric” layer may reduce the actual voltage on the grain and thus the detected piezoresponse.

Moreover, another origin of the different ferroelectric responses could be the size of the grains. Analyzing Figure 31b, it can be seen that grains having larger lateral sizes (more than 300 nm) appear to possess a stronger contrast. Theoreticians have predicted a few decades ago that ferroelectricity should disappear in thin films below a critical thickness that depends on the material and on the processing conditions^[150]. It was also found experimentally that the coercive field increases, and the permittivity drops, with decreasing grain size^[151,152]. These facts were proven to be a consequence of the equilibrium domain structure within the grain^[153]. For lead titanate films it was found that grains smaller than 150 nm in diameter (measurements performed by TEM) are in the single domain state, whereas larger grains exhibit a ferroelectric domain structure. It seems, however, that this is only the case for the simple perovskite structure, for which the tetragonal distortion is not too large. In contrast, the large difference between the lattice constants a and c in the layer-structured thin

films causes not only an anisotropic grain growth, but leads to much thinner stable domain structures.

Switching behavior of SBT grains

Further investigations of ferroelectric properties within individual grains and of the matrix are presented in Figure 32 and Figure 33. First, the neighboring grains shown in Figure 32a were chosen to show a comparison between different responses to electric field biasing. Figure 32b, acquired simultaneously with the topography, illustrates the initial domain structure (z-component of polarization oriented top-to-bottom). Grain No. 2 appears to possess a weaker piezoelectric response (a dark gray contrast) than grain No. 1. The ferroelectric hysteresis of each grain was then probed separately by fixing the SFM tip above the desired place. Switching of the polarization from the negative to the positive state is proven by modifications occurring in the domain structure (Figure 32c) and by the presence of a local piezoelectric hysteresis (Figure 32e).

Of high importance is to determine whether switching of one grain modifies the polarization state of the neighboring grains, a question which is related to the problem of cross talk between different memory cells in a FeRAM. An intermediate piezoresponse image (not shown) acquired between the probing of the two grains proved that indeed biasing the grain No. 1 did not affect the domain structure of grain No. 2.

From local hysteresis measurements it follows that switching behavior differs from grain to grain in terms of the hysteresis parameters: magnitude of the piezoelectric response, coercive field, vertical shift and shape. Figure 32e gives an idea on the differences encountered in ferroelectric characterization of individual grains. From an almost ideal, symmetric and rectangular-shaped hysteresis loop like the one of the grain No. 1, several variations in switching behavior could be measured, to the rather strange loop of grain No. 2. This is, of course, an undesirable feature for the prospective application of epitaxial thin films in FeRAMs, arising from differences in the local environment of each grain, as already pointed out above.

These non-uniformities show up not only in terms of hysteresis loop parameters, but also as formation and evolution of the ferroelectric domain structure on a long time scale. Figure 32d shows the domain structure of the two grains four hours after the positive poling of grain No. 1 (grain No. 2 was poled one hour later). The positive domain in the central part of grain No. 1 (Figure 32c) has switched back, indicating that the induced domain structure was unstable, in contrast to grain No. 2 whose domain structure was still found unchanged after 24 hours.

90° switching in SBT?

Another important actual question regarding the switching properties of SBT is whether or not 90° domain walls exist and are stable in such a material with a high anisotropy. Grain No. 2 seems to present evidence of 90° domain switching in SBT. As was already emphasized, the initial domain contrast of this grain was rather weak and close to gray (Figure 32b). Bias cycling revealed a very strange response during the first loop, with almost no indication of ferroelectricity, as can be seen in Figure 32f. Starting with the second cycle the piezoelectric response increased, and from the third cycle onward the hysteresis loop stabilized. Further cycling showed the same shape and magnitude of the signal. The lattice parameters in SBT

were recently measured with a high accuracy ^[138]. According to this report the orthorhombic distortion between the a - and b - axes in SBT is $(b/a-1) = 0.03\%$, about five times smaller than the tetragonal distortion in barium titanate. This small distortion implies that 90° domain walls are almost free of stress, and therefore the a - and b - axes can easily flip, allowing 90° switching. Also, a look to Figure 29 confirms that only very small ion movements are involved in an a - b flip. In our experiment, grain No. 2 was most probably initially (010) -oriented having therefore the spontaneous polarization in the film plane, and showing only a weak negative contrast, probably due to a built-in electric field generated by the electrode asymmetry. During the first cycling the grain was 90° switched, so that it became (100) -oriented and therefore the ferroelectric polarization became detectable.

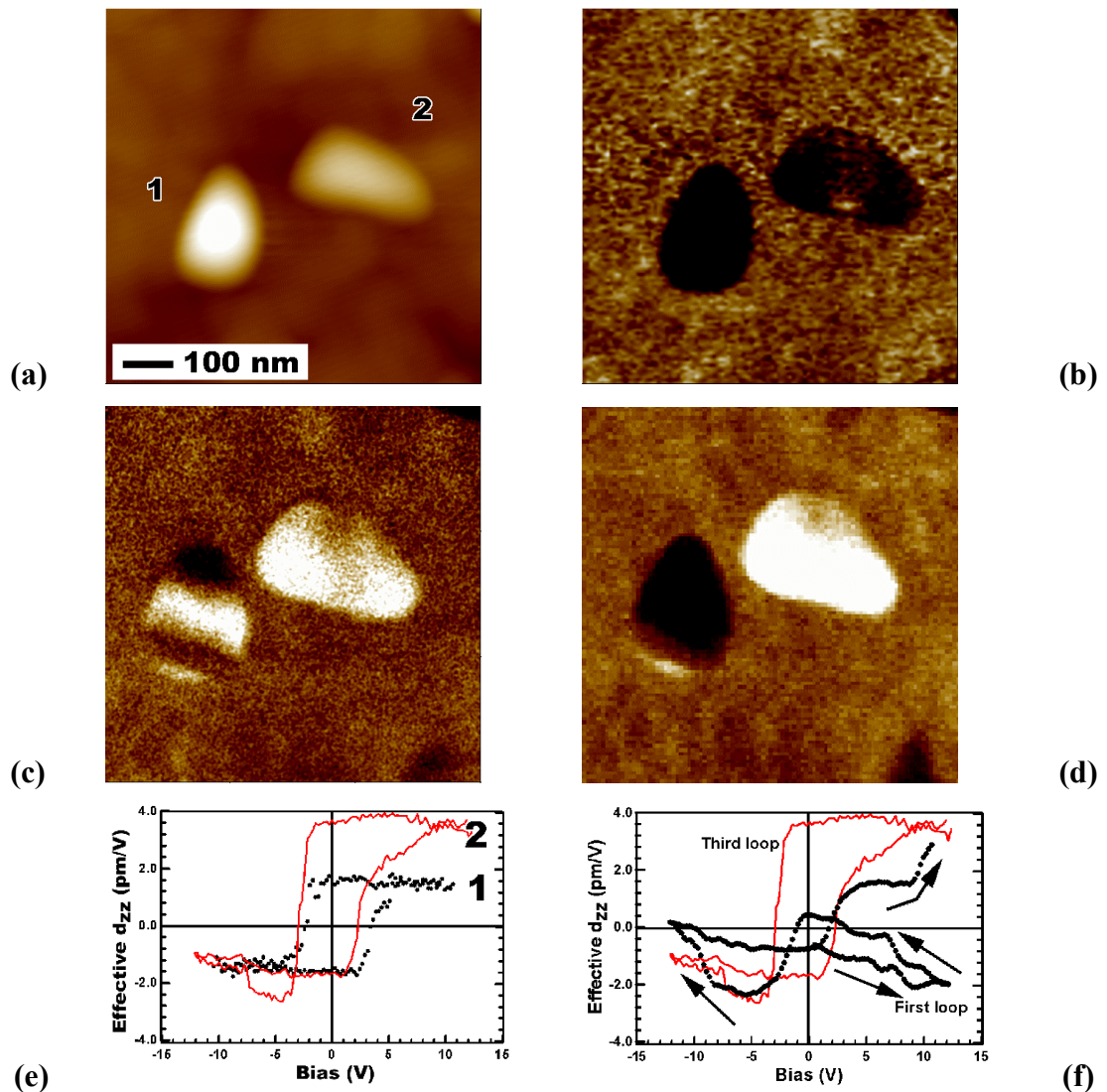


Figure 32 Different switching behavior in SBT grains. **(a)** Topography. **(b)** Piezoresponse image showing the domain structure before hysteresis loop measurements. **(c)** Piezoresponse image after recording a hysteresis loop from each grain, the last voltage applied being +12 V. **(d)** Piezoresponse image recorded 4 hours after poling grain No. 2. **(e)** Piezoelectric hysteresis loops of the two grains. **(f)** First hysteresis loop of grain No. 2 compared with the third. *Note: Grain No. 2 was not influenced by the hysteresis loop measurement of grain No. 1.*

In principle, it is possible to push further the characterization of SBT grains with different orientations. Assuming that grain No. 1 is (110)-oriented and grain No. 2 has (100) orientation, we find the following ratio between the magnitudes of piezoelectric coefficients along these directions:

$$\frac{(d_{zz}^+ - d_{zz}^-)|_{zz=(110)}}{(d_{zz}^+ - d_{zz}^-)|_{zz=(100)}} = 0.57 \quad \text{Eq. 32}$$

An analysis of both detectable components of polarization (out-of-plane and in-plane of the film) will complete the elucidation of switching in SBT. Also, the absence or presence of 90° domain walls in SBT can be studied in a similar manner as in the case of barium titanate (Sect. 5.1.2). However, detection of the in-plane induced oscillations in SBT films seems to be a real challenge and it was not possible up to now to get reliable experimental data. Further experiments are in progress.

Domain wall pinning in SBT crystallites

Sometimes SBT grains in our films exhibit a domain structure like that presented in Figure 33c, a domain pattern that looks very stable. The 150 nm × 90 nm grain appears with a negative polarization (z-component oriented top-to-bottom) except a thin line (about 40 nm in thickness) that crosses the grain width. The question arises whether or not the gray line in the piezoresponse image is switchable or at least can be modified.

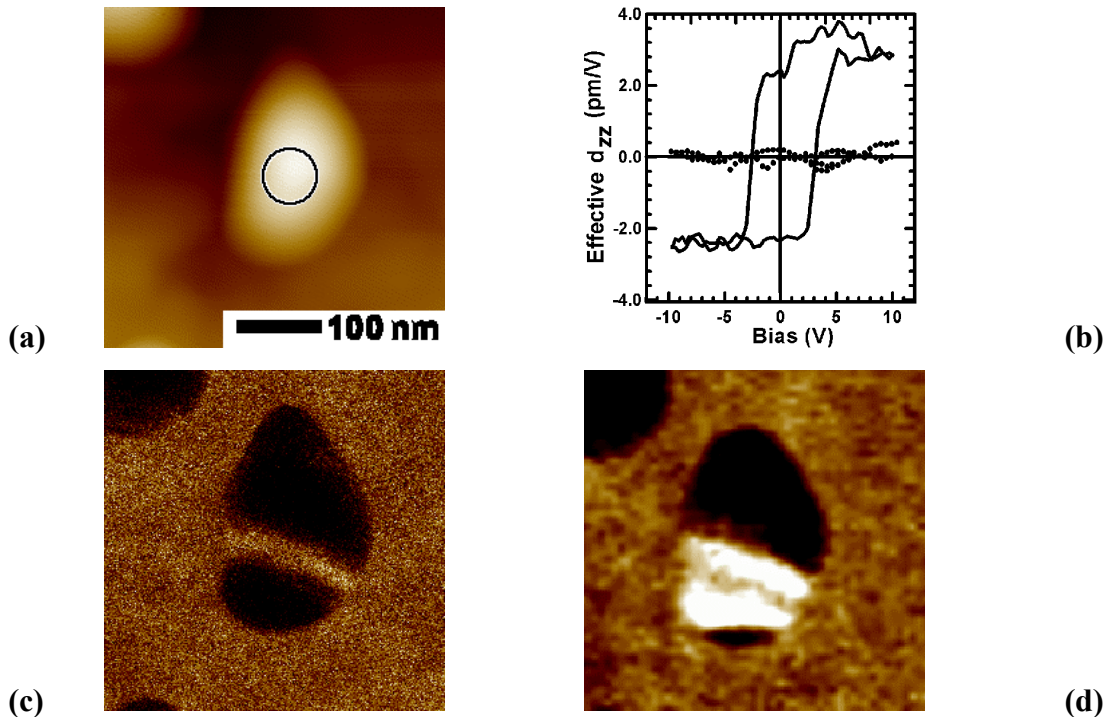


Figure 33 Switching of a ferroelectric domain in a 150 nm lateral size grain of SBT. **(a)** Topographic image of the grain. **(b)** Piezoelectric hysteresis loop of the grain (full line) and of the flat background (dots). **(c)** The domain structure of the grain in the negative polarization state, before switching. **(d)** Domain structure of the grain 2 hours after the application of a 10 V / 100 ms pulse. The circle in (a) shows the estimated contact area during the hysteresis loop measurement.

Since the tip radius is in the range of 30 nm to 50 nm, this feature is at the resolution limit; the circle in the topographic image shows the estimated contact area. For instance, a positive domain 20 nm in width could give the same piezoelectric contrast.

Recording of piezoresponse hysteresis loops of the grain at the place marked by the circle in the topographic image revealed the normal ferroelectric behavior of the non-*c*-oriented grains in this film (Figure 33b). The bias procedure ended with a positive pulse, therefore the grain has been switched into the positive state. However, the single-positive domain state was not stable. Even within the first subsequent scan (less than five minutes after poling) the polarization in the grain started to switch back quite fast, so that at the second image the domain pattern reached the state shown in Figure 33d. The same domain configuration was still found two hours later. A comparison of images (c) and (d) in Figure 33 clearly reveals the immobility of the gray region against the electric bias cycling. Such a stability of the polarization can be due to a pinned or clamped region, probably deep inside the grain, at the interface with the *c*-oriented matrix. This may explain both the gray contrast and the lack of interaction with a strong bias field. However, it is difficult to understand why this “inactive” region does not affect the shape of the hysteresis loop and also the stability of either positive or negative orientation of the polarization in the proximity of this pinned region.

Anisotropy at the nanoscale

The absence of a polarization component along the crystallographic *c*-axis was already proven in all piezoresponse images by the presence of a gray contrast at the flat *c*-oriented background. However, it is still required to check whether or not a piezoelectric response can be induced there by an electric bias. This task was accomplished, and the result is presented in Figure 33b (dotted curve), in comparison with the response of the non-*c*-oriented grain. It is obvious that no remanent polarization could be induced in the matrix by an electric field, in complete agreement with the properties deduced from macroscopic data.

Typical values of the piezoelectric coefficient (*effective* d_{zz} at zero bias field^{*}) measured in non-*c*-oriented SBT grains are between 2 pm/V and 5 pm/V. These values represent about half of the reported d_{33} ^{**} coefficient in thin films using double interferometry^[94]. As in the case of PZT films, the thin film values are several times lower (at least two times) than the coefficients measured in bulk materials. Indeed, very recently, the successful preparation of SBT single crystals with $P_S = 16\mu\text{C}/\text{cm}^2$ and $d_{11} = 22\text{ pm}/\text{V}$ was reported^[154].

5.3.4 *BaBi₄Ti₄O₁₅ films*

Barium bismuth titanate (BaBi₄Ti₄O₁₅) is an even-*n* member of the Aurivillius family, having four oxygen octahedra sandwiched between two bismuth oxide planes. The study of this material was performed to prove the existence of a ferroelectric behavior at a mesoscopic scale, and to observe the effects of the anisotropy. Visualization of the domain structure in this material was achieved for the first time^[58]. Measurements have confirmed that the ferroelectric behavior has the same trend as in case of SBT.

^{*} Equivalent to d_{11} in a single crystal if the respective grain was *a*-oriented (see Appendix B)

^{**} The notation d_{33} in thin films stands for the effective longitudinal piezoelectric coefficient.

Domain structure and switching

The ferroelectric behavior was tested on different grains having (100) - or (110) - orientations. No significant difference was found between the two types of grains. A typical example of ferroelectric switching performed on a (110) - oriented rectangularly shaped grain is shown in Figure 34.

By probing the negative domain of the rectangular grain (point marked by a cross in Figure 34a) a piezoelectric hysteresis loop was recorded (Figure 34d). Note that at the starting point of the curve the piezoelectric coefficient is negative, which is consistent with the initial domain state seen in Figure 34b. The values obtained for the piezoelectric coefficient at saturation $+d_{33}^{rem} = 10 \text{ pm/V}$ and $|-d_{33}^{rem}| = 18 \text{ pm/V}$ are comparable with the value of $d_{33} = 12 \text{ pm/V}$ measured for poled ceramic disks of $\text{BaBi}_4\text{Ti}_4\text{O}_{15}$ by Subbarao^[133].

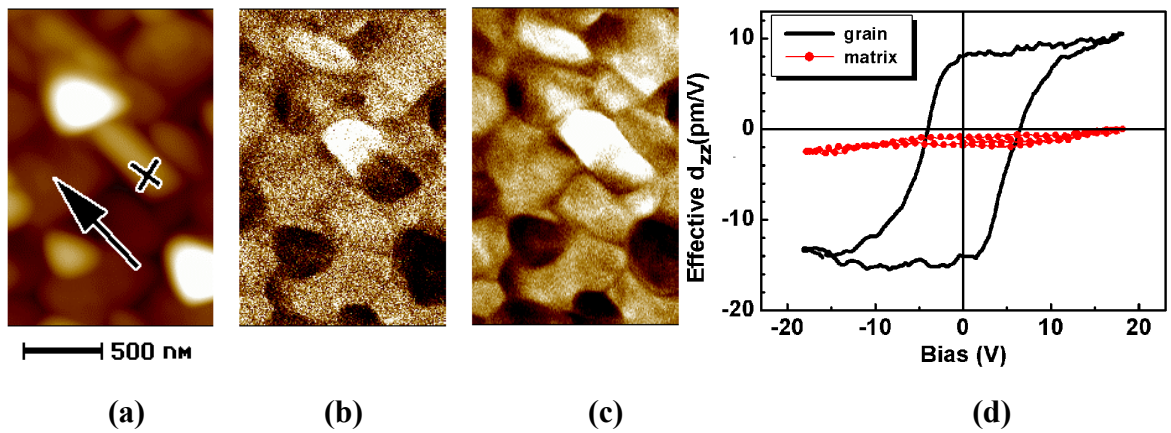


Figure 34 (a,b,c) Topography (a) and piezoelectric response images of a (110) -oriented crystallite of $\text{BaBi}_4\text{Ti}_4\text{O}_{15}$ before (b) and after (c) acquirement of a piezoelectric hysteresis loop. **(d)** Piezoelectric hysteresis loops acquired at the place marked by a cross in the topographic image (—) and in the c -oriented region (—●—) at the place marked with an arrow in the topographic image. The c -oriented region exhibits no piezoelectric activity.

The coercive voltages of $+V_c = 5.8 \text{ V}$ and $|-V_c| = 4.5 \text{ V}$ of the nanoscopic hysteresis loop are comparable with $V_c = 4.48 \text{ V}$ obtained from classical macroscopic ferroelectric hysteresis measurements performed on the same sample^[145]. The imprint in the LaNiO_3 - $\text{BaBi}_4\text{Ti}_4\text{O}_{15}$ structure is confirmed by the shifts of the hysteresis loop in the negative direction along the d_{zz} -axis and in the positive direction of the electric field axis, which means that switching of polarization in the positive direction requires a higher field.

Figure 34c presents the piezoresponse image of the same area after having performed the piezoelectric hysteresis loop measurement. As the last voltage applied was $+20 \text{ V}$, the polarization and the piezoelectric constant remained positive after the acquirement of the hysteresis loop and it can easily be seen that the entire grain became positive. Therefore, in this case, a single ferroelectric domain as small as 300 nm in size was switched within a (110) -oriented crystallite of $\text{BaBi}_4\text{Ti}_4\text{O}_{15}$ ^[58].

Anisotropy

As in the case of SBT, due to the symmetry it is expected that the spontaneous polarization has no component along the c -direction. Measurements performed by Kim et al. on $\text{BaBi}_4\text{Ti}_4\text{O}_{15}$

single crystals revealed a strong anisotropy of the dielectric constant ^[155]. They found that $\epsilon_{a,b} / \epsilon_c = 6$ at room temperature and $\epsilon_{a,b} / \epsilon_c = 58$ at the Curie temperature, concluding that the Bi_2O_2 planes act as paraelectric layers in $\text{BaBi}_4\text{Ti}_4\text{O}_{15}$. However, to date there are very few experimental indications of the absence of the spontaneous polarization in the c -direction ^[139]. In order to investigate the ferroelectric behavior along the c -axis, the piezoresponse of a point located on the c -oriented region was thus measured. The hysteresis loop measurement shown in Figure 34d (dots) was performed at the place marked by the arrow in Figure 34a. The absence of the piezoelectric hysteresis definitely demonstrates that the polarization vector in $\text{BaBi}_4\text{Ti}_4\text{O}_{15}$ has no component along the c -axis.

5.3.5 $\text{Bi}_4\text{Ti}_3\text{O}_{12}$ films

Bismuth titanate ($\text{Bi}_4\text{Ti}_3\text{O}_{12}$) is an odd- n member of the Aurivillius family, having three oxygen octahedra between two bismuth oxide layers. Its crystal symmetry in the paraelectric phase is tetragonal, and it appears that $\text{Bi}_4\text{Ti}_3\text{O}_{12}$ is one of the few compounds within the Aurivillius family that has a monoclinic ferroelectric structure, with one component of the polarization in the plane of the layers, and the other perpendicular to this plane. The resulting domain-wall structure is complex, leading to complicated but also interesting optical, electric, and piezoelectric properties.

Right from its discovery ^[131] it was considered as the representative prototype member of the BLSFs, also known as the “bismuth titanate family” ^[136]. The discovery of ferroelectricity and optical activity in $\text{Bi}_4\text{Ti}_3\text{O}_{12}$ single crystals started a vast new area of research ^[133,156].

In this work, the most exciting results were obtained on bismuth titanate, too.

Ferroelectric domains

Our epitaxial $\text{Bi}_4\text{Ti}_3\text{O}_{12}$ films grown by PLD show mainly the same structural and crystallographic characteristics as the SBT and $\text{BaBi}_4\text{Ti}_4\text{O}_{15}$ films presented previously. The only differences were their larger thickness of 500 nm (double than SBT) and the longer rectangular crystallites, of the order of 1 – 2 μm . TEM investigations revealed that these crystallites had a (110) - orientation with the c -axis perpendicular to the long edges of the crystallites ^[79,157].

Figure 35 shows the typical surface morphology and the corresponding domain structure of a $\text{Bi}_4\text{Ti}_3\text{O}_{12}$ film grown on $\text{LaNiO}_3 / \text{STO}(001)$. The topographic image reveals several rectangular grains with a large aspect ratio (approx. 5:1), having the long edges oriented along two mutually perpendicular directions, viz. parallel to $[100]$ and $[010]$ of the STO substrate ^[79]. The out-of-plane domain image reveals a very strong contrast within the grains (black, white and gray stripes alternating along the grain length) and almost no contrast in the surrounding film matrix (gray). The domain size ranges from 100 nm up to the entire crystallite size. The domain walls appear perpendicular to the grain length and therefore parallel to the c -axis at least in the initial state. The gray contrast within the grains can be explained by the presence of opposite domains over the film thickness, therefore contributing out of phase to the local piezoresponse.

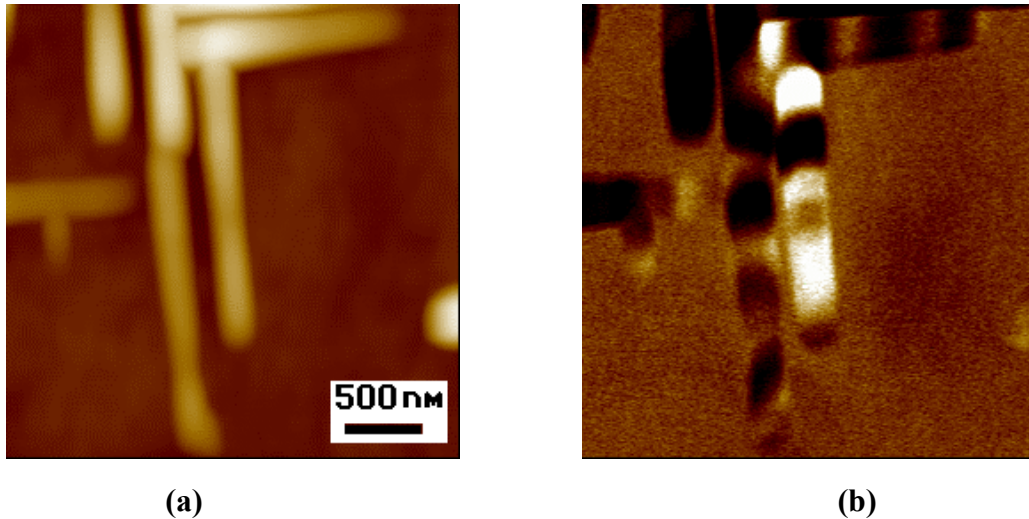


Figure 35 (a,b) Topography (a) and out-of-plane domains (b) in an epitaxial $\text{Bi}_4\text{Ti}_3\text{O}_{12}$ film.

It was found that the initial domain structure contains positive domains (polarization oriented bottom to top) especially in regions where the density of the (110) -oriented crystallites is rather high (with connected and overlapped grains like the ones in Figure 35). This suggests that the local ferroelectric behavior is strongly dependent on the orientation, polarization and strain induced by the environment. In order to avoid the uncontrollable influence of the neighboring grains and to ensure the same background for the initial state, the following experiments were performed on isolated grains, in regions where their density was low.

Local piezoelectric response

When probed for the local piezoelectric hysteresis it appears that, unlike all the other samples tested, $\text{Bi}_4\text{Ti}_3\text{O}_{12}$ films behave in a unique way. Looking to the in-field hysteresis loop obtained from one of the non- c -oriented grains (dotted loop in Figure 36) the loop appears to be comparable with those obtained from PZT films having about the same thickness. However, a very strange behavior was observed in $\text{Bi}_4\text{Ti}_3\text{O}_{12}$. If the biasing voltage is suppressed at the maximum field applied (e.g. 30 V, positive or negative) the piezoresponse signal drops to a very low value and even changes its sign, as indicated by arrows in Figure 36! Recording the remanent loop above the same place revealed that for those high pulses, the piezoelectric coefficient decreases and often changes its sign as if the polarization under the tip would switch back after the removal of the field.

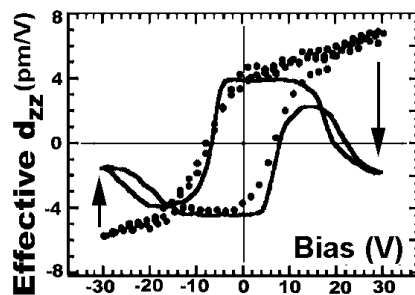


Figure 36 In-field (dots) and remanent (full line) piezoelectric hysteresis loops of non- c -oriented grains of bismuth titanate.

To obtain more information about this switching behavior, it would be helpful to record a domain image after each pulse applied to the same point of the sample. This task, however, requires a very good stability of the system (a high-resolution image may require up to approx. 1.5 hours) and may be difficult to achieve, due to the tip deterioration during the scanning process. Figure 37 summarizes an experiment in which the domain structure was recorded for the most important regions of the remanent hysteresis loop, namely at $V_{\text{bias}} = \pm V_{\text{max}}$ and at $V_{\text{bias}} = 0$. It is worth to specify that a very similar behavior was observed overall not only on epitaxial films, but also on polycrystalline films, deposited on $\text{LaNiO}_3 / \text{YSZ} / \text{Si}(100)$ [73].

The initial polarization state was negative (Figure 37c), in accordance with the already mentioned observation that this is the general case for isolated grains in our films. On the hysteresis loop, this domain image corresponds to the point marked “c”, with $d_{zz}^-(0) = -4.5 \text{ pm/V}$. The SFM tip was positioned over the grain shown in Figure 37a at the place marked by the cross, and voltage pulses were applied to the tip as described for the measurement of remanent hysteresis loops.

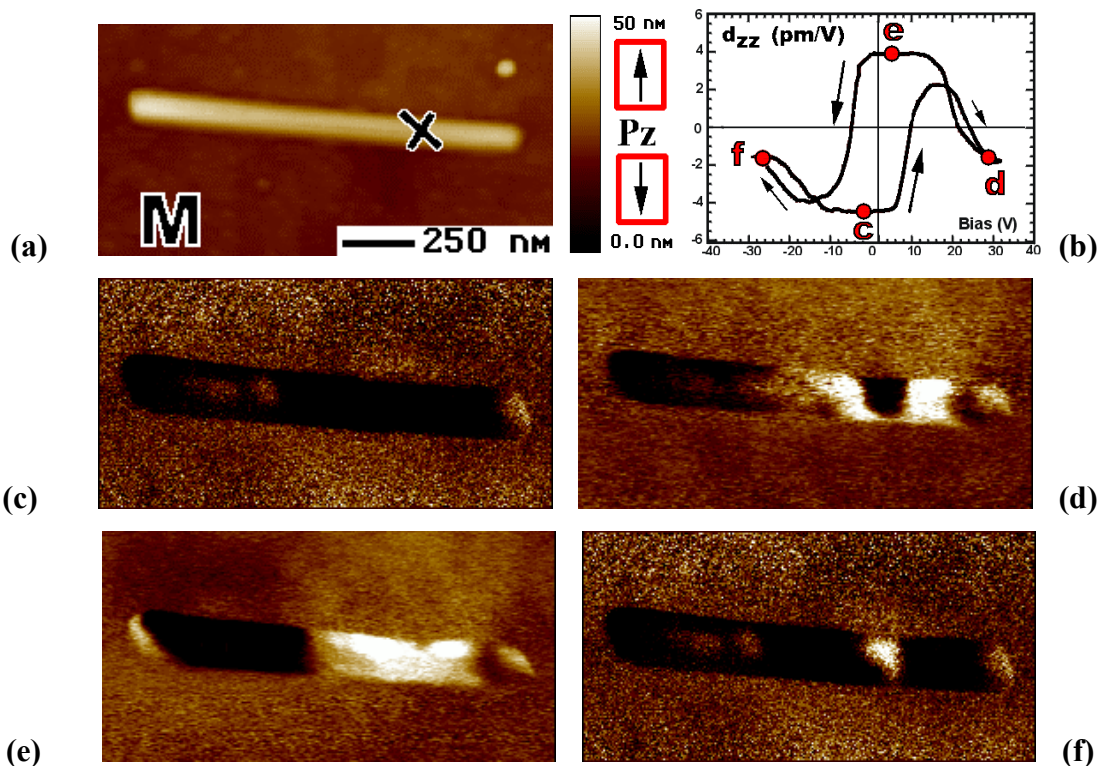


Figure 37 Out-of-plane piezoresponse characterization of a (110) -oriented grain of bismuth titanate. (a) Topography, the cross indicates the place where the SFM tip was fixed for hysteresis measurement. (b) Remanent piezoelectric hysteresis loop of the grain. (c–f) Piezoresponse images acquired to visualize the domain structure corresponding to the places marked with bullets on the loop.

Applying increasing voltage pulses to the marked region it is found that the piezoresponse sharply increases near the coercive field, becomes positive, but the expected saturation is not reached anymore. Surprisingly, the piezoelectric coefficient starts to *decrease*

and even becomes negative, as if the polarization would be oriented in the opposite direction than that imposed by the electric field applied (section “c” – “d” marked on the loop). The biasing procedure was interrupted at point “d” in order to record the corresponding domain structure induced in the grain, and the corresponding image is shown in Figure 37d. Remarkably, the domain image is indeed consistent with the hysteresis data. With other words, the place where the tip has applied the voltage exhibits a dark contrast over several tens of nanometers, indicating an orientation of polarization in another direction than that initially expected. Furthermore, the image shows that outside this area positive domains were switched in the grain, on both sides of the probing point, up to a distance of about 150 nm from the probing point. The hysteresis loop cycling was continued subsequently by applying bias pulses with amplitudes decreasing from the previous V_{max} (in this case 30 V) down to zero (point marked “e” on the loop). Again unexpectedly, the piezoelectric response *increased* up to $d_{zz}^+(0) = +4 \text{ pm/V}$. The domain image corresponding to this stage (Figure 37e) fully confirms the switching of the region under the tip *at decreasing bias pulses*, showing that almost half of the grain has the polarization upward.

The same measurement procedure was then applied for negative voltages, starting from this state. Decreasing the pulse amplitudes down to $-V_{max}$ (the point indicated with “f” on the loop) resulted, as revealed by Figure 37f, in complete switching around the probing place, but *not under the tip*. Finally, increasing the bias pulses from $-V_{max}$ up to zero, the grain arrived in the same state as before cycling (Figure 37c), indicating that the process is reversible.

Franke et al. reported somewhat similar effects on PZT(53/47) thin films^[158]. They explained this behavior as being caused by the Maxwell stress (electrostatic attraction between tip and bottom electrode) developed during the application of high voltage pulses (up to 30 V, their film having 600 nm thickness). In their case, the depolarization was supposed to occur *via* ferroelastic switching, which takes place to minimize the elastic energy of the crystallite. In the case of PZT, this means in fact a 90° switching, which results in the spontaneous polarization oriented perpendicular to the direction of the compressive stress. However, their setup did unfortunately not allow ferroelastic switching without the application of an electric field, thus preventing them from a definitive confirmation of their explanation.

In our case, however, there is not only a depolarization, i.e. a decrease of the piezoelectric signal to zero, but definitely the appearance of a non-zero value: in Figure 37b the piezoelectric coefficient reaches -2 pm/V at high positive voltages. Furthermore, in our experiments we did not detect any change in the piezoresponse even for 1 GPa stress applied to the sample, a value about 30 times higher than the estimated Maxwell stress. Therefore, we think that the reason for the observed behavior is electrostatic (and not mechanic) in nature. As shown in Sect. 3.2.4 and Appendix A the electric field generated by the SFM tip in the sample is extremely nonhomogeneous due to the tip shape and to the high dielectric permittivity of ferroelectric materials. According to the simulations (Figure 9 in Sect. 3.2.4), there is a large area in the contact region where the electric field applied is nearly parallel to the surface, having a radial symmetry. At strong electric fields the polarization may be oriented by this electric field resulting in a metastable domain pattern with domain walls directly under the contact place. The presence of domain walls may lead to unusual piezoelectric response in their vicinity, and, of course, the relationship between polarization and piezoelectric coefficient (Eq. 10, Sect. 2.2) is not valid anymore.

This explanation is consistent with measurements of the in-plane piezoresponse signal. If the polarization is oriented in the film plane by the high electric fields, its orientation should also depend on the polarity of the poling. It follows that an *opposite contrast* should result in the in-plane piezoresponse images for positive and negative poling. Taking into account the local field distribution under the tip (suggested by the equipotentials in Figure 9, Sect. 3.2.4), the reversal of the in-plane contrast in the vicinity of the poling location is expected as indicated in Figure 38.

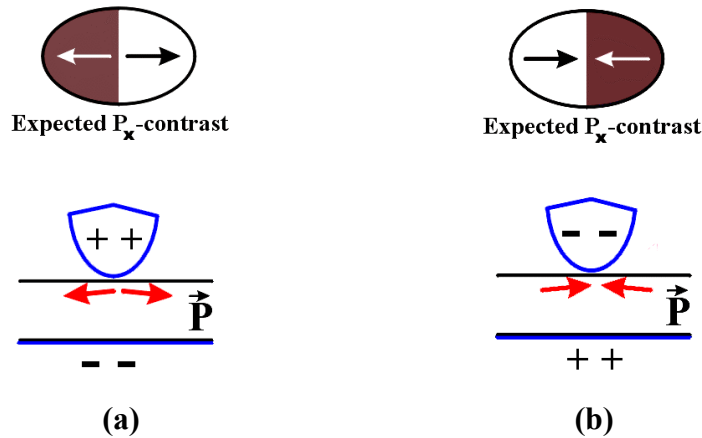


Figure 38 Expected contrast of the in-plane piezoresponse image (upper images) for high voltages applied in remanent hysteresis loops. **(a)** for negative and **(b)** for positive voltages applied to the bottom electrode. The lower images are side views.

Indeed, experiments have confirmed these expectations. Figure 39 summarizes an experiment during which the in-plane piezoresponse signal was monitored in addition to the out-of-plane piezoresponse. The cross in Figure 39a indicates the place above a grain where the local measurements were performed. For high positive voltage pulses, the contrast of the in-plane piezoresponse image (Figure 39d) is similar to the contrast predicted in Figure 38b. As expected in Figure 38a, for high negative voltages applied to the tip, the in-plane contrast of Figure 39c is reversed. Therefore, the images (c) and (d) in Figure 39 obviously demonstrate the in-plane switching in the probing region*.

The in-plane “hysteresis” loop (Figure 39b, full line) represents the in-plane signal recorded as a function of the bias pulse amplitude. The shape of the curve clearly indicates that in the contact region, for bias voltages higher than 20V in absolute value (where $|d_{zz}|$ decreases), a formation of in-plane domains takes place. In contrast, for voltages between +20V and -20V, the in-plane signal is not well defined, suggesting domain wall movements and domain rearrangements. As it is obvious, changes in polarization direction with the voltage cause fast variations of the in-plane signal, which take place for pulse amplitudes corresponding approximately to the coercive voltage on the out-of-plane loop (d_{zz}).

* It should be reminded that, due to the particularities of the detection method, the in-plane piezoresponse images illustrate only the component of the vibration *perpendicular* to the cantilever axis as indicated on the color bars, and not the entire in-plane component of the polarization.

Now the question arises why such an effect occurs *only* in bismuth titanate and not in the other BLSF materials. To give an answer is not simple, and would require a laborious computation of the total energy minimization in the system under consideration.

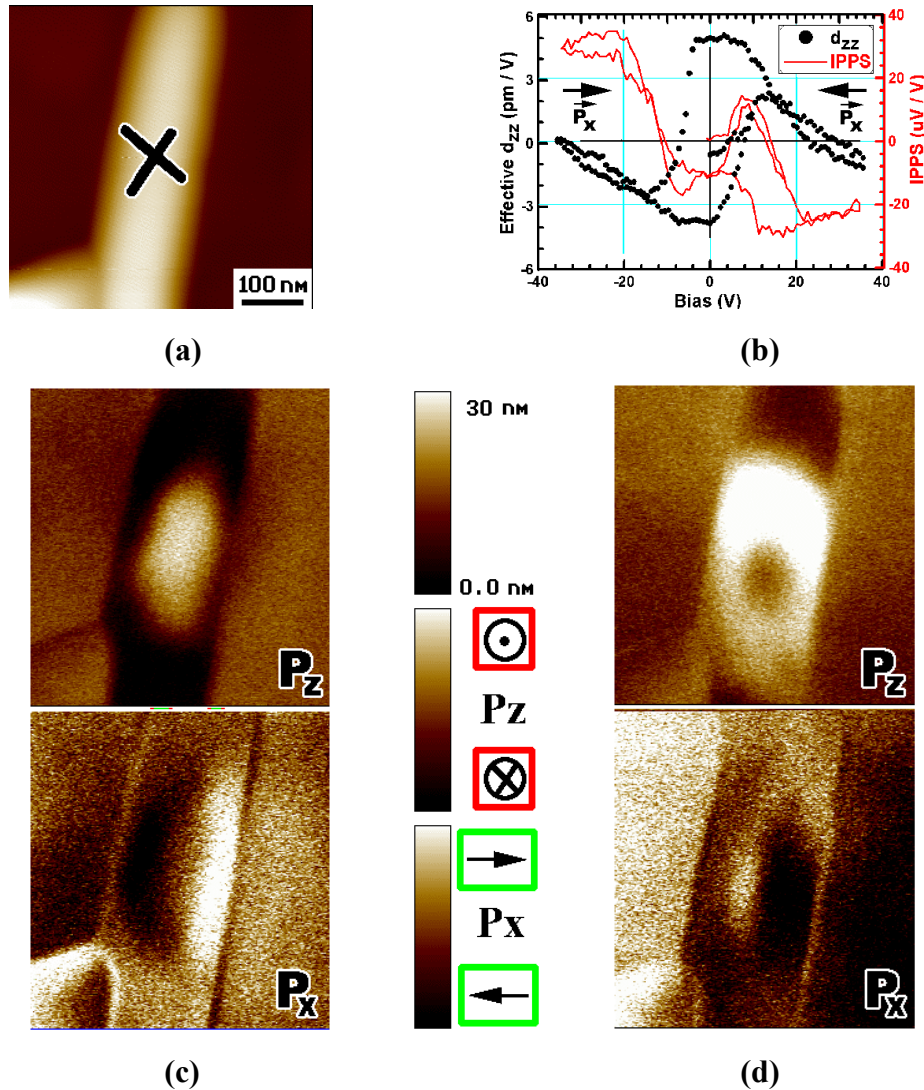


Figure 39 High-magnification two-dimensional monitoring of piezoelectric switching in a (110) -oriented grain of bismuth titanate. **(a)** Topography showing the probing place. **(b)** Out-of-plane (dots) and in-plane (solid line) piezoelectric loops of the grain (IPPS stands for *in-plane piezoresponse signal*). **(c)** Out-of-plane (up) and in-plane (down) piezoresponse images illustrating the domain configuration after a strong negative pulse. **(d)** *Ibid.*, after a strong positive pulse. Note: pulses are applied to bottom electrode.

Simply speaking, the spontaneous polarization in $\text{Bi}_4\text{Ti}_3\text{O}_{12}$ has eight possible orientations (compared to six in tetragonal PZT and four in SBT and $\text{BaBi}_4\text{Ti}_4\text{O}_{15}$) and it is therefore much easier for the polarization vector to find the closest direction to that of the local field. Similar results of Franke et al. ^[158], which were briefly presented above, have been obtained on PZT films with compositions at the morphotropic phase boundary, which is have presumably *fourteen(!)* equivalent domain states (or possible orientations of spontaneous polarization ^{*}) ^[8].

^{*} Viz. the six orientations of tetragonal PbTiO_3 and the eight orientations of rhombohedral PbZrO_3 , assuming that the grains are single crystalline and that there is a uniform distribution of Ti and Zr ions.

Although a large number of allowed directions for the spontaneous polarization leads to an enhancement of the material properties, it also causes some drawbacks such as strains developed in domain walls, fatigue, as well as dielectric and mechanical losses. In the next section an in-situ observation of domain pinning will be shown as an effect of a complex domain configuration.

In-situ observation of local pinning of ferroelectric domains

The study of the basic mechanisms that lead to the inhibition of ferroelectric switching is of very high importance. Usually, the clamping of domains occurs when a charged defect and a domain wall (charged or not) form a stable configuration that prevents the polarization in a certain region to reverse its orientation. The application of high voltage pulses with a sharp tip induces an unusual domain structure due to the extreme inhomogeneous electric field at the tip apex. In combination with an existing domain structure this may lead to the formation of a highly stable configuration that cannot be modified anymore.

Figure 40 illustrates the occurrence of domain pinning in such a situation. The grain shown in the topographic image was probed for the piezoelectric hysteresis at the place marked by the cross. The hysteresis loops acquired show a history dependence (the loops have different shapes) indicating that cycling produces irreversible domain rearrangements.

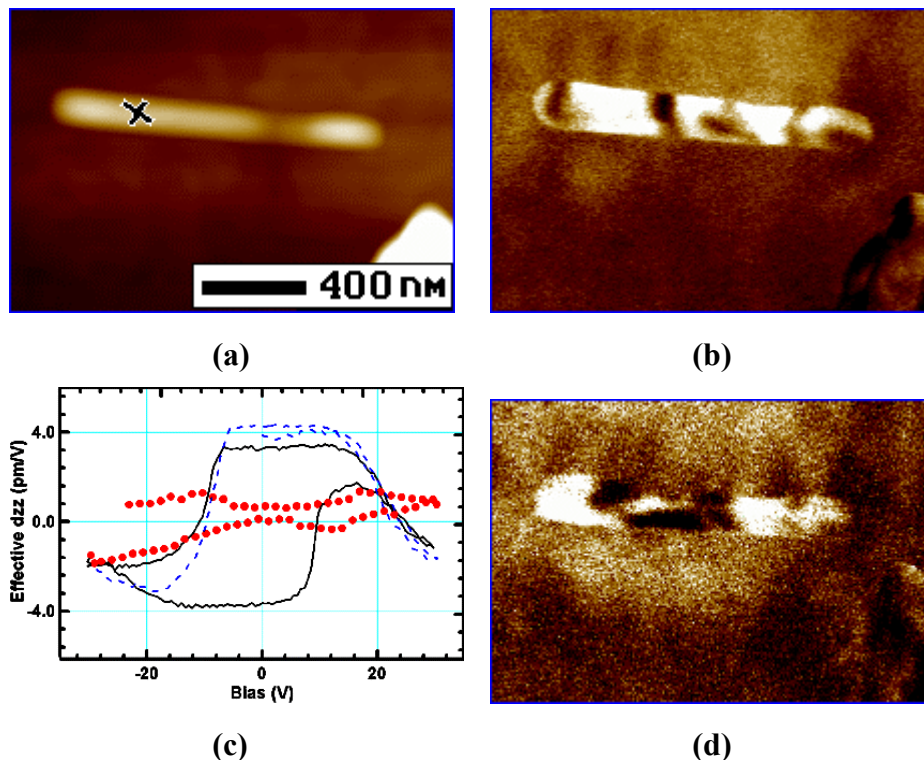


Figure 40 Pinning of domains in bismuth titanate. (a) Topography. (b) Domain image before cycling. (c) Hysteresis loops acquired at the point marked in (a) with a cross. (d) Piezoresponse image after the hysteresis loop measurement showing clamped domains. Note the change in contrast of the matrix around the grain.

The main modification consists in an increase (in absolute value) of the negative coercive voltage of the second cycle (traced with a solid line in Figure 40c) compared to the coercive voltage of the first trace (dashed line). This is an indication that under the probing

location the domain walls became clamped, preventing the growth of negative domains, so that a higher field was required to partly switch again into the negative state. After the maximum negative voltage was applied, the ferroelectric behavior was entirely suppressed, and any expected correlation between the piezoresponse and the voltage applied disappeared (the third loop, represented by dots). The piezoresponse image acquired after the local probing (Figure 40d) reveals the formation of a needle-shaped positive domain inclined with respect to the grain axis. This is certainly not a natural domain wall that can appear in a needle-shaped grain with the c -axis parallel to the film plane and perpendicular to the long edges of the grain. It is reasonable to assume that this special domain is the reason for the occurrence of domain pinning under a high inhomogeneous electric field.

Furthermore, the change of contrast in the c -oriented matrix is remarkable. As it is well known, $\text{Bi}_4\text{Ti}_3\text{O}_{12}$ has a component of the spontaneous polarization along the c -axis and therefore a piezoelectric coefficient $d_{33} \neq 0$. The observed changes in the weak contrast of the matrix indicate switching of the polarization along the c -axis. The next section presents measurements in this region, and compares the obtained piezoelectric data with data from the literature.

Anisotropy in bismuth titanate

Piezoresponse imaging of c -oriented $\text{Bi}_4\text{Ti}_3\text{O}_{12}$ films is rather difficult due to its low piezoelectric coefficient along this direction, and requires long integration times for a reasonable good detection. Local measurements can be performed much easier since they are not limited in duration by the timing imposed by the scanning. We succeeded, however, both to modify and to image the out-of-plane and in plane components of the induced polarization in c -oriented $\text{Bi}_4\text{Ti}_3\text{O}_{12}$ films.

Figure 41a shows the topographic image of a tested area with a cross marking the place chosen for local measurements. Initially, the area did not show a clear piezoelectric contrast for both out-of- and in-plane signals, possibly due to the presence of several domains over the film thickness. A piezoelectric loop was recorded with the tip fixed above the surface. The long time constant needed implied the use of a very low cycling frequency (30 minutes period).

The longitudinal piezoelectric coefficient was found to be $2d_{33} = 1.6 \text{ pm/V}$. Compared to the longitudinal piezoelectric coefficient of non- c -oriented $\text{Bi}_4\text{Ti}_3\text{O}_{12}$ grains we find a ratio $d_{11}/d_{33} = 5 \pm 1$ in complete agreement with measurements by Neto and Cross on single crystals, who found the same ratio^[159].

The domains induced in the sample by a negative pulse are presented in images (c) and (d) of Figure 41. The out-of-plane piezoresponse image shows a weak dark contrast with dimensions of $600 \text{ nm} \times 400 \text{ nm}$ at the place where the field was applied, and a weak light contrast that extends much further into an area larger than $2 \mu\text{m} \times 2 \mu\text{m}$. The in-plane image shows the P_x -contrast expected for the negative poling (see Figure 38a), as discussed in the previous section. The induced domains extend into a hexagonal-shaped area of about 800 nm in lateral size. This area is zoomed in Figure 42a. Additionally, the change in contrast at the domain boundaries is emphasized with line drawings. The dashed line represents the contour of the negative domain observed in the out-of-plane image (Figure 41c).

The domain structure induced can now be easily derived, as shown in Figure 42b, since the crystallographic orientation of the film is precisely known from HRTEM analysis^[79]. The

distribution of the in-plane polarization shows a radial symmetry, in agreement with the calculated field distribution in the vicinity of the sample surface. However, a rectangular area about $100 \text{ nm} \times 200 \text{ nm}$ in size, exactly at the contact location during poling, could not be resolved, since it appears gray in both images. It is reasonable to believe that the region is highly stressed by the surrounding domains (and also by the tip during poling), since all four edges of the rectangle are normal to the spontaneous polarization of the neighboring domain. The presence of a high stress may either clamp the piezoelectric response, or even cause a reduction of the spontaneous polarization. Furthermore, the domain structure in Figure 42b is certainly not a natural domain configuration, in the sense that it implies a positive charge distribution, in the respective area, that should have been induced by the tip*.

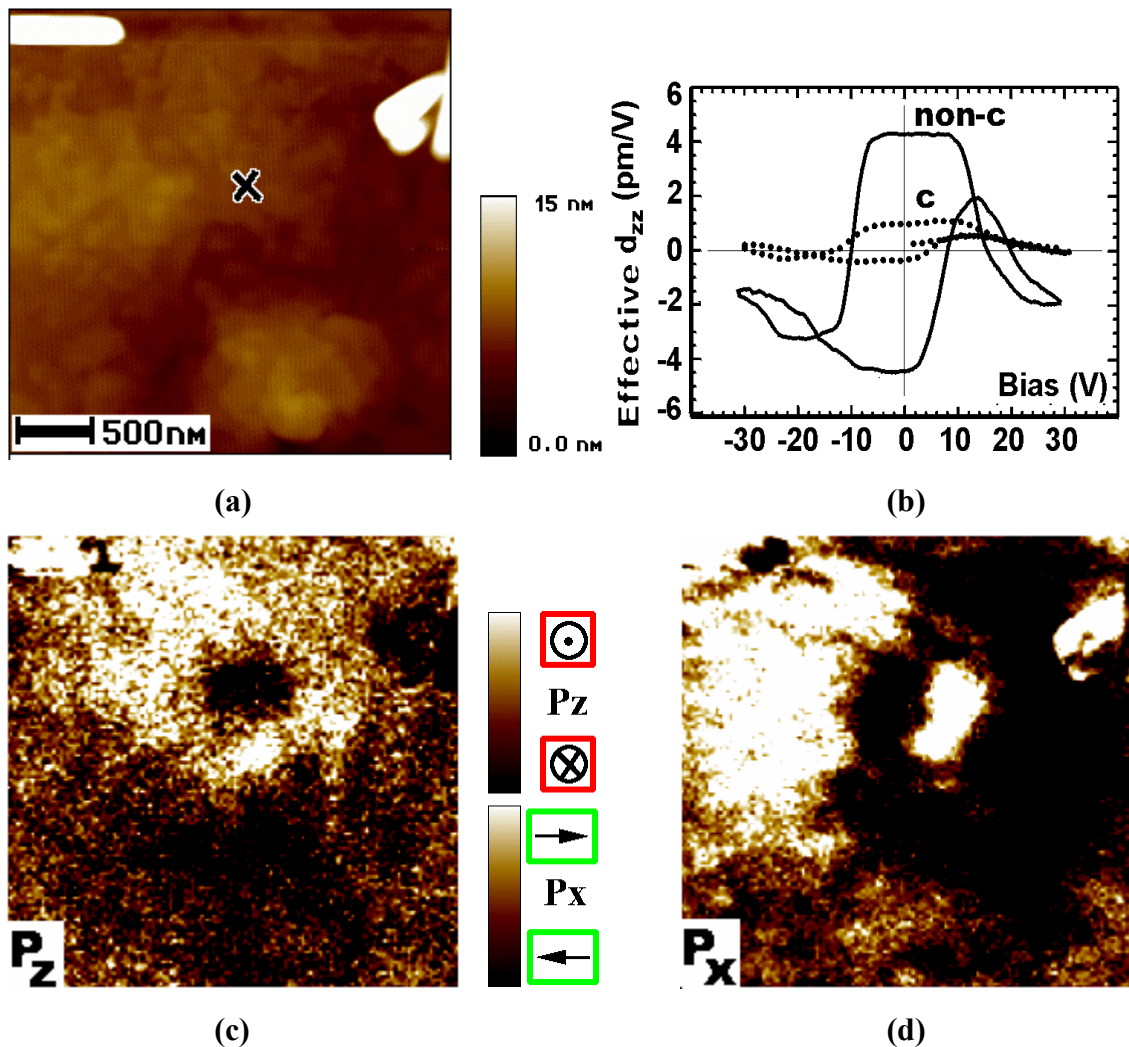


Figure 41 Study of the ferroelectric behavior in c -oriented bismuth titanate films. (a) Topography of the area; the probing place is indicated by a cross. (b) Comparison between the response of non- c -oriented grains and the matrix. (c,d) Out-of-plane (c) and in-plane (d) piezoresponse images of the area after the application of a strong negative voltage pulse to the bottom electrode. Note: The initial contrast was gray, i.e. featureless.

* As already mentioned, the negative voltage was applied to the bottom electrode.

Another characteristic of the domain structure inferred from our measurements is that the 90° -like domain walls that are parallel to one of the crystallographic axes of $\text{Bi}_4\text{Ti}_3\text{O}_{12}$ are not compatible with the criterion of Fousek and Janovek ^[2] concerning the prediction of domain wall orientations. Since their phenomenological theory was developed for an infinite, perfect ferroelectric single crystal, our findings show that at the mesoscopic scale the thermodynamic approach needs further refinement.

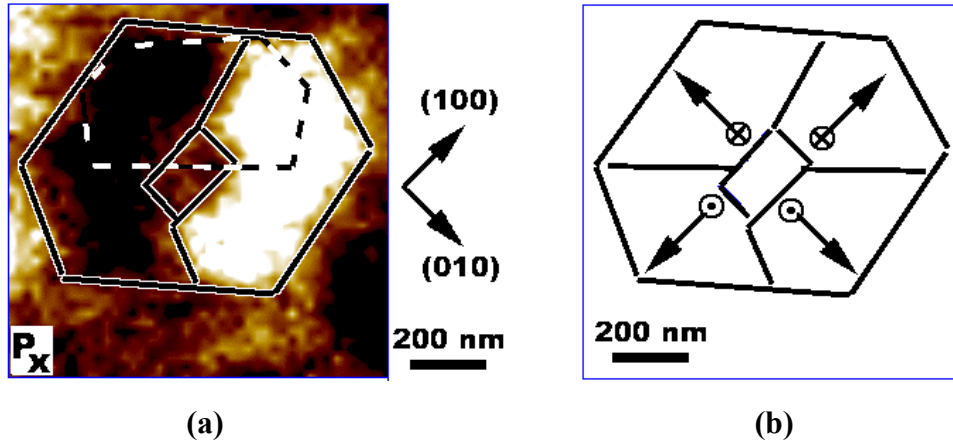


Figure 42 Deduction of the polarization orientation induced in the c -oriented $\text{Bi}_4\text{Ti}_3\text{O}_{12}$ film. **(a)** High magnification of the in-plane piezoresponse image Figure 41d. The lines mark places with high piezoresponse level. The dashed contour was taken from Figure 41c and limits the region with a high negative piezoresponse signal (the polarization *clearly* has a component oriented top-to-bottom). **(b)** The domain structure deduced from piezoresponse images and the known crystallographic orientation.

In conclusion, measurements performed on thin films of different members of the Aurivillius family revealed the following:

- As deduced from structural analysis and a few macroscopic experiments on films with *preferential* orientations, a ferroelectric behavior was found only in the non- c -oriented grains, and also for the c -oriented matrix of $\text{Bi}_4\text{Ti}_3\text{O}_{12}$, an odd- n member of the family. The piezoelectric response along the c -direction of the even- n members of the BLSF was *always* under the noise limit of the setup. The results indicate the presence of a spontaneous polarization only along the crystallographic $[100]_{orth}$ direction, with the exception of $\text{Bi}_4\text{Ti}_3\text{O}_{12}$, which has also a small component along the $[001]_{orth}$ direction.
- Individual non- c -oriented grains of SBT and $\text{BaBi}_4\text{Ti}_4\text{O}_{15}$ as small as 100 nm in lateral size possess very well defined rectangular-shaped hysteresis loops. However, the films are not homogeneous and the hysteresis parameters differ from one grain to another. In contrast, the c -oriented matrix did not respond piezoelectrically even after strong local poling.
- An internal bias field exists at the bottom electrode - ferroelectric film interface, a bias that causes a negative initial polarization (top-to-bottom) and, sometimes, also the backswitching of the positive domains.

- Indications on the occurrence of 90° domain switching in SBT films were found. However, further investigations are needed, especially by detecting the in-plane component of the polarization (which was not fully successful yet).
- Some particular gray and very thin regions were found in the non-*c*-oriented grains of SBT, which are very stable against poling, but which seem not to disturb the switching of the rest of the grain. These regions need further investigation, too.
- A very particular response of Bi₄Ti₃O₁₂ to poling pulses was found in the non-*c*-oriented grains, as well as in the *c*-oriented matrix. This behavior is explained in terms of the special (monoclinic) symmetry of bismuth titanate which facilitate the manifestation of the in-plane polarization. In-plane polarization is indeed detected and revealed that the film is polarized by the SFM parallel to the surface, a somewhat unusual, but understandable phenomenon if the exact field distribution under the SFM tip is taken into account. However, a consistent deduction of the polarization orientation in these regions, which would be in agreement with the TEM data, could not be found. If all the components of the piezoelectric tensor were known, this problem could probably be solved.
- The conditions for domain wall orientations predicted by the thermodynamic theory (developed for infinite, free, ideal single crystals) were found not to be fulfilled in epitaxial films of Bi₄Ti₃O₁₂, at least *not locally* on a mesoscopic scale.

5.4 Patterned nanostructures

In view of the prospective integration of ferroelectric materials into microelectronics it appears necessary to decrease the size of the device structures. In particular, for the prospective ferroelectric random access memory, the ability to scale down the ferroelectric properties is an imperative task in order to be competitive with other information data storage media. For this purpose, two main achievements have to be realized. The first one is the fabrication of memory cells having sizes in the submicron range, thus fulfilling the requirements for a FeRAMs in the memory density range of one or several Gbit per chip. The second is to study how these cells behave at sizes in the range of hundreds of nanometers and below. The main problem that may occur, predicted by some theoretical calculations ^[150], is whether or not the ferroelectric properties are altered by the size reduction.

The fabrication of arrays of *independent* ferroelectric cells was achieved in our group by electron beam direct writing as described in Sect. 3.4.3. This subchapter addresses the characterization of their ferroelectric behavior.

A first approach to check the ferroelectricity of individual cells consists in recording piezoelectric loops, and visualizing the domains formed (and switched) within the structure. Further characterization implies the observation of the stability of the domain structure under different conditions like poling of the neighbouring cells (testing of crosstalk between cells) and number of switching cycles (fatigue measurements).

5.4.1 Control of the domain pattern in mesoscopic structures

Fully successful "writing" and "reading" of ferroelectric domains within 1 μm cells is illustrated in Figure 43. The structures appear without an initial domain pattern, as can be seen from the upper left cell in Figure 43b. However, high resolution investigations (such as AFM with a sharp tip) revealed grain sizes of 20 nm or less. The detection of the grains was not possible in piezoresponse mode due to the tip apex, estimated to have a radius of 30-50 nm (the grains are even not distinguishable in the topographic image Figure 43a).

The SFM tip was positioned at the center of each of the numbered cells and piezoelectric hysteresis loops were acquired. As can be seen in Figure 43c the behavior of the patterned structures is reasonably uniform and well reproduced, with variations of less than 20% in the hysteresis parameters. The ferroelectric domains induced in each of the cells characterize the saturation regions of the corresponding hysteresis loops, after applying the maximum voltage used in the cycling: +30V for the grains No. 1 and No. 2, and -30V for the grain No. 3. The lateral size of the domains is several hundreds of nanometers, larger for the negative domain than for the positive ones.

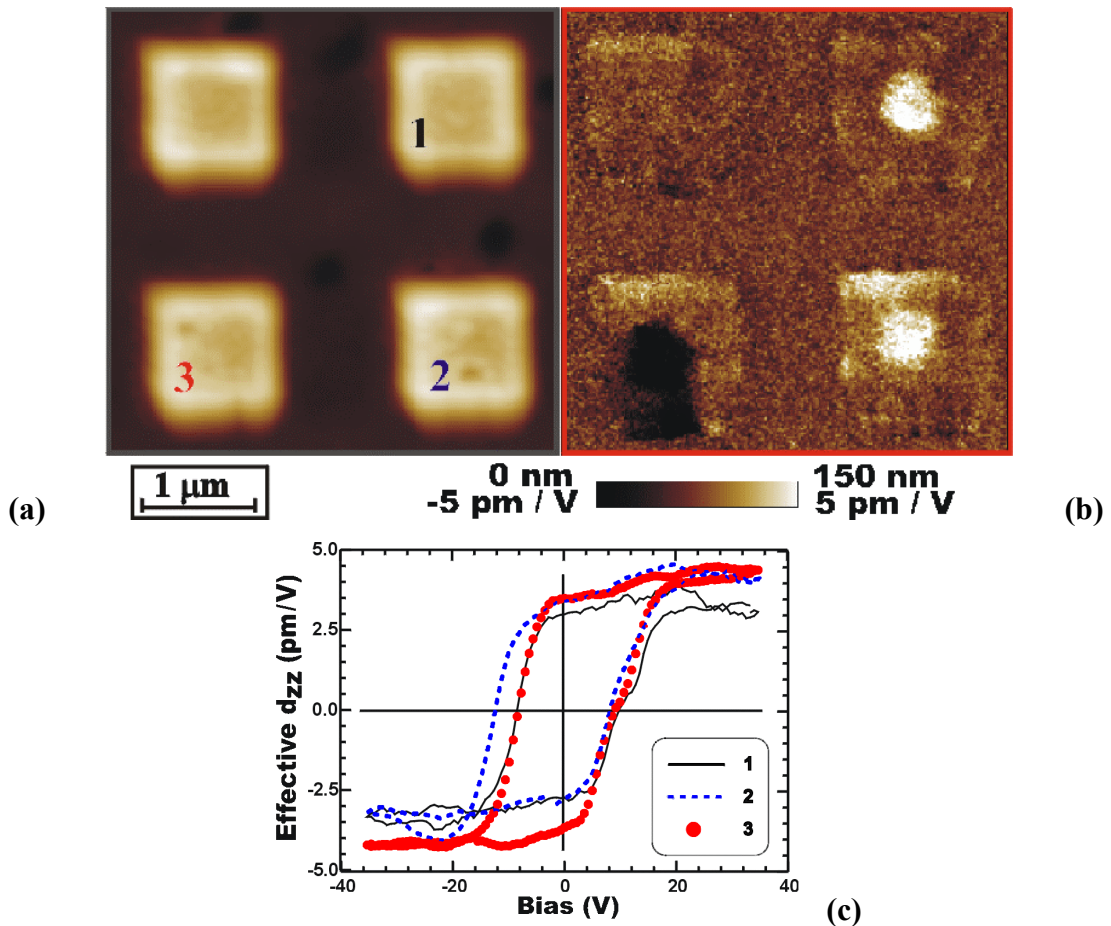


Figure 43 Ferroelectric behavior of PZT structures 1 μm in lateral size. (a,b) Topography (a) and piezoresponse (b) images simultaneously acquired after the poling. (c) Local hysteresis loops acquired in the center of the cells numbered in (a). The cells No. 1 and 2 were left positively polarized and cell No. 3 negatively. No change in topography was detected after poling.

Similar results were obtained from the 500 nm lateral size cells (cf. Figure 48a,b below). No mutual influence of the cells was detected; the cells could be tested and switched independently, therefore the crosstalk between cells can be ruled out, at least down to the cells 250 nm in lateral size, and 250 nm apart one from another.

Unfortunately, imaging of smaller structures (300 and 100 nm lateral size) failed due to the tip shape. The tip apex did not penetrate into the space between the cells down to the substrate, and consequently the images were highly distorted, representing actually a superposition of the real topography and the tip contour.

The behavior of the 1 μm structures was further tested in order to check the stability of a polydomain structure and also the dependence of the properties on the probing point. The results of the experiments performed on one cell are summarized in Figure 44.

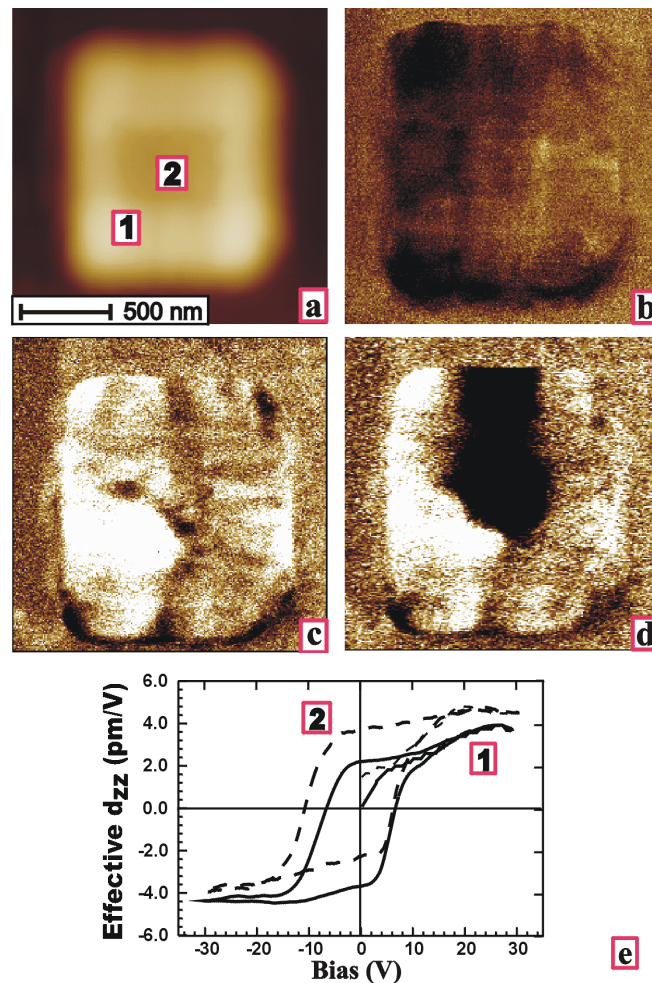


Figure 44 Switching experiments on a 1 μm \times 1 μm \times 100 nm PZT structure. (a,b) Topographic (a) and piezoresponse (b) images simultaneously obtained before poling. (c) Piezoresponse image acquired after poling at the point marked “1” (the last voltage applied was +30V). (d) Configuration of domains formed after poling at the point marked “2” (the last voltage applied was -30V). (e) Hysteresis loops measured at the regions marked “1” (full line) and “2” (dashed line) in the topographic image (a).

The topography (Figure 44a) and the initial polarization state (Figure 44b) were first acquired. The piezoelectric response shows a weak dark contrast, indicating a small negative

preference for the initial polarization orientation. Then the SFM tip was positioned successively on two different places of the cell, first close to one of the corners and then in the center. These positions are indicated by numbers “1” and “2” in the topographic image. From each point a hysteresis loop (Figure 44e) was recorded.

The last voltage applied to point “1” was +30 V and to point “2” –30V. Two opposite domains were created, with lateral sizes of $\sim 500 \text{ nm} \times 350 \text{ nm}$ and $\sim 700 \text{ nm} \times 400 \text{ nm}$, as can be seen in Figure 44c acquired after the local poling of both regions of the cell. Although the two places were poled with the same bias amplitude and pulse width, the negative domain is much larger ($\sim 150\%$) than the positive one. This is a clear indication of a preferential switching direction in the structure. This asymmetry can be ascribed to the differences in the two interfaces with the two electrodes (the Nb-doped SrTiO_3 substrate and the highly doped silicon tip) as suggested for macroscopic ferroelectric capacitors^[160].

By comparing the two loops acquired from points separated by 400 nm a slight difference can be observed: The hysteresis loop of the center shows a higher coercive field and has a better symmetry with respect to the d_{zz} -axis than the other one. This fact suggests that in the proximity of the edge the effect of either depolarizing fields and/or surface states become significant.

Experiments performed on cells having 500 nm in lateral size revealed that poling at the center results in the switching of the entire cell, as shown by the cells in the left column of Figure 45b. However, two opposite domains could be induced in the upper right cell by subsequent poling in the middle (negative poling) and at one of the corners (positive poling) of the cell. The resulting domain pattern was stable on the experiment’s time scale (several tens of hours). The positive domain has about 200 nm in lateral size and represents the smallest domain we could write and subsequently read on these structures.

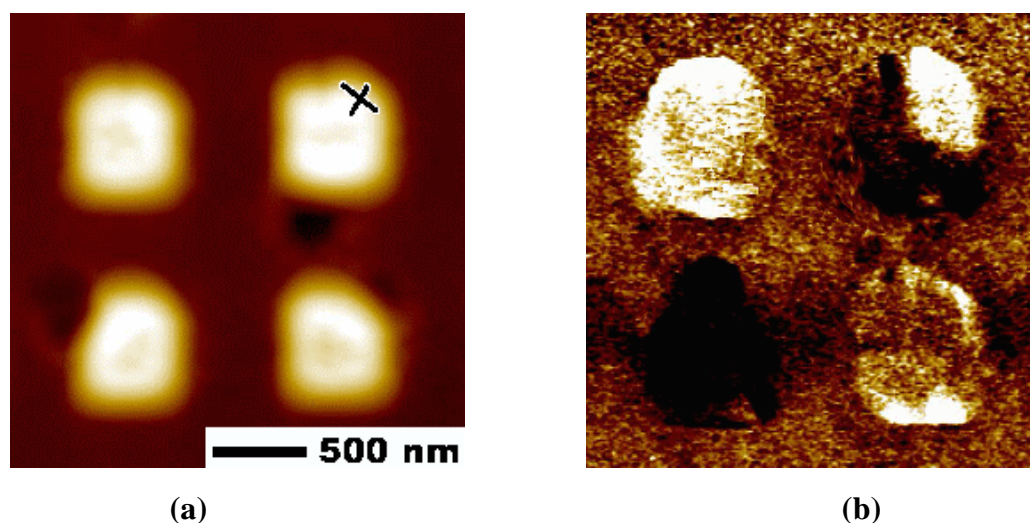


Figure 45 Domain control in 500 nm lateral size structures. **(a)** Topography. **(b)** Domain image of the cells after poling: The cells in the left part were positively (upper cell) and negatively (lower cell) poled with the tip fixed at the center. The upper right cell was first negatively polarized with the tip fixed in the middle, then positively polarized with the tip fixed above the upper right corner.

Extremely important in memory cell arrays is to prevent the memory state of one cell to be influenced by the memory state or by the processes involved in writing or reading the state of the neighboring memory cells. This phenomenon called *crosstalk*, represents a challenging problem in the case of magnetic storage media at sizes in the sub-micron range. The results presented in Figure 45b clearly demonstrate that, in the case of the prospective *ferroelectric* memories, writing and reading of one single memory cell in an array of cells of 500 nm in lateral size with 500 nm spacing does not affect by any means the polarization state of the neighboring cells. This fact represents a significant achievement of the present work, proving that the ferroelectric cells fulfill the conditions requested for the use in a high-density FeRAM array*.

5.4.2 Scaling down of ferroelectricity

Although piezoresponse imaging did not result in reliable domain *images* in the case of PZT structures smaller than 500 nm in lateral size, it was still possible to fix the SFM tip over the desired place and to sweep the bias for *local hysteresis loop* measurements.

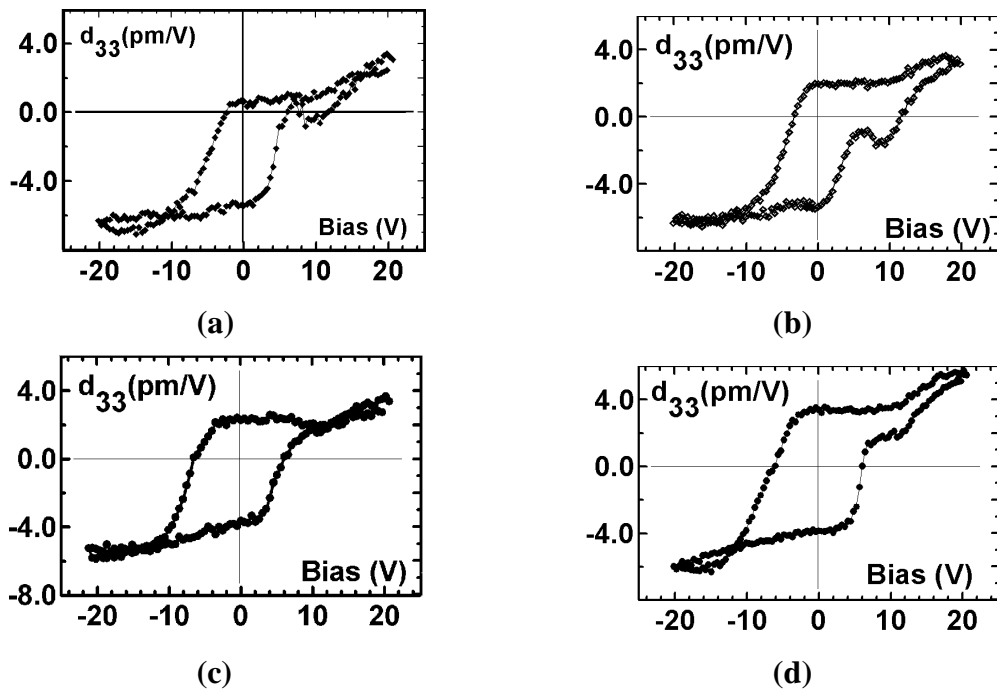


Figure 46 Piezoelectric hysteresis loops of PZT cells with: (a) 100 nm, (b) 300 nm, (c) 500 nm and (d) 1000 nm lateral size.

The ferroelectric behavior of patterned PZT structures with lateral sizes of 100, 300, 500 and 1000 nm was proven by means of local piezoelectric loops acquired from several cells of each size. The results are shown in Figure 46(a-d). In order to compare the ferroelectric behavior for different cell sizes, it is very important to emphasize that for this experiment, the

* The absence of a crosstalk between the nanostructures in our results reported in Ref. 80 has attracted the consideration of NATURE, which has mentioned the ability of our group to create ferroelectric memory arrays, as well as to write / read *individual* memory cells: P. Ball, "Technology: The computer that doesn't forget" in Nature science update, Friday, 24 Sept. 1999 (<http://helix.nature.com/nsu/990930/990930-1.html>).

four categories of cells were prepared on the same substrate onto an area of $50 \times 50 \mu\text{m}^2$, therefore under similar conditions (cf. Figure 13 in Sect. 3.4.3). Moreover, the hysteresis loop measurements were achieved using the same SFM tip, within the same experimental session. Therefore, it can be assumed that the results really reflect the sole effect of the lateral size.

There are no major changes in the ferroelectric behavior with decreasing the lateral size by one order of magnitude in the mesoscopic range (hundreds of nanometers). Both hysteresis parameters $2d_{zz}$ and $2E_C$ are comparable and within the variation range observed in each set of cells. However, the size of the structures did systematically influence another hysteresis parameter: the vertical offset of the loop. The absence of a top electrode in the experiments caused an asymmetry between the bottom electrode and the highly doped silicon tip, which leads to the vertical offset of the loops. This asymmetry of the loops was found to be size dependent, the hysteresis loops of smaller structures being strongly shifted into the negative direction of the vertical axis.

The asymmetry of a ferroelectric hysteresis loop is usually caused by the preference of a certain polarization state over the other in ferroelectric bistable states, a phenomenon called imprint and also observed in macroscopic measurements^[161,162]. In the macroscopic measurements of polarization this asymmetry results in a shift of the hysteresis loop along the electric field axis, as the vertical position of the loop is arbitrarily set. This is due to the fact that the determination of a charge (or a polarization) from an electrical measurement is done by integrating a current during a certain period of time, and this determination needs an integration constant which usually is not known. Therefore, the polarization hysteresis loops are usually centered along the polarization axis^[163], and as a consequence, the imprint in the ferroelectric capacitor appears as a shift along the field axis, and is described in terms of an internal bias field^[162,164]. In contrast, the piezoelectric displacement measured is perfectly well defined, and has an absolute value. Therefore, the calculation of the polarization from piezoelectric data using Eq. 10a in Sect. 2.2 is considered as an *absolute* method to determine the ferroelectric polarization^[89,165]. In the same way, a vertical shift (or the offset along the d_{zz} -axis) of a piezoelectric hysteresis loop can be associated with a region having a non-switchable polarization and therefore a preferred polarization direction, which thus can be called imprint, too. For convenience, to eliminate the effect of the different shapes of the hysteresis loops, we may define the imprint also as a *relative offset*, i.e. as the median d_{zz} -position of the zero-field piezoelectric coefficients, with respect to the distance between them^{*}:

$$\Omega = \frac{(d_{zz}^+ + d_{zz}^-)/2}{d_{zz}^+ - d_{zz}^-} \quad \text{Eq. 33}$$

where Ω denotes the relative offset, and d_{zz}^+ and d_{zz}^- are the zero field piezoelectric coefficients of the hysteresis loop, including their sign.

Calculations of the imprint (as defined in Eq. 33) with d_{zz} -values from the hysteresis loops of Figure 46, showed a strong dependence on the cell size (Figure 47). In the light of the studies found in the literature, this size dependence could be explained assuming the presence of dipolar defects in the vicinity of the cell surface. This explanation is further developed in the next chapter, Sect.6.4.

^{*} The distance between the zero-field coefficients on a piezoelectric hysteresis loop is usually denoted $2d_{zz}$ (as the distance between the coercive fields is denoted $2E_C$).

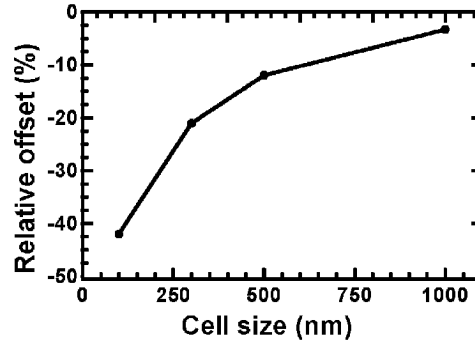


Figure 47 Size dependence of the relative hysteresis shift (imprint) in mesoscopic cells (d_{zz}).

5.4.3 Fatigue in submicrometer devices

Ferroelectric fatigue is defined as the loss of switchable remanent polarization in a ferroelectric material as a function of the number of bipolar switching cycles. The endurance to polarization switching of the patterned PZT cells was tested in order to compare it with the fatigue of macroscopic samples reported in the literature.

In Figure 48 fatigue measurements performed on a 500 nm PZT structure are shown. This experiment was completed at the center of the cell No. 1 of Figure 48a, by applying an AC voltage having an amplitude of 7 V and a frequency of 5kHz. To demonstrate that the tip-to-sample contact did not deteriorate during the cycling of cell No. 1, the neighboring cell (No. 2) was used as a reference. Before and after fatigue measurements, the hysteresis loop of each cell was acquired. Cell No. 1 was left each time in the positive polarization state (white contrast in the image) and cell No. 2 was left negative (polarization towards the bottom electrode, black contrast).

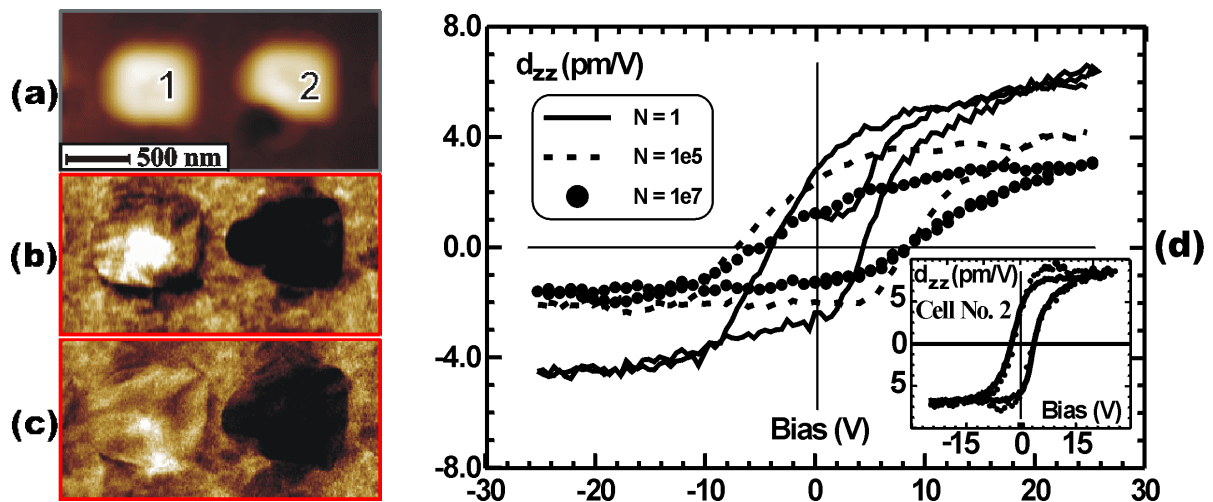


Figure 48 Fatigue measurements performed on one of the 500 nm PZT structures. (a) Topographic image of two PZT cells. (b,c) Domain structure of the same area before (b) and after (c) fatigue of cell No. 1. (d) Hysteresis loops of the cell No. 1 before cycling (—), after 10^5 cycles (---) and after 10^7 (●) cycles. The inset shows the hysteresis loops of cell No. 2 before (—) and after (●) fatigue of cell No. 1.

The images shown in Figure 48b-c represent the piezoresponse of the cells before and after 10^7 cycles on cell No. 1. The fatigue experiment of cell No. 1 was interrupted after $N=10^5$ cycles in order to acquire a hysteresis loop (Figure 48d). As shown by the hysteresis loop data in Figure 48d, after $N=10^5$ polarization reversals the remanent piezoelectric coefficient was not affected significantly; only the maximum value of the piezoelectric coefficient decreased and the coercive field increased while cycling the ferroelectric cell. Further fatigue of the cell up to $N=10^7$ cycles led to a decrease of the remanent piezoelectric coefficient down to 50 % of the initial value. Unlike in fatigue experiments performed on thin films^[89,166], no shift along the d_{zz} -axis can be noticed. The piezoresponse image of cell No. 1 in the fatigued state (Figure 48c) suggests that pinning of domains takes place in the entire volume of the structure .

Taking into account that the grain size of the structures is of the order of 20 nm, it is not possible to specify the role of grain boundaries in domain pinning, because the grain size is below the lateral resolution of the SFM. It has been suggested that for thin films (up to 1.8 μm thickness) a high density of frozen-in domain walls in the entire volume of the structure implies an increase of permittivity^[121], whereas no asymmetry of the polarization hysteresis is expected if nucleation of reversed domains is inhibited at the electrodes. For thick films (down to 70 μm thickness), a decrease of the permittivity with the number of polarization switches has been reported^[95]. Since the slopes of the hysteresis loops in Figure 48d suggest the decrease of the dielectric constant with the number of cycles, we suppose that fatigue of this nanostructure occurs via inhibition of the nucleation of domains at the grain boundaries, in the entire volume of the structure^[167].

The main results obtained on patterned PZT structures can be summarized as follows:

- No effect of the size could be observed in the ferroelectric hysteresis: Both coercive field and piezoelectric coefficient are the same for all sizes, within the experimental errors. However, an internal bias seems to be present and to increase as the size of the ferroelectric cells decreases.
- It was proven that 500 nm cell in lateral size could be written and read individually without any influence on the polarization state of the neighboring cells. That is, from the device viewpoint, no crosstalk is expected between the cells of the prospected high-density FeRAMs. Moreover, there is some indication that the crosstalk is absent down to 300 nm lateral size with 300 nm spacing.
- Ferroelectric domains were written into and read out of 1 μm and 0.5 μm lateral size cells. Even two oppositely written domains were perfectly stable for a long time, without any indication of further alteration of the piezoelectric contrast (and therefore polarization).
- Fatigue measurements performed on the cells of 0.5 μm lateral size revealed the normal behavior for PZT films, without any indication of an influence of the size effect on the fatigue.

6. Discussion

The scope of this work was to study ferroelectric phenomena at a local scale on different materials in view of their prospective use in non-volatile memories.

An analysis of the available techniques by which ferroelectricity can be probed at a level as small as possible revealed that the most suitable method is the so-called “piezoresponse-SFM”, a scanning probe technique, which is based on the converse piezoelectric effect (present in all ferroelectric materials). The reason for this choice is that this technique allows both the *detection* and *modification* of the ferroelectric state using the same experimental setup, down to a resolution of 10 nm. Special attention has been paid to explore and to point out the methodology to extract as much information as possible about the local material properties from the physical quantities accessible with this method. The capabilities of the experimental system were tested using barium titanate single crystals, whose properties are well known in the literature, both from macroscopic and microscopic characterization.

Ferroelectricity was investigated by means of the electromechanical response to an AC excitation voltage on a series of samples, with ferroelectric structures of decreasing size:

1. Polycrystalline *continuous* films of PZT consisting of grains with random orientation and sizes in the 100 nm - 600 nm range. The thickness of the films was in the same range, 200 nm up to 600 nm. These films can be considered as a two-dimensional assembly of ferroelectric entities.
2. *Individual* non-*c*-oriented grains embedded in a *c*-oriented matrix of different epitaxial films of BLSF materials. The grain size was again in the mesoscopic range (hundreds of nanometers), comparable with the contact area between the SFM tip and the grain i.e. the area from which the electromechanical data are collected. These grains, embedded into a background with *c*-orientation, were not completely independent or stand-alone, since they were surrounded by a matrix of the same material. However, since they were switchable independently from each other, they may be considered as individual grains.
3. A set of fine-grained *individual* ferroelectric structures having finite lateral sizes ranging from 1 μm down to 100 nm. These sizes are close to the experimental resolution limit (which is the contact area between the SFM tip and the structure).

The ferroelectric behavior was studied by means of domain imaging and local electromechanical probing. Although each experimental result was shortly discussed already, some general discussion will now be provided.

6.1 The ferroelectric domain structure

The configuration of the ferroelectric domains is the most important factor that determines the macroscopic ferroelectric properties, controlled by the domain nucleation and the domain wall mobility. From piezoresponse images a large variety of domains could be observed, starting from the single domain state that was found in BaTiO₃ single crystals over large areas and

down to very small (100 nm) and isolated grains of SBT containing even multiple domains of 30 nm in lateral sizes (like Figure 31 in Sect. 5.3.3).

Unlike other methods, scanning microscopy methods, in particular piezoresponse SFM, permit to verify whether the conditions for stability of the domain structure still hold in the range of tens of nanometers. It was found, for instance, that the rules found for the macroscopic equilibrium of ferroelectric domains are still valid at this scale, at least under normal conditions (moderate contact force and electric fields applied). For example, 90° domain wall structures, typical for BaTiO₃ single crystals, where they have a domain width of 10 μm - 20 μm (as in Figure 18, Sect. 5.1.2), were found in PZT (30/70) grains of only 500 nm size with domains of less than 10 nm in width (see Figure 23, Sect. 5.2.2). The same holds for the 180° domain walls. It may happen, however, that extreme local conditions such as stress from neighboring grains or from the substrate, or an intense poling field from the SFM tip induce charged domain walls or metastable domain states that are not allowed within equilibrium thermodynamics.

A common belief for simple perovskites is that grain sizes below 150 nm should be stable monodomains^[153], and therefore would exhibit bad switching properties due to the inhibition of reverse domain nucleation. In switching experiments we indeed found that grains of 500 nm usually take the single domain state when poled at saturation (Figure 27, Sect. 5.2.4), but also that they can assume a multidomain state for lower poling voltages. This case was shown, for instance, in Figure 28c (Sect. 5.2.4), where the small domain nucleated was stable at least for several hours. Also, it was found that the domains may extend into the adjacent grain but do not necessarily extend over the whole grain. In the case of SBT, grains of 200 nm in lateral size may still exhibit a domain structure, even after poling at saturation.

Domain imaging in small grains of SrBi₂Ta₂O₉ revealed a very fine and very stable domain structure, grains of different sizes usually exhibiting domains of less than 50 nm in width. Figure 31 (Sect. 5.3.3), for instance, shows a grain 250 nm in length divided into five stripe domains 50 nm in width each, and a smaller grain, about 150 nm in diameter, shows three similar domains. In contrast, there are two other small grains discernible in the flat background, each about 50 nm in lateral size, which are in the single domain state. The hypothesis could be put forward that, at least for this type of ferroelectric systems (*a*-oriented grains of SBT embedded into the *c*-oriented matrix), grains under 50 nm are single domains. This value is, however, very close to the lateral resolution of the experiment, estimated to 30 nm – 50 nm. Therefore, even finer domains could exist (also in grains that appear with gray contrast) without being visible due to the too large probing contact area. Assuming nevertheless that in SBT the smallest domain size is 50 nm, it is possible to compare the domain wall energy in different materials using the relation^[5]:

$$\sigma = \frac{d^2 \epsilon^* P_0^2}{t}, \quad \text{Eq. 34}$$

where *d* is the smallest stable domain size in a periodic domain structure having the thickness *t*, *P*₀ is the spontaneous polarization, *ε*^{*} is a constant related to the dielectric permittivities of the crystal, and *σ* is the domain wall energy density. Since the smallest stable domain observed in grains of similar sizes in BaBi₄Ti₄O₁₅ and Bi₄Ti₃O₁₂ was about 100 nm, it is

possible to predict that the domain wall energy density is at least four times bigger for the two materials than for SBT.

As a general feature, the bismuth layer-structured ferroelectric (BLSF) thin films studied in this work exhibit grains of non- c -orientation embedded into a flat c -oriented matrix. These grains, a few fractions of micrometer in lateral size, are either spherical (as seen in the SEM images) or rectangular with an aspect ratio higher for $\text{Bi}_4\text{Ti}_3\text{O}_{12}$ than SBT and $\text{BaBi}_4\text{Ti}_4\text{O}_{15}$. The formation of these structures is an effect of the high anisotropy of these materials, which leads to an anisotropic grain growth during deposition. The piezoelectric contrast is always zero in the c -oriented matrix, except for $\text{Bi}_4\text{Ti}_3\text{O}_{12}$ where domains can be induced by poling the samples. The non- c -oriented grains exhibit a well-defined piezoresponse, slightly stronger in spherical grains than in the rectangular-shaped grains. The magnitude of the signal from the grains will be discussed below (Sect. 6.3). The sign of the piezoresponse indicates that the polarization in the as grown state is usually oriented towards the bottom electrode, which consists of an epitaxial LaNiO_3 film or of a Nb-doped SrTiO_3 crystal. A possible reason for this initial orientation of the spontaneous polarization is the negative carrier concentration present in the bottom electrode. Negative charges in the bottom electrode, near the interface with the ferroelectric film, create an electric field that favors the top-to-bottom orientation of the polarization in the ferroelectric. However, this hypothesis has to be checked, for instance by depositing films on oxide electrodes with a p -type conduction. In this case the onset of polarization should be positive.

In all the BLSF films investigated, the domain walls in the rectangular grains were parallel to the c -axis of the grains, as revealed by a comparative analysis of piezoresponse measurements and HRTEM investigations of grains in the same area of the samples. The occurrence, under certain circumstances, of domain walls with other orientations was followed by the pinning of these atypical domain walls after less than ten switching cycles of the polarization (see Sect. 5.3.5).

Ferroelectric domains induced in isolated PZT nanostructures were stable at least on the experimental time scale (a few days). Writing and imaging of two domains within the same structure of 1 μm or 500 nm in lateral size was also achieved. The smallest domain we could write and further image in these very fine-grained nanostructures was about 200 nm in size, as shown in Figure 45, Sect. 5.4.1 (the positive domain in the upper right cell). We believe that these domains certainly extend through the entire thickness of the structure.

Another disputable aspect in piezoresponse imaging of ferroelectric domains is the depth into the sample over which the detected domain extends. This aspect may be defined as the “ z -sensitivity” of the method and is basically determined by the ferroelectric material investigated. Calculations with the simple model described in Appendix A indicate that 90% of the voltage applied between the SFM tip and the bottom electrode is applied to about 30% of the sample thickness (see Figure A 3b in Appendix A) for a permittivity of the ferroelectric material of $\epsilon_r = 100$. Other simulations using the finite element method have estimated the “active” layer that piezoelectrically responds to be 30 nm out of 128 μm thickness of a BaTiO_3 single crystal^[168] and a similar value is suggested for a 400 nm thick epitaxial PZT (20/80) film^[169].

Rather contradictorily, Ahn et al. ^[40] have experimentally *demonstrated* the field effect in a PZT/SrRuO₃(110)/SrTiO₃(001) epitaxial heterostructure. Systematic and stable changes in the resistance of the SrRuO₃ layer were induced by poling the upper surface of the 400 nm thick PZT film with an SFM tip. In other words, the ferroelectric domains induced at the surface extended *throughout* the thickness down to the bottom electrode and reversibly modified its carrier concentration ^[40].

Our estimates (using the simple model described in Appendix A) regarding the penetration depth of the electric field have clearly established the following two aspects:

1. The permittivity is a very important parameter; higher values imply smaller fields inside the sample, as indicated by our simple model in Eq. A 4*. Therefore, the region which piezoelectrically responds will be very thin, and consequently the piezoresponse of high permittivity materials is concentrated to the near-surface region. For instance, in BaTiO₃ single crystals, one can estimate that the field penetrates 20 times deeper into the *c*-domains than into the *a*-domains ($\epsilon_a / \epsilon_c \approx 4000 / 200$).
2. The aspect ratio *contact area / film thickness* of the electrostatic system plays an important role, too. A large contact area (of blunt tips for example) or a small thickness of the ferroelectric film makes the geometry to get closer to that of a planar capacitor, therefore decreasing the degree of non-homogeneity of the electric field. As a consequence, the piezoresponse of thin films may reflect the contribution of a larger percent of the film depth than the piezoresponse of thick samples. The stray field, however, remains important in both cases and it may polarize the region parallel to the film plane.

Therefore, we may assume that the piezoresponse images of thick (more than about 1 μm) samples illustrate only the domain structure near the surface, whereas in thin films (less than 500 nm in thickness), the whole thickness of the film contributes to the measured piezoresponse. Nevertheless, these assumptions depend on the specific experimental circumstances, e.g. on the permittivity and the grain size of the sample.

6.2 Piezoelectric and ferroelectric hysteresis

The procedures for recording the hysteresis loops were explained in Sect. 4.3.3. It is obvious that these loops are not usual hysteresis loops, in a classical sense. While the in-field loops are similar in nature to the small-signal capacitance measurements, the remanent loops are of a more particular type. They reflect in fact the retention characteristics after the application of a particular voltage pulse and after the specific history of polarization states. In contrast, the in-field loop characterizes a domain state in the presence of the electric field applied, a ferroelectric state that may not remain after the suppression of the field. This is actually the case in many macroscopic measurements, where the polarization value read a few fractions of a second after the field removal is much lower than the zero field polarization of the

* V_{M2} inside the ferroelectric is proportional to $(\epsilon_2)^{-1}$.

(dynamical) in-field loop. Therefore, the hysteresis loop of the relaxed state (defined as *remanent hysteresis loop* by our group ^[73]) is much more suitable not only for local electromechanical measurements but also for ferroelectric characterization in general.

Interpretation of the hysteresis loop shape

Whereas the physical meaning of the saturation parts on the hysteresis loops is clear, the meaning of the intermediate points of the loops, near the coercive voltage, is not trivial. In the ideal case, for the 180° switching of a single grain, the loop should be perfectly rectangular-shaped, similar to that of grain No.1 in Figure 32 (Sect. 5.3.3). This would indicate that once the local threshold field has been reached, nucleation and growth of an opposite domain take place in the whole volume probed within some nanoseconds, giving rise to an ideal square-shaped hysteresis loop. The experiments have shown, however, that abrupt switching from one state to another only rarely occurs, depending on the material, grain size or grain orientation. Nucleation and growth of the domains actually take place over a set of pulses applied with amplitudes around the coercive voltage, suggesting intermediate *stable* states of the domain configuration. Compared with macroscopic switching it appears very unusual that switching - a highly non-equilibrium process - occurs by passing through (at least) metastable states. However, the different conditions imposed on the system in the case of the local piezoresponse and macroscopic ferroelectric polarization hysteresis make them difficult to compare. In the SFM measurements only one nucleation center is activated, whose evolution depends on the local environment, whereas in macroscopic measurements a well-defined electric field is applied to a statistical system of domains (each with its own parameters) that evolve together, with a strong mechanical and electrostatic coupling ^[170,171].

The interpretation of the transition regions between the two saturated states of polarization on a hysteresis loop needs a special treatment. As mentioned above they characterize intermediate switching states as “seen” by the tip through the small piezoelectric oscillations induced in a certain volume underneath the contact region. During polarization reversal, in this volume, mainly nucleation and growth of opposite domains occurs, at least for those domains having the polarization oriented perpendicular to the film plane. Nevertheless, in order to minimize the total energy of the system, either ferroelastic switching or motion of an existing domain wall from a previous position to a more stable one may also take place, as imposed by the field and by the specific boundary conditions. The first hysteresis loop of grain No. 2 in Figure 32 (Sect. 5.3.3) certainly resulted from a ferroelastic switching, and as consequence, a strange loop was recorded during this 90° switching. Simultaneous recording of both out-of-plane and in-plane hysteresis loops will help the elucidation of these processes, specific to *local* probing experiments.

Since the system evolves according to the local boundary conditions, the hysteresis loops recorded at different places should, at least in principle, be different. Local strains and electric fields produced by nearby grains should influence the local behavior. Indeed, this is a general trend that was observed during this work, where differences in hysteresis parameters were found not only between grains, but also within the same *individual* grain, less than 300 nm in lateral size ^[58,60]. The hysteresis loops in Figure 44 (Sect. 5.4.1) are another example where the presence of the edges of the structure (1µm in the lateral size) shifts the onset of polarization downwards.

Considerations on numerical values

The values obtained for the piezoelectric coefficients are calculated as described in Sect. 4.2. Those of the *local* saturation piezoelectric coefficients are typically 2 – 4 times smaller than the ones measured from macroscopic measurements on films, and about 10 – 20 times smaller than the bulk values. However, similar values have been reported in the literature from other piezoresponse SFM measurements [66,90,111]. The clamping of the film to the substrate (Appendix C) is not sufficient to explain the low experimental values of the effective piezoelectric coefficient even in macroscopic measurements on thin films [172]. Since piezoelectricity implies strain, which exists mainly at each 90° domain walls*, it is believed that the reduced number of non-180° domain walls in thin films (compared to the bulk) is responsible for the further decrease of the piezoelectric response [173]. In the case of the piezoresponse measurements, even more factors may cause the reduction of the effective piezoelectric coefficient. A few possible reasons for the very small values of the local piezoelectric coefficient measured (for example, 3 to 6 pm/V in BaTiO₃, compared to the bulk value of 86 pm/V) are:

1. The high permittivity of ferroelectrics

Due to the high permittivity (usually several hundreds), and also to the large thickness of the sample, the electric field is confined to a thin region near the surface, in the vicinity of the contact place (see Figure 9 in Sect. 3.2.4). This implies that only a small region of the sample will respond piezoelectrically to the AC testing voltage [168]. The region is clamped by the *immobile* surroundings not only in the film plane (as shown in Appendix C) but also perpendicular to it, and therefore the effective piezoelectric coefficient appears smaller than that of the film.

2. The very high electric field under the tip

Because the electric field is similar to that given by a point charge, therefore extremely inhomogeneous, the testing voltage (in the range of $2 V_{rms}$) may be high enough to switch the polarization in a very small region under the contact area, where the field exceeds the *local* coercive field. Occurrence of switching under the influence of the AC testing voltage, with the same frequency as the excitation, will lead to a decrease of the first harmonic response and to an increase of the second harmonic oscillation.

3. The adsorbed (water) layer at the surface

Any adsorbed surface layer with a relatively low dielectric constant will further decrease the field in the ferroelectric sample, due to the large permittivity of ferroelectric materials.

4. The contact force between tip and surface

A simple estimate of the stress applied to the sample for a contact force of $5 \mu N$ and a contact area of $\pi \cdot 40^2 \text{ nm}^2$ (as usual in the present measurements) leads to a value of 1 GPa . Such a huge pressure may considerably clamp the mechanical response of the sample.

* The contribution of the domain wall movements to the dielectric permittivities and piezoelectric coefficients is known in the literature as “extrinsic contribution”, which has to be added to those of the lattice (single crystal), called “intrinsic contribution”.

To obtain reasonable numerical values from local piezoresponse measurements, some scientists simply scale the average signal over a poled area with respect to the piezoelectric coefficient measured macroscopically. Other works use a standard sample, for instance quartz, to calibrate the signal. Despite these calibrations, the piezoresponse SFM measurements are not comparable with macroscopic piezoelectric measurements and are not really comparable among the different types of samples investigated each of them reflecting specific measurement conditions. Therefore, in this work, the values resulting from the direct calculations were given. In contrast, estimates of the electrostriction coefficient are of the same order of magnitude as those from macroscopic measurements on SBT polycrystalline films^[73], and even showed a better match for PZT and BaTiO₃ (single crystal).

6.3 Dependence of the local ferroelectric properties on the local crystallographic orientation

As already established, piezoresponse SFM allows to obtain information on the *existence* of polarization, and whether or not the material is *switchable*, in other words, to test for ferroelectricity. In our epitaxial films, the exact crystallographic orientation has been established by other means (XRD and HRTEM). The piezoresponse measurements have not only shown the absence of polarization along the *c*-direction for BLSF materials with even Aurivillius parameter, but also the impossibility to pole or to create domains in these regions. In other terms, *the complete absence of ferroelectricity along the c-direction* has been demonstrated.

It should be emphasized that in piezoresponse imaging it is not the polarization which is being sensed, but an induced *piezoelectric oscillation*. It was proven in Sect. 4.1 that the movement of the SFM tip reflects the induced vibration of the sample surface underneath. This piezoelectric oscillation should now be analyzed more in detail. At first, if we consider only the out-of-plane imaging, we can say that the physical quantity probed is certainly the piezoelectric coefficient perpendicular to the film plane. Therefore, the piezoresponse images represent, exactly speaking, *piezoelectric* and not ferroelectric domains. Although they are strongly correlated, as already explained in Sect. 5.2.3 and as it is shown more precisely in Appendix B, the piezoelectric oscillation detected is not strictly proportional to the out-of-plane component of the polarization even in the simple ferroelectric system PZT. If we look to BaTiO₃ (Appendix B, Figure A 4b) we immediately notice that the maximum in d_{zz} (the piezoelectric coefficient “seen” by the tip; see notations in Appendix B) appears along a direction making a large angle (about 52°^[174]) with the direction of the spontaneous polarization. This implies that out-of-plane piezoresponse imaging in BaTiO₃ does not describe simply the out-of-plane polarization, and that additional information is needed to deduce the actual ferroelectric domains. Such knowledge may be, for example, either the film orientation or the in-plane piezoresponse image. In the case of polycrystalline films, it may be difficult to extract information about the polarization. In fact the piezoelectric coefficient and the spontaneous polarization are still related, but this correlation depends on the specific orientation of each grain. The reason for this specific shape of the d_{zz} -surface of BaTiO₃ is the large value of its d_{15} piezoelectric coefficient (see Appendix B), which in turn is related (*via* Eq. 10c, Sect. 2.2) to the permittivity ϵ_{11} that is about 20 times larger than ϵ_{33} . Since no other

material studied in this work showed such large differences in the magnitude of the permittivities, we assume that the d_{zz} -surfaces of the materials with tetragonal symmetry approximate in shape the one of tetragonal PZT, given in Figure A 4a.

Therefore, for all materials having a tetragonal symmetry, the differences in the maximum induced piezoelectric coefficient could be expressed on the basis of the crystal orientation dependence of the piezoelectric coefficients. This was possible, because $d_{zz}(\theta)$ and $P_z(\theta)$ have the same trend, namely they are both at maximum for $\theta=0^\circ$, at minimum for $\theta=180^\circ$ and zero for $\theta=90^\circ$. In PZT polycrystalline films the difference in the behavior of the grains could be explained on the basis of different orientations of the grains (Figure 26 in Sect. 5.2.3). Although the symmetry of the BLSF is not exactly tetragonal, it is usually assumed that a small orthorhombic or monoclinic distortion does not significantly change the piezoelectric tensor. In fact, knowing the crystallographic orientation, our results demonstrate that a similar correlation between the longitudinal piezoelectric coefficient and polarization is indeed valid for all the even- n members of the BLSF materials.

Let us have a closer look on bismuth titanate. $\text{Bi}_4\text{Ti}_3\text{O}_{12}$ has a monoclinic symmetry and therefore 10 independent components of the piezoelectric tensor. Neto and Cross^[159] have measured the longitudinal coefficients d_{11} , d_{22} and d_{33} for single crystals, and separately calculated the other coefficients from previously published data. Using these values* the d_{zz} surface was calculated as a function of the direction as described in Appendix B for the tetragonal symmetry.

The result of this calculation is shown in Figure 49. Although there may be some other variants of the surface, this is the most probable dependency, in agreement with the measured coefficients. As can be immediately noticed in the figure, a maximum in the piezoelectric response can be reached in a direction parallel to $[100]$, but also a small piezoelectric activity exists along the $[001]$ direction. The ratio d_{11}/d_{33} is approximately equal to 4.

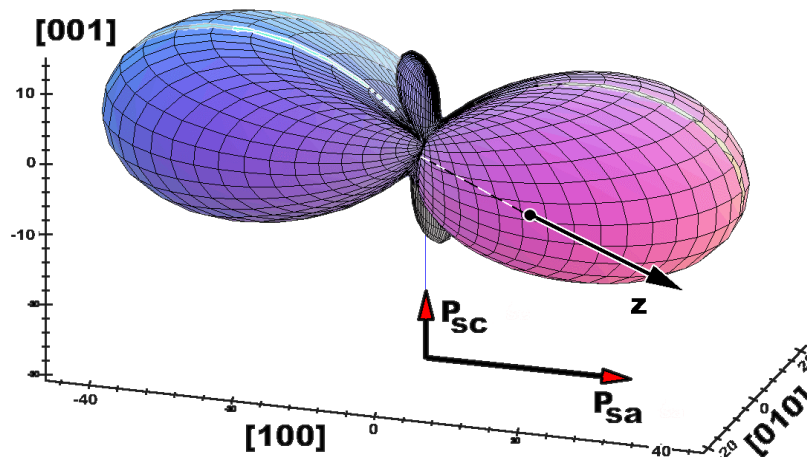


Figure 49 Expected dependence of the longitudinal piezoelectric coefficient on the measurement direction “z” in bismuth titanate. For the physical meaning of the surface plot see Appendix B.

Although about five times smaller than the bulk values, the piezoelectric coefficients in our measurements on $\text{Bi}_4\text{Ti}_3\text{O}_{12}$ epitaxial thin films (about 500 nm thick) revealed the same ratio

* They found a discrepancy between the calculated and measured d_{33} , so the *experimental* value was used for the piezoelectric coefficient along the c-axis.

for the piezoelectric coefficient of non- c -oriented grains and of the c -oriented matrix (see the zero-field piezoelectric coefficients in Figure 41b, Sect. 5.3.5).

6.4 Size effect studies in ferroelectrics

Studies of size effects in ferroelectric materials historically developed in the following directions:

- Three-dimensional approach at macroscopic level: The size of the sample is kept constant, but the size of the single crystalline constituents is decreased. More exactly, the bulk properties are studied as a function of the grain size. The conclusion is that ferroelectric properties deteriorate with decreasing grain size.
- One-dimensional approach: Two dimensions of the ferroelectric sample are kept constant and the film thickness is decreased. In simple perovskites (BaTiO₃, PZT) the grain size is strongly related to the film thickness (due to the isotropic grain growth) and their effects on the ferroelectric properties could be estimated separately only recently ^[153]. Experiments have shown that the grain size is the main factor involved in the deterioration of ferroelectric properties when decreasing the film thickness. The same was found for SBT films. Due to the anisotropic grain growth in SBT, the same grain size and consequently the same ferroelectric behavior was reported for films with thickness from 50 nm up to 500 nm ^[151].
- True three-dimensional approach, achievable by *decreasing all three dimensions of the sample*.

During this work the size effects on the ferroelectric behavior have been experimentally studied using the third approach, which from a physics point of view is the proper one. Our results clearly prove that the ferroelectric behavior *does not depend on the size at least down to 100 nm lateral size* of the ferroelectric “sample”. The one micron “samples” behaved as thin films when probed in the middle. Domains up to 500 nm lateral size were written and read as usual in very fine-grained thin films. Also, a multiple domain structure could be formed even in the 500 nm lateral size cells.

However, an increase of the vertical offset of the hysteresis loops was found with decreasing the structure size, an effect that may prevent the functionality of small memory cells. The vertical bias of the loops is certainly not related to the ferroelectric phenomenon, but most probably to the electrode asymmetry. Drawing the reciprocal of the relative offset (from Figure 47) versus the cell area it was noticed that the dependence can be fairly well fitted with a linear relation as shown in Figure 50. From the fitting parameters, the following empirical law was derived:

$$\Omega^{-1} = -\alpha A - \beta, \tag{Eq. 35}$$

where Ω is the relative shift of the hysteresis loop (as defined in Eq. 33, Sect. 5.4.2), A is the area of the cell, $\alpha = (28 \pm 3) \mu\text{m}^{-2}$ and $\beta = 1.9 \pm 0.2$. This dependence is difficult to interpret in the frame of the present imprint theories proposed in the literature. In the following, we will

try to relate our results to the two main attempts to explain the imprint of polarization in ferroelectric thin films.

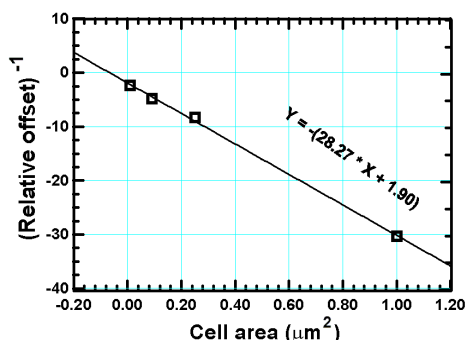


Figure 50 Size dependence of the reciprocal of the vertical hysteresis shift (imprint) in mesoscopic cells.

There are several reports in the literature on the effect of a layer with a fixed polarization on the leakage current^[160] and on the vertical shift of the piezoelectric hysteresis loop in the case of *epitaxial* films^[175]. According to the above studies, a lattice mismatch between the film and the substrate causes strong elastic in-plane strains in the film that build up a region with fixed polarization at the interface. The orientation of this strain-induced polarization depends on the lattice mismatch. If the lattice constant of the film is larger than that of the substrate, the polarization is directed towards the ferroelectric film. The size effect (in this case “thickness-effect”) comes from the fact that the influence of this non-switchable layer (which is supposed to have a constant thickness for a given ferroelectric-substrate interface) becomes more important as the overall thickness of the ferroelectric film decreases. In our case, however, the existence of a layer with non-switchable polarization cannot be caused by a lattice mismatch, since the PZT structures are not epitaxial, but polycrystalline with an average grain size of about 20 nm. Moreover, since all the cells have the same thickness of 110 nm, a non-switchable layer with a fixed thickness cannot explain the effect of the lateral size on the relative offset.

Another approach to explain the imprint is based on the assumption that an internal bias field is present inside the ferroelectric or at least in the vicinity of its interfaces with the electrodes. The association of this internal field with the voltage shift of the macroscopic hysteresis loop of the polarization is supported by the linear dependence of the hysteresis shift on the value of the polarization remaining after a sustained (long time) poling^[176,164].

We think that this is actually happening in our case, too, with the built-in electric field arising from the asymmetry of the ferroelectric-bottom electrode interface. In order to use the substrate as a bottom electrode, the mesoscopic devices were patterned directly onto Nb-doped STO substrates. Doping with niobium turns the perovskite strontium titanate into an *n*-type semiconductor^[177]. This may provoke a region depleted from charge carriers near the interface, since ferroelectric materials can be considered as semiconductors with low mobility charge carriers. The region depleted from charge carriers generates an electric field at the ferroelectric-electrode interface^[178], which in this case would be oriented top-to-bottom. This orientation of the bias field is in complete agreement with the sign of the offset found in our samples, for which the non-switchable layer also appears to have a spontaneous polarization

oriented top-to-bottom, therefore negative according to the convention used throughout this work (positive z-axis oriented bottom to top).

Next, we will try to explain the dependence of the offset *on the cell area* observed in our structures. The empirical relation expressed in Eq. 35 above, shows that the relative shift of the piezoelectric hysteresis loops of the cells depends on the reciprocal of a linear expression of the cell area. Using the linear dependence between the *effective* piezoelectric coefficient measured by the tip and the *effective* polarization underneath (Eq. 10a*, Sect. 2.2) we may deduce from Eq. 33 (Sect. 5.4.2) and Eq. 35 the ratio between the zero-field polarizations for the two oppositely polarized states:

$$\frac{P^+}{|P^-|} = \frac{\alpha A + \beta - 2}{\alpha A + \beta + 2} \quad \text{Eq. 36}$$

It should be mentioned that the exact physical processes occurring in ferroelectric films are presently not yet well understood, and finding the cause for the vertical shift of the loops remains an open question. For instance, the processing conditions, especially during the crystallization of the ferroelectric phase, have a very strong impact on the ferroelectric properties^[161,179]. Following Pike et al.^[180], and also Warren et al.^[176], we may suppose that the imprint (internal bias field) is given by a component of the polarization, further referred to as P_D , determined by the dipolar defects present in the ferroelectric materials. In our case, P_D is oriented top to bottom. We may also suppose that the net polarization in the ferroelectric structure is given by the sum of the ferroelectric polarization and the defect-dipole component. For the two zero-field states we therefore may write, assuming that the pure ferroelectric polarization is symmetric:

$$\begin{cases} P^+ = P_{ferro} - P_D \\ |P^-| = P_{ferro} + P_D \end{cases} \quad \text{Eq. 37}$$

Substituting Eq. 37 into Eq. 36, we find the dependence of the dipolar-defects component on the ferroelectric cell area (the sign is not included):

$$P_D = P_{ferro} \frac{2}{\alpha A + \beta} \quad \text{Eq. 38}$$

Eq. 38 can be explained if we assume that the defects are mainly located at the surface of the ferroelectric structure over a certain thickness δ . It follows that the effect of the dipoles becomes important when the ratio between the volume and the surface of the structure (viz. the lateral size of the cell) decreases. This assumption seems to be supported by the experiment presented in Figure 44 (Sect. 5.4.1): The hysteresis loop recorded at the corner of the cell having 1 μm in lateral size exhibits a significantly larger imprint compared to the hysteresis loop recorded at the center of the same cell. The proximity of the cell edges has therefore shifted the hysteresis loop in the negative direction. Eq. 38 gives for $P_D / P_{ferro} = 0.87$ in the case of cells having 100 nm size. This ratio decreases to only 0.033 for cells of 1 μm

* Although deduced for single crystals in the monodomain state, Eq. 10a still remains valid in the case of polycrystalline ferroelectrics (ceramics and films) if the values of the physical quantities involved are replaced with their effective values.

lateral size. It can also be found that the upper limit, $P_D = P_{ferro}$, is reached when the size of the structure decreases to zero.

In the case of PZT-based materials, the existence of these dipolar defects at the interfaces has been confirmed in different investigations, and therefore our explanation appears to be intuitively correct. However, further experiments, specifically on structures patterned on various p-type semiconductor substrates should confirm the opposite orientation of the dipolar defects compared to the present studies.

7. Conclusions and outlook

In this work a comprehensive study of the local piezoelectric response behavior of ferroelectric single crystals, thin films and nanostructures has been carried out, applying the technique of voltage-modulated scanning force microscopy. In view of the significance of ferroelectric thin films and nanostructures for the prospective development of high-density ferroelectric random access memories (FeRAMs) for use in advanced microelectronics, emphasis was put on the local ferroelectric properties of thin films and nanostructures of the most promising ferroelectric materials, viz. $\text{Pb}(\text{Zr,Ti})\text{O}_3$ (PZT) and different members of the bismuth-layer structure family (BLSF), or Aurivillius phases. Members of the Aurivillius family with both an even and an odd number n of perovskite-type octahedra between Bi_2O_2 layers (even Aurivillius parameter), viz. $\text{SrBi}_2\text{Ta}_2\text{O}_9$ (SBT) and $\text{BaBi}_4\text{Ti}_4\text{O}_{15}$, and $\text{Bi}_4\text{Ti}_3\text{O}_{12}$, respectively, have been studied, because these two sub-groups of the BSLF fundamentally differ in their crystal symmetry and therefore also in the anisotropy of their ferroelectric properties. The investigations included imaging ferroelectric domains, recording local piezoelectric hysteresis loops, and measuring piezoelectric coefficients, all with a lateral resolution down to 10 nm and a high sensitivity. This measurement performance has been achieved by adding a homemade piezoresponse module to a commercial scanning force microscope, by carefully optimizing the measuring procedures, and by studying some of the basic mechanisms and conditions underlying the piezoresponse-mode of scanning force microscopy. Among the results obtained, the following deserve particular attention either in terms of the possibilities and limitations of the piezoresponse-SFM technique, of new facts of fundamental character, or of formerly unknown properties of films and nanostructures significant to the future development of FeRAMs:

1. Making use of a simultaneous or subsequent visualization of both the out-of-plane and in-plane components of the piezoelectric response of a certain sample area, the ferroelectric domain structure of BaTiO_3 single crystals, known from many investigations of various authors, was fully reproduced using the piezoresponse-mode SFM setup. In this way, the overall performance and reliability of the setup and the validity of the measuring procedures used were fully confirmed.
2. The domain structure and local piezoelectric hysteresis loops of different grains in polycrystalline PZT thin films were studied and compared with each other. Film thickness and grain size of the films both ranged from 100 nm to 600 nm. The investigations showed that a strong variation of the properties occurred from grain to grain within the same film, and even within the same grain. In particular, it was found that the saturation piezoelectric coefficient may differ drastically from one grain to another, and that the switching process, viz. nucleation and growth of domains with reversed polarization, occurred differently when the same grain was probed at different places. The most probable reasons for this variability were found to be the different crystallographic orientations of the grains and crystallites implying variations of the effective piezoelectric response, and the fact that the switching nucleated by the SFM tip evolves according to the local environment. In view of the demonstrated spatial variation of the properties within polycrystalline films, the growth

of *epitaxial* films of these materials is necessary in order to achieve uniform properties over the entire film area.

3. Comprehensive investigations were carried out on individual grains of different well-defined crystallographic orientations within epitaxial thin films of different BSLF members, both with even and odd Aurivillius parameters n . In this way, it was confirmed that even- n BLSF members have no polarization component along their [001] axis, even not in the close vicinity of grains with other orientations, and that they cannot be polarized along the [001] axis under any local conditions. Accordingly, (001)-oriented films of even- n BSLF materials cannot be used in a planar-capacitor type FeRAM. In contrast, odd- n BLSF members have a small component of the polarization along their [001] axis, as was confirmed by local switching experiments in (001)-oriented regions of $\text{Bi}_4\text{Ti}_3\text{O}_{12}$ films. As a consequence, the odd- n BLSF members are in principle suitable for an application in a planar-type geometry even if they are (001)-oriented.
4. A study of the domain structure within individual grains was performed knowing the crystallographic directions in the investigated grains from comparative transmission electron microscopy (TEM) and selected area electron diffraction (SAED) studies of the same BLSF films. The main results are that small grains of the order of 100 nm in lateral size can possess a fine and stable domain structure with the domain sizes at the lateral resolution of the setup. Well defined, rectangular-shaped hysteresis loops were recorded from these grains indicating that individual ferroelectric structures with lateral sizes in the 100 nm range possess excellent properties for the application in non-volatile memories. It was found that the domain walls in these non- c -oriented grains are preferentially parallel to the c -axis and that, under certain circumstances, interaction of domain walls with different orientation caused the irreversible pinning of the adjacent domains. These results show that the domain sizes in thin films can attain much smaller values than believed previously and, therefore, the lower limit of the smallest structure still exhibiting ferroelectric behavior is well below 100 nm in case of BLSF materials.
5. For FeRAMs with a memory density in the Gigabit range, well-ordered ferroelectric nanostructures with lateral sizes in the 100 nm range are required. To find out whether or not such small structures are still ferroelectric (i.e. possess a spontaneous polarization that is switchable), a study of the local piezoresponse of such manufactured structures was performed. It was found that fine-grained $100\text{ nm} \times 100\text{ nm} \times 100\text{ nm}$ ferroelectric structures exhibit a well-defined piezoelectric hysteresis comparable to that of larger structures, up to $1\ \mu\text{m} \times 1\ \mu\text{m} \times 100\text{ nm}$. Since these structures were *separate* ferroelectric entities, the results clearly demonstrate that ferroelectricity scales well down with size, without deterioration of the switching behavior, at least in terms of the hysteresis loop parameters $2P_r$ and $2E_C$.
6. Switching experiments were performed on *individual* polycrystalline PZT structures $500\text{ nm} \times 500\text{ nm} \times 100\text{ nm}$ in size that were part of a regular array, with a spacing of 500 nm between them. The experiments showed that these structures could be addressed individually, that they switch entirely, i.e. different ferroelectric domains are not usually forming within one structure, and that no crosstalk occurs between neighboring structures.

Accordingly, there is no obstacle of physical nature to the realization of FeRAMs with a high memory density in the Gigabit range.

7. From the experimental piezoresponse results it was possible to derive certain components of the piezoelectric tensor of the ferroelectric epitaxial thin films investigated. Their values turned out to be about two to five times lower than the values measured macroscopically on the same materials, but comparable to the values obtained by other authors using piezoresponse SFM. The origins of the low values measured were discussed in terms of the complex electromechanical interaction between the ferroelectric sample and the probing SFM tip. For the case of bismuth titanate, which has a nonzero component of polarization along the c -axis, the ratio d_{11}/d_{33} determined was same as that measured macroscopically on single crystals, therefore validating the numerical values obtained from the piezoresponse data. A more complex model of the tip-to-sample interaction, including also the elastic properties of the tested material, is definitely needed in order to explain the small effective values measured.
8. A basic imaging mechanism has been studied taking into account the anisotropy of the tensor of the piezoelectric coefficients d_{ij} (matrix notation) in order to establish how the piezoresponse signal really reflects the out-of-plane component of the spontaneous polarization. It was found, by computing and drawing three-dimensional plots of the longitudinal piezoelectric coefficient d_{zz} along the probing direction that only in a restricted number of cases the magnitude of the piezoresponse signal correspond to the magnitude of the polarization.
9. The investigations also demonstrated a fundamental electrical asymmetry of the ferroelectric film-semiconductor electrode structure. The local piezoelectric hysteresis loops were always shifted in the vertical (d_{zz}) direction, indicating a preferential orientation of the polarization towards the bottom electrode. As the main reason, it was established that a region depleted from charge carriers is present at the interface between the ferroelectric film and the n -type SrTiO₃ substrate causing a built-in field, which favors the aforementioned polarization state. Moreover, it was observed, for the individual structures patterned on the same substrates, that this asymmetry increases with a decrease in size of the structure. The latter effect was explained assuming the presence of oriented dipolar defects in the fine-grained PZT cells, defects located mainly at the surface of the nanostructure.

In conclusion, the successful application of the piezoresponse-mode of scanning force microscopy to a variety of thin films and nanostructures of different composition, crystallographic structure and morphology has contributed to a better understanding of the piezoelectric and ferroelectric properties of these films and structures. Although a number of open questions remains, which are especially related to the details of the field distribution within the material volume under the SFM tip, it can be concluded that voltage-modulated scanning force microscopy has proven a powerful tool to characterize ferroelectric films and nanostructures on the lateral nanometer scale, a performance which is required for future developments of ferroelectric high-density memories in advanced microelectronics.

Appendices

Appendix A: The method of the image charges applied to EFM of a dielectric layer with bottom electrode

A ferroelectric sample with a bottom electrode and a conductive SFM tip represent an electrostatic system for which the potential distribution and the electric field have to be determined. In this section, the method of the image charges is used to estimate, in a first approximation, the potential distribution produced by the application of a voltage between the SFM tip and the bottom electrode.

In first approximation, the spontaneous polarization is neglected and the ferroelectric is replaced with a dielectric medium (further referred to as M2) having the permittivity ϵ_2 and a thickness d . Also, the conductive tip in contact with the dielectric is replaced with a point charge q_0 at a distance h above the surface in the adjacent medium (denominated M1) having the permittivity ϵ_1 . The bottom electrode, in contact with M2 on the opposite side of M1, is kept at zero potential. The solution of the simplified problem is based on the fact that the potential produced by q_0 has one equipotential surface which is tangential to the M1-M2 interface, and this surface may be considered as the surface of the tip.

For determining the potential inside the layer, the solution to two simple electrostatic problems turn out to be useful. The first one is the problem of a point charge located in M1 at a distance h from the plane that separates M1 from M2. This problem is further referred to as “DD” (“dielectric-dielectric”). The second elementary problem is that of a charge in front of an infinite conductive plane, from now on denominated “CP” (“conductive plane”). Both problems are solved in any basic course of electrostatics ^[181], and the respective solutions will be taken as known.

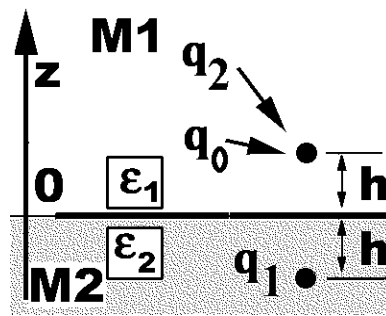


Figure A 1 Problem DD: A point charge in a medium M1 at a distance h of the surface that separates M1 and M2.

The solution of problem DD (the geometry of which is schematically represented in Figure A 1) is as follows: In M1 the potential is generated by two charges: a charge q_0 at $z = h$ in M1, and a charge q_1 at $z = -h$, in M2. In M2 the potential is given by a charge q_2 located in M1, at the same place as q_0 . The values of the charges q_1 and q_2 are :

$$\begin{cases} q_1 = -q_0 \frac{\epsilon_2 - \epsilon_1}{\epsilon_1 + \epsilon_2} \\ q_2 = q_0 \frac{2\epsilon_2}{\epsilon_1 + \epsilon_2} \end{cases} \quad \text{Eq. A 1}$$

The problem CP is trivial: the potential distribution of a system composed of a charge in front of a conductive plane is the same as the one of the initial charge plus a charge of opposite sign located symmetrically with respect to the plane.

For the initial problem, the origin of the axis z was chosen at the conductive plane, as shown in Figure A 2. The solution is based on successive imaging of charges with respect to the conductive plane and to the M1-M2 interface. The resolution of the problem can be performed following the succeeding steps:

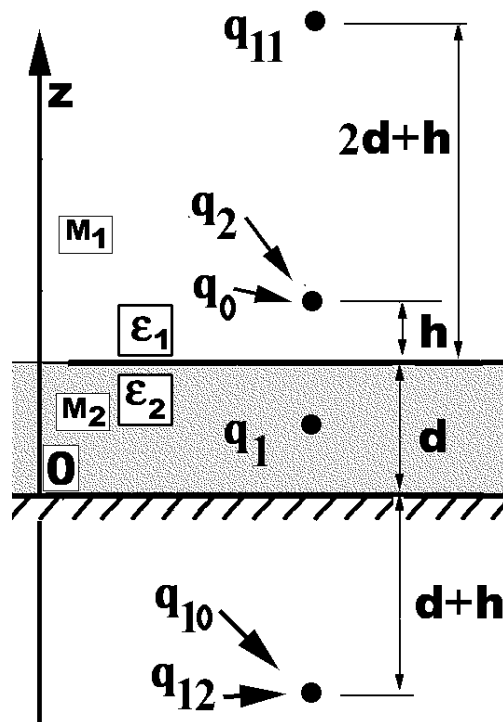


Figure A 2 Charges and their positions for the first two steps of the solution.

Step 1

The charge q_0 is imaged with respect to the dielectric interface (DD). In M1 the potential is given by q_0 , at position $z_0 = (d + h)$ and by q_1 (according to problem DD) at position $z_1 = (d - h)$ (the origin is now at the conductive plane). In M2, the potential is given by the charge q_2 (according to problem DD), at position $z_2 = (d + h)$. The solution of the problem DD ensured the fulfillment of the boundary condition at the M1–M2 interface. Since the conductive plane *exists* beneath M2, and since *in* M2 the potential is given by the charge q_2 (*only*, for now), it follows that q_2 has to be imaged with respect to the conductive plane. This third charge $q_{10} = -q_2$ is located at the position $z_{10} = -(d + h)$, symmetric to that of q_2 with respect to the conductive plane (Figure A 2).

The “occurrence” of the charge q_{10} contributes to the potential in M2 (according to the problem CP) and thus the boundary condition of DD ceases to be satisfied! Therefore, the

imaging process has to start again, now with the initial charge q_{10} instead of q_0 (that's why it was called q_{10} and not q_3 , for example).

Step 2

The new charge q_{10} (acting in M2, and which does not fulfill the boundary conditions of the previous solution of DD) is now the starting point of a new DD problem. The initial charge now being in M2 (and not in M1 as it was in the first DD problem), two other new charges are created. At this stage, the potential in M2 is given by the charges q_2 and q_{10} , and additionally, by the image charge q_{11} at position $z_{11} = d + (2d + h)$ (symmetric with respect to the dielectric interface). The potential in M1 is given, at this stage, by the charge q_{12} at position $z_{12} = -(d + h)$ (the same as q_{10} , according to the problem DD), in addition to the charges q_0 and q_1 (charges which were found previously that were acting in M1).

The values of the new charges are given in Eq. A 2 (the permittivities ϵ_1 and ϵ_2 of the solution DD in Eq. A 1 are interchanged, since now the initial charge is in M2).

$$\begin{cases} q_{10} = -q_2 = -q_0 \frac{2\epsilon_2}{\epsilon_1 + \epsilon_2} \\ q_{11} = -q_{10} \frac{\epsilon_1 - \epsilon_2}{\epsilon_1 + \epsilon_2} \\ q_{12} = q_{10} \frac{2\epsilon_1}{\epsilon_1 + \epsilon_2} \end{cases} \quad \text{Eq. A 2}$$

At this stage, the boundary conditions at the dielectric interface are fulfilled again, but with the new charge q_{11} acting in M2, the boundary condition at the conductive plane is not satisfied anymore, and this charge is the initial charge of a new CP problem. As a consequence, a new charge, $q_{20} = -q_{11}$, at $z_{20} = -(d + 3d + h)$, will contribute to the potential in M2, and the boundary conditions at the M1-M2 interface cease to be fulfilled.

Now the situation is the same as before in *Step 2*, with q_{20} being the starting charge. To find the complete solution, *Step 2* has to be repeated until the boundary conditions at the interfaces are fulfilled. It is important to note that no additional singularities are introduced by the imaging procedure: all the charges acting in M1 (M2) are located outside M1 (M2).

After performing the necessary calculations, the general formula for all image charges and their positions can be derived as given in Eq. A 3. The potential function is given in Eq. A 4. In these equations, k represents the number of *Step 2* iterative operations performed.

$$\begin{cases} q_0^k = (-1)^{2k-1} \left(\frac{\epsilon_1 - \epsilon_2}{\epsilon_1 + \epsilon_2} \right)^{k-1} \frac{2\epsilon_2}{\epsilon_1 + \epsilon_2} q_0 & , \quad z_0^k = -[(2k-1)d + h] \\ q_1^k = -\frac{\epsilon_1 - \epsilon_2}{\epsilon_1 + \epsilon_2} q_0^k & , \quad z_1^k = z_0^k \\ q_2^k = \frac{2\epsilon_1}{\epsilon_1 + \epsilon_2} q_0^k & , \quad z_2^k = (2k+1)d + h \end{cases} \quad \text{Eq. A 3}$$

$$\begin{cases} V_{M1} = V_0 + V_1 + \sum_{k=1} V_1^k \\ V_{M2} = V_2 + \sum_{k=1} (V_0^k + V_2^k) \end{cases} \quad \text{Eq. A 4}$$

In Eq. A 4, $V_\alpha^{(k)}$ is the potential produced by the charge $q_\alpha^{(k)}$, where $\alpha = 0, 1$, and 2. It is to be noted that the absolute values of the image charges are decreasing as k increases. Since the location of the charges is moving away from the interface with increasing k , the problem converges rather rapidly, depending on the ratio between the two permittivities. For example, if $\varepsilon_2/\varepsilon_1 \rightarrow \infty$ only the first step is needed and the electric field does not penetrate into M2. Usually, for $\varepsilon_2/\varepsilon_1 = 100$ (a usual case for ferroelectric thin films) $k = 5$ iterations are needed to fulfill the boundary conditions with an accuracy of 1%.

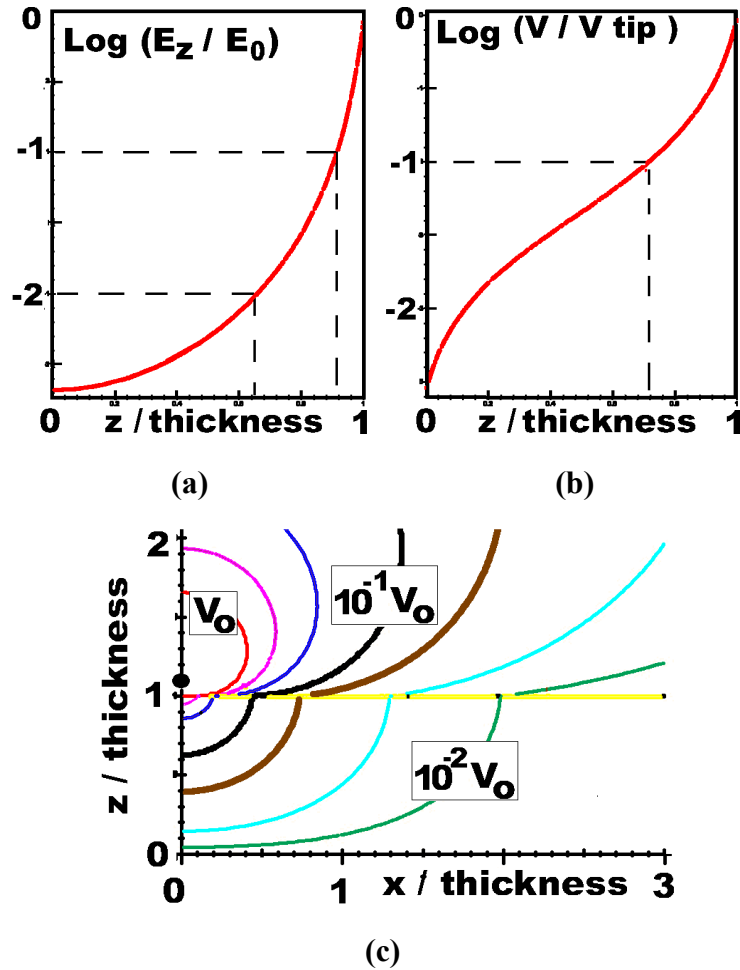


Figure A 3 (a, b) Electric field (a) and potential (b) versus position along the film thickness directly under the tip. (c) Cross-section normal to the film plane showing the equipotential surfaces. V_0 denotes the equipotential tangent to the surface, that may play the role of the tip surface (i.e. the voltage applied to the tip with respect to the bottom electrode). The distances in the plots are divided by the film thickness. Note: the accuracy is better than 1% (the potential at the bottom electrode is not zero, but less than 1% of the value at the surface).

The results of the calculations of the electric field and of the potential in the regions of interest for $\varepsilon_2/\varepsilon_1 = 100$ are shown in Figure A 3. As expected, both the electric field and the potential inside the dielectric are extremely inhomogeneous and concentrated under the tip apex. The plot in Figure A 3a shows that the electric field at a depth of 35% of the

dielectric thickness under the surface is about 1% of the value at the contact place, and is ten times smaller than at a depth of 10% of the dielectric thickness. The potential plot in Figure A 3b shows that the voltage drop over the first 30% of thickness of the dielectric is almost 90% of the voltage applied to the tip.

Figure A 3c illustrates the equipotential surfaces in a cross-section through the $y = 0$ plane. Both x - and z -axes were scaled to the film thickness, so that the $z = 0$ plane represents the dielectric-bottom electrode interface, whereas the sample surface is at $z = 1$. The presence of a field component parallel to the sample surface, in the near vicinity of the tip should be especially emphasized. This in-plane component may polarize the ferroelectric along radial directions parallel to the film surface. Whether or not the resulting domain structure is stable, depends on the material and on the local environment.

Appendix B: Dependence of the piezoelectric coefficients on the testing directions

In piezoresponse SFM, the tip senses the induced oscillations in a ferroelectric sample. If the spontaneous polarization is normal to the film plane, then the piezoelectric coefficient involved is the standard one. For example, if the sample probed is c -oriented PZT, the piezoelectric coefficient detected is d_{33} . This section addresses the problem of the piezoelectric detection if the ferroelectric has an arbitrary orientation.

Given (d^0) the complete set of piezoelectric coefficients for a particular orientation of the coordinates system $S^0 = (x^0, y^0, z^0) = (x^0_i)$ with respect to the principal crystallographic axes, the piezoelectric coefficients along different directions can be calculated using tensor transformations^[6,7,182]. For this purpose, a second system of coordinates $S = (x, y, z) = (x_i)$ has to be chosen, in such a way that the directions of interest are along its axes. For example, if only the longitudinal coefficient has to be calculated along a particular direction, then the system S is chosen with one of its axis (usually the z -axis) to coincide in orientation with the direction of interest. In this case, the x - and y - axes may have arbitrary orientations, since only the z -direction is implied in the measurement (both the electric field and the induced displacement are along z). The choice of the system of axes has also to fulfill the condition of being a right-handed orthogonal system. Now the piezoelectric coefficient related to the directions of interest can be computed in the new system of coordinates from the *whole piezoelectric tensor* in the system S^0 . For instance, in the aforementioned case, the piezoelectric coefficient d_{33} in the system S is the longitudinal piezoelectric coefficient (d_{zz}) along the direction z in the system S_0 .

The transformation matrix of coordinates from the system S^0 to the system S is $A'_i = a_{ij} = x_i x_j$. The components of the piezoelectric tensor will then transform from the old system to the new one as $d_{ijk} = A_i^m A_j^n A_k^l d_{mnl}^0$. For the compressed (matrix) notation of the coefficients, this transformation become:

$$d = A d^0 N, \tag{Eq. A 5}$$

where the elements of matrix N are combinations of the elements of the matrix A ^[7]:

$$N = \begin{bmatrix} a_{11}^2 & a_{12}^2 & a_{13}^2 & a_{12}a_{13} & a_{11}a_{13} & a_{11}a_{12} \\ a_{21}^2 & a_{22}^2 & a_{23}^2 & a_{22}a_{23} & a_{21}a_{23} & a_{21}a_{22} \\ a_{31}^2 & a_{32}^2 & a_{33}^2 & a_{32}a_{33} & a_{31}a_{33} & a_{31}a_{32} \\ 2a_{21}a_{31} & 2a_{22}a_{32} & 2a_{23}a_{33} & a_{22}a_{33}+a_{23}a_{32} & a_{21}a_{33}+a_{23}a_{31} & a_{21}a_{32}+a_{22}a_{31} \\ 2a_{11}a_{31} & 2a_{12}a_{32} & 2a_{13}a_{33} & a_{12}a_{33}+a_{13}a_{32} & a_{11}a_{33}+a_{13}a_{31} & a_{11}a_{32}+a_{12}a_{31} \\ 2a_{11}a_{21} & 2a_{12}a_{22} & 2a_{13}a_{23} & a_{12}a_{23}+a_{13}a_{22} & a_{11}a_{23}+a_{13}a_{21} & a_{11}a_{22}+a_{12}a_{21} \end{bmatrix} \quad \text{Eq. A 6}$$

To calculate the longitudinal piezoelectric coefficient along different directions, the new system $S = (x_i) = (x, y, z)$ is rotated in the 3-dimensional space and the d_{zz} coefficient is calculated using Eq. A 5. The system $S^0 = (x_i^0) = (x^0, y^0, z^0)$ is chosen with its axes to coincide with the crystallographic ones for which (d^0) is known (for instance $[001]$ is x^0_3 , $[100]$ is x^0_1 , $[010]$ is x^0_2). A convenient transformation matrix that can be used to rotate the system S in 3-dimensional space with respect to the system S_0 is the following:

$$A = \begin{bmatrix} \sin \varphi & -\cos \varphi & 0 \\ \cos \theta \cos \varphi & \cos \theta \sin \varphi & -\sin \theta \\ \sin \theta \cos \varphi & \sin \theta \sin \varphi & \cos \theta \end{bmatrix}$$

where θ is the angle between the axis z^0 and the axis z , and φ is the angle between the projection of the z -axis on the x^0y^0 plane and the x^0 -axis. The transformation matrix A rotates all the three x, y, z -axes but the x -axis is kept in the x^0y^0 plane. The two systems coincide for $\theta = 0^\circ$ and $\varphi = 90^\circ$.

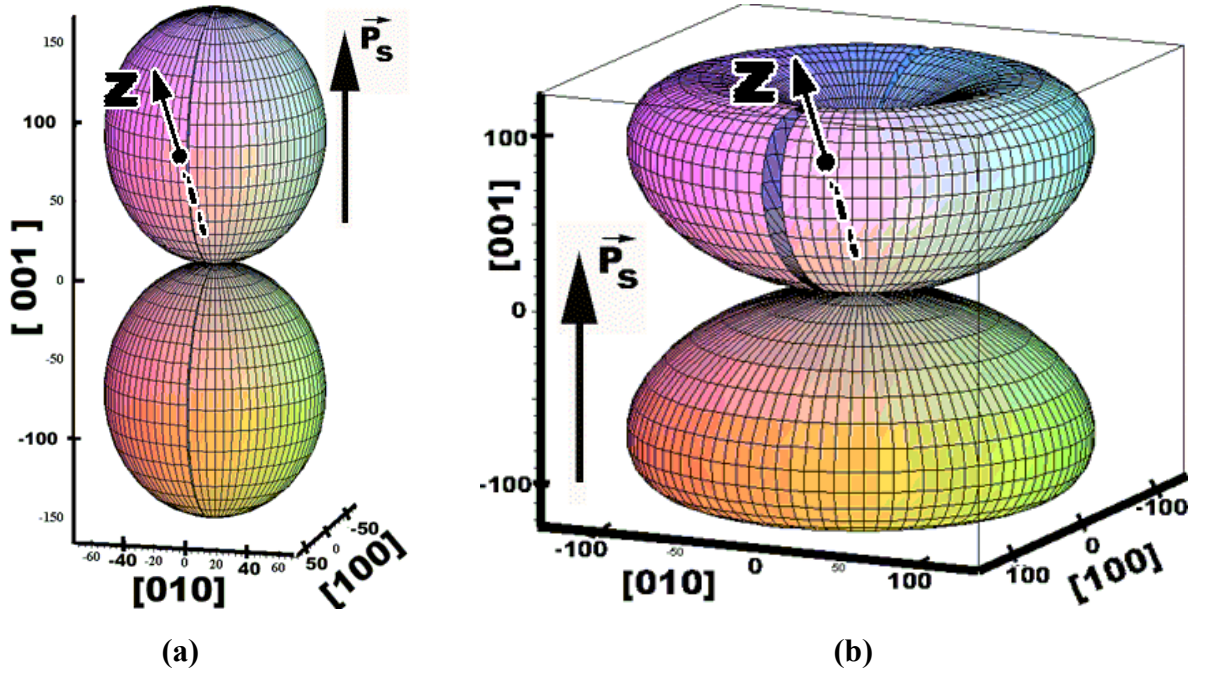


Figure A 4 Longitudinal piezoelectric coefficient d_{zz} (electric field applied along z , displacement measured along z) for the tetragonal symmetry $4mm$: **(a)** for PZT(40/60), and **(b)** for BaTiO₃. Numerical values used for the calculation are given in Table 2. For the specific meaning of the surface plot see text.

The results of the calculation are shown in Figure A 4 for tetragonal PZT (a) and for tetragonal BaTiO₃ (b). In these figures, the distance between one point of the graph and the origin represents the longitudinal piezoelectric coefficient along that direction.

Therefore, if the longitudinal piezoelectric coefficient is not measured along the direction of the spontaneous polarization, the piezoelectric coefficient is not simply proportional to the projection of the polarization on this direction, but is a complicated function of the other piezoelectric coefficients of the entire piezoelectric tensor.*

By replacing (d^0) in Eq. A 5 with the piezoelectric matrix form of tetragonal single crystals (point group 4mm) the general equation given in Eq. A 7 comes out for the longitudinal piezoelectric coefficient along a direction making the angle θ with the direction of the spontaneous polarization.

$$d_{zz}(\theta) = (d_{31} + d_{15})\sin^2 \theta \cos \theta + d_{33} \cos^3 \theta \quad \text{Eq. A 7}$$

In Eq. A 7 there are two terms that influence d_{zz} . The two materials chosen (Figure A 4) represent the extreme cases for which one of the two terms dominates and determines the shape of the surface: d_{33} in the case of PZT and d_{15} for BaTiO₃.

Material (point group)	d_{22} (pm/V)	d_{33} (pm/V)	d_{31} (pm/V)	d_{15} (pm/V)
BaTiO ₃ (4mm)	-	85	-35	400
PZT (40/60) (4mm)	-	160	-60	170
PZT (60/40) (3m)	75	70	-11	360

Table 2 The piezoelectric coefficients used for the graphic representation (in the standard orientation for each symmetry).

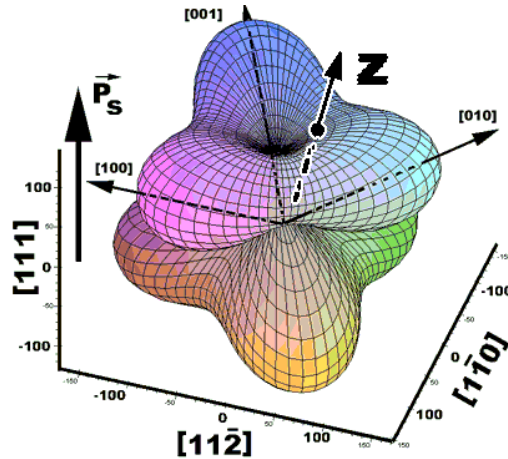


Figure A 5 d_{zz} of rhombohedral PZT. Note that in this case the magnitude of d_{zz} does not reflect anymore the maximum of the z -component of the polarization.

* for instance, $d_{zz} \neq d_{33} \cos \theta$, where θ is the angle between the directions “ z ” and “ 3 ”.

For lower symmetries, the dependence of the piezoelectric coefficient on the direction is more complex, since there will be more non-zero terms than in Eq. A 7. For example, in Figure A 5 the piezoelectric surface for rhombohedral PZT is given. One can easily notice that the d_{zz} piezoelectric coefficient is not anymore simply related to the component of the spontaneous polarization along the z -direction. In such cases, the analysis of the piezoresponse is becoming complex and the images or the local measurements have to be considered with extreme care.

Appendix C: The effective piezoelectric coefficients in thin films – clamping by the substrate

It is well known that piezoelectric measurements of thin films reveal much lower values of the coefficients, compared to the bulk values in standard measurements. This effect has been assigned to the *clamping* of the piezoelectric film by the substrate. The origin of this effect comes from the fact that the longitudinal piezoelectric effect occurs always together with the transversal effect. For the inverse piezoelectric effect, for example, the application of an electric field parallel to P_S does not only cause an extension ($d_{33} > 0$) in the direction parallel to the field, but also a compression perpendicular to the field (d_{31} has almost always a sign opposite to that of d_{33}). If the crystal is not allowed to deform along the transversal directions, then it will deform less along the longitudinal (normal to the film) direction. In the case of thin films on substrates, exactly this is happening, and the direct consequence is that the value of the measured piezoelectric coefficient is much lower than the real one^[183].

In the case of the converse piezoelectric effect, the effective piezoelectric coefficient may be easily calculated by using the piezoelectric constitutive equations (Eq. 5a in Sect. 2.2).

In the case of a polycrystalline film poled in the z -direction perpendicular to the film plane, the symmetry class in this case is the same as that for a poled ceramic, i.e. ∞mm . The relevant equations in this case are:

$$D_3 = \epsilon_{33}E_3 + d_{31}(X_1 + X_2) + d_{33}X_3 \quad \text{Eq. A 8}$$

$$\begin{cases} x_1 = s_{11}^E X_1 + s_{12}^E X_2 + s_{13}^E X_3 + d_{31}E_3 \\ x_2 = s_{11}^E X_2 + s_{12}^E X_1 + s_{13}^E X_3 + d_{31}E_3 \\ x_3 = s_{13}^E (X_1 + X_2) + s_{33}^E X_3 + d_{33}E_3 \end{cases} \quad \text{Eq. A 9}$$

An ideal clamping in the x - y plane (plane of the substrate) implies $x_1 = x_2 = 0$ whereas $x_3 \neq 0$. The symmetry of the film in the plane of the substrate results in $X_1 = X_2$ and because the surface of the film is free, $X_3 = 0$. Eq. A 9 then gives for the effective (measured) converse piezoelectric coefficient in randomly oriented films:

$$d_{33}^{clamped} = \frac{x_3}{E_3} = d_{33} - 2d_{31} \frac{s_{13}^E}{s_{11}^E + s_{12}^E} \quad \text{Eq. A 10}$$

Since in most materials $d_{31} < 0$ and $s_{13} < 0$, the measured coefficient in films is smaller than in unclamped materials. Therefore, the small values of the piezoelectric coefficients in films relative to the bulk ceramic values can be at least partly explained by the clamping effects of the substrate.

Appendix D: The matrix notation of the electromechanical coefficients

To simplify the notation, the components of the electromechanical tensors (strain, stress, elastic compliance, piezoelectric coefficient, electrostriction, etc) can be written in the matrix (or reduced notation) form, following the Voigt convention given in Table 3. A pair of indices $ii = 11, 22, 33$, for example, is replaced with the single index $m = 1, 2, 3$, respectively, and the mixed pairs of indices (which represent shear components of strain and stress tensors) $ij = 23$ or $32, 13$ or $31, 12$ or 21 are written as $m = 4, 5, 6$, respectively.

Tensor notation	Matrix notation
$ii = 11, 22, 33$	$m = 1, 2, 3$
$ij = 23$ or $32, 13$ or $31, 12$ or 21	$m = 4, 5, 6$
s_{ijkl}	s_{mn} , both m and $n = 1, 2$ or 3
$2 s_{ijkl}$	s_{mn} , m or $n = 4, 5$, or 6
$4 s_{ijkl}$	s_{mn} , both m and $n = 4, 5$, or 6
d_{ijk}	d_{im} , $m = 1, 2, 3$
d_{ijk}	$(1/2)d_{im}$, $m = 4, 5, 6$
Q_{ijkl}	Q_{ijkl} , $m = 1, \dots, 6, n = 1, 2, 3$
$2 Q_{ijkl}$	Q_{ijkl} , $m = 1, \dots, 6, n = 4, 5, 6$

Table 3 Conventions for the matrix notation

References

- ¹ K. Aizu, *Phys. Rev.* **146**, 423 (1966).
- ² J. Fousek and V. Janovec, *J. Appl. Phys.* **40**, 135 (1969).
- ³ L.E. Cross, *Thermodynamic phenomenology of ferroelectricity in single crystal and ceramic systems*. In: *Physics of Electronic Ceramics*, Part B. Eds.: L.L. Hench and D.B. Dove. Dekker, New York 1972, p.707.
- ⁴ T. Mitsui, I. Tatsuzaki, and E. Nakamura, *An Introduction to the Physics of Ferroelectrics*. Gordon and Breach, London 1976.
- ⁵ M.E. Lines and A.M. Glass, *Principles and Applications of Ferroelectrics and Related Materials*. Clarendon Press, Oxford 1977.
- ⁶ J.F. Nye, *Physical Properties of Crystals*. Oxford University Press, Oxford 1985.
- ⁷ W.G. Cady, *Piezoelectricity*. Dover Publications, Inc., New York 1964.
- ⁸ D. Damjanovic, *Rep. Prog. Phys.* **61**, 1267 (1998).
- ⁹ IRE Standards on piezoelectric crystals, 1949 (49 IRE 14.S1), *Proc. IRE* vol. 47, 1378-1395 (Dec. 1949).
- ¹⁰ A.F. Devonshire, *Philos. Mag.* **42**, 1065 (1951). See also A.F. Devonshire, *Philos. Mag.* **40**, 1040 (1949).
- ¹¹ R. Wiesendanger, *Scanning Probe Microscopy and Spectroscopy: Methods and Applications*. University Press, Cambridge 1994, p.291.
- ¹² Th. Schimmel, Th. Koch, J. Küppers, and M. Lux-Steiner, *Appl. Phys. A* **68**, 399 (1999).
- ¹³ L.M. Eng, M. Bammerlin, Ch. Loppacher, M. Guggisberg, R. Bennewitz, R. Lüthi, E. Meyer, and H.-J. Güntherodt, *Appl. Surf. Sci.* **140**, 253 (1999).
- ¹⁴ N. Nakatani, *Jpn. J. Appl. Phys.* **18**, 491 (1979).
- ¹⁵ H. Bluhm, U.D. Schwarz, K.-P. Meyer, and R. Wiesendanger, *Appl. Phys. A* **61**, 525 (1995).
- ¹⁶ H. Bluhm, R. Wiesendanger and K.-P. Meyer, *J. Vac. Sci. Technol. B* **14**, 1180 (1996).
- ¹⁷ A. Savada and R. Abe, *Jpn. J. Appl. Phys.* **6**, 699 (1967).
- ¹⁸ L.M. Eng, H.J. Güntherodt, G. Rosenman, A. Skliar, M. Oron, M. Katz, and D. Eger, *J. Appl. Phys.* **83**, 5973 (1998).
- ¹⁹ R. Lüthi, H. Haefke, W. Gutmannsbauer, E. Meyer, L. Howald, and H.-J. Güntherodt, *J. Vac. Sci. Technol. B* **12**, 2451 (1994).
- ²⁰ L.M. Eng, M. Friedrich, J. Fousek, and P. Günter, *J. Vac. Sci. Technol. B* **14**, 1191 (1996).
- ²¹ A. Correia, J. Massanell, N. Garcia, A.P. Levanyuk, A. Zlatkin, and J. Przeslawski, *Appl. Phys. Lett.* **68**, 2796 (1996).
- ²² D.-Y. Kim, J.W. Hong, S.-I. Kwun, and S.-Y. Jeong, *J. Vac. Sci. Technol. B* **16**, 2125 (1998).
- ²³ S.-I. Hamazaki, F. Shimizu, S. Kojima, and M. Takashige, *J. Phys. Soc. Jpn.* **64**, 3660 (1995).
- ²⁴ S. Tsunekawa, T. Fukuda, T. Ozaki, Y. Yoneda, T. Okabe, and H. Terauchi, *J. Appl. Phys.* **84**, 999 (1998).
- ²⁵ S. Balakumar, J.B. Xu, J.X. Ma, S. Ganesamoorthy, and I.H. Wilson, *Jpn. J. Appl. Phys.* **36**, 5566 (1997).
- ²⁶ M. Takashige, S.-I. Hamazaki, N. Fukurai, and F. Shimizu, *J. Phys. Soc. Jpn.* **66**, 1848 (1997).
- ²⁷ Y.G. Wang, J. Dec, and W. Kleeman, *J. Appl. Phys.* **84**, 6795 (1998).

- ²⁸ M. Takashige, S.-I. Hamazaki, N. Tashiro, F. Shimizu, and M.S. Jang, *Jpn. J. Appl. Phys.* **37**, 5397 (1998).
- ²⁹ A. Gruverman, O. Auciello, and H. Tokumoto, *Integr. Ferroelectr.* **19**, 49 (1998).
- ³⁰ O. Kolosov, A. Gruverman, J. Hatano, K. Takahashi, and H. Tokumoto, *Phys. Rev. Lett.* **74**, 4309 (1995).
- ³¹ A. Gruverman, O. Kolosov, J. Hatano, K. Takahashi, and H. Tokumoto, *J. Vac. Sci. Technol. B* **13**, 1095 (1995).
- ³² M. Takashige, S.-I. Hamazaki, N. Fukurai, N. Tashiro, F. Shimizu, and S. Kojima, *J. Phys. Soc. Jpn.* **66**, 2272 (1997).
- ³³ R. Lüthi, H. Haefke, K.-P. Meyer, E. Meyer, L. Howald, and H.-J. Güntherodt, *J. Appl. Phys.* **74**, 7461 (1993).
- ³⁴ H. Bluhm, U.D. Schwarz, and R. Wiesendanger, *Phys. Rev. B* **57**, 161 (1998).
- ³⁵ R. Lüthi, H. Haefke, P. Grütter, H.-J. Güntherodt, L. Szczesniak, and K.-P. Meyer, *Surf. Sci. Lett.* **285**, L498 (1993).
- ³⁶ S. Kim, Y. Park, Y. Kang, W. Park, S. Baik, and A.L. Gruverman, *Thin Solid Films* **312**, 249 (1998).
- ³⁷ D. Rugar, H.J. Mamin, P. Güthner, S.E. Lambert, J.E. Stern, I. McFadyen, and T. Yogi, *J. Appl. Phys.* **68**, 1169 (1990).
- ³⁸ J.E. Stern, B.D. Terris, H.J. Mamin, and D. Rugar, *Appl. Phys. Lett.* **53**, 2717 (1988); B.D. Terris, J.E. Stern, D. Rugar, and H.J. Mamin, *J. Vac. Sci. Technol. A* **8**, 374 (1990); B.D. Terris, J.E. Stern, D. Rugar, H.J. Mamin, *Phys. Rev. Lett.* **63**, 2669 (1989).
- ³⁹ F. Saurenbach and B.D. Terris, *Appl. Phys. Lett.* **56**, 1703 (1990).
- ⁴⁰ C.H. Ahn, T. Tybell, L. Antognazza, K. Char, R.H. Hammond, M.R. Beasley, Ø. Fischer, J.-M. Triscone, *Science* **276**, 1100 (1997).
- ⁴¹ M. Nonnenmacher, M.P. O'Boyle, and H.K. Wickramasinghe, *Appl. Phys. Lett.* **58**, 2921 (1991).
- ⁴² D. Sarid, *Scanning Force Microscopy with Applications to Electric, Magnetic and Atomic Forces*, Oxford University Press, New York 1991.
- ⁴³ Ch. Sommerhalter, Th.W. Matthes, Th. Glatzel, A. Jäger-Waldau, and M.Ch. Lux-Steiner, *Appl. Phys. Lett.* **75**, 286 (1999).
- ⁴⁴ H. Birk, J. Glatz-Reichenbach, Li Jie, E. Schreck, and K. Dransfeld, *J. Vac. Sci. Technol. B* **9**, pt.2, 1162 (1991).
- ⁴⁵ P. Güthner, and K. Dransfeld, *Appl. Phys. Lett.* **61**, 1137 (1992).
- ⁴⁶ K. Franke, J. Besold, W. Haessler, and C. Seegebarth, *Surf. Sci. Lett.* **302**, L283 (1994).
- ⁴⁷ K. Franke and M. Weihnacht, *Ferroelectric Lett.* **19**, 25 (1995).
- ⁴⁸ K. Franke, *Ferroelectric Lett.* **19**, 35 (1995).
- ⁴⁹ T. Hidaka, T. Maruyama, M. Saitoh, N. Mikoshiba, M. Shimizu, T. Shiosaki, L.A. Wills, R. Hiskes, S.A. Dicarolis, and J. Amano, *Appl. Phys. Lett.* **68**, 2358 (1996).
- ⁵⁰ A. Gruverman, O. Auciello, and H. Tokumoto, *Appl. Phys. Lett.* **69**, 3191 (1996).
- ⁵¹ A. Gruverman, H. Tokumoto, S.A. Prakash, S. Aggarwal, B. Yang, M. Wuttig, R. Ramesh, O. Auciello, and T. Venkatesan, *Appl. Phys. Lett.* **71**, 3492 (1997).
- ⁵² L.M. Eng, H.J. Güntherodt, G. Rosenman, A. Skliar, M. Oron, M. Katz, and D. Eger, *J. Appl. Phys.* **83** (11) 5973 (1998).
- ⁵³ L.M. Eng, M. Abplanalp, and P. Günter, *Appl. Phys. A* **66**, S679 (1998).
- ⁵⁴ V. Likodimos, X.K. Orlik, L. Pardi, M. Labardi, and M. Allegrini, *J. Appl. Phys.* **87**, 443 (2000).
- ⁵⁵ M. Abplanalp, L.M. Eng, and P. Günter, *Appl. Phys. A-Mater* **66**, S231 (1998).

- ⁵⁶ L.M. Eng, H.J. Güntherodt, G.A. Schneider, U. Köpke, and J. Munoz Saldana, *Appl. Phys. Lett.* **74**, 233 (1999).
- ⁵⁷ A. Gruverman and Y. Ikeda, *Jpn. J. Appl. Phys.* **37**, L939 (1998).
- ⁵⁸ C. Harnagea, A. Pignolet, M. Alexe, K.M. Satyalakshmi, D. Hesse, and U. Gösele, *Jpn. J. Appl. Phys.* **38**, L1255 (1999).
- ⁵⁹ M. Alexe, A. Gruvermann, C. Harnagea, N.D. Zakharov, A. Pignolet, D. Hesse and J.F. Scott, *Appl. Phys. Lett.* **75**, 1158 (1999).
- ⁶⁰ C. Harnagea, M. Alexe, A. Pignolet, K.M. Satyalakshmi, D. Hesse and U. Gösele: "Switching of ferroelectric nanostructures". In: *Piezoelectric Materials: Advances in Science, Technology and Applications*. Eds: C.Galassi, M.Dinescu, K.Uchino, and M.Sayer. NATO Science Series No.3 - High Technology, vol. 76, Kluwer Academic Publishers, Dordrecht, Boston, London 2000, p.169.
- ⁶¹ A.L. Kholkin, C. Wüthrich, D.V. Taylor, and N. Setter, *Rev. Sci. Instrum.* **67**, 1935 (1996).
- ⁶² L.N. Kantorovich, A.I. Livshits, and M. Stoneham, *J. Phys.: Condens. Matter* **12**, 795 (2000).
- ⁶³ J.W. Hong, Sang-il Park, and Z.G. Khim, *Rev. Sci. Instrum.* **70**, 1735 (1999).
- ⁶⁴ Ch. Sommerhalter, Th. Glatzel, Th.W. Matthes, A. Jäger-Waldau, and M.Ch. Lux-Steiner, *Appl. Surf. Sci.* **157**, 263 (2000).
- ⁶⁵ H.O. Jacobs, P. Leuchtmann, O.J. Homan, and A. Stemmer, *J. Appl. Phys.* **84**, 1168 (1998).
- ⁶⁶ C. Durkan, M.E. Welland, D.P. Chu, and P. Migliorato, *Phys. Rev. B* **60**, 16198 (1999).
- ⁶⁷ K. Goto and K. Hane, *J. Appl. Phys.* **84**, 4043 (1998).
- ⁶⁸ W.K.H. Panofsky and M. Phillips, *Classical Electricity and Magnetism*, 2nd ed. Addison-Wesley Reading, MA 1962, Chap.3; K.J. Binns and P.J. Lawrenson, *Analysis and Computation of Electric and Magnetic Field Problems*, 2nd ed. Pergamon, Oxford, 1973, Chap. 3.
- ⁶⁹ S. Belaidi, P. Girard, and G. Leveque, *J. Appl. Phys.* **81**, 1023 (1997).
- ⁷⁰ S. Lanyi, J. Torok, and P. Rehurek, *J. Vac. Sci. & Technol. B.* **14**, 892, (1996).
- ⁷¹ Dimension™ 5000 Scanning Probe Microscope Instruction Manual, Digital Instruments, Incorporated, Santa Barbara, California (1994).
- ⁷² Model 7260 DSP Lock-in Amplifier Instruction Manual (190 163-A-MNL-D), EG&G Instruments Corporation (1997).
- ⁷³ C. Harnagea, A. Pignolet, M. Alexe, D. Hesse, and U.Gösele, *Appl.Phys. A* **70**, 261 (2000).
- ⁷⁴ Keithley Model 6517 Electrometer User's Manual (Document No.: 6517-900-01 Rev. D), Keithley Instruments, Inc. Test Instrumentation Group, Cleveland, Ohio, USA, Fourth Printing, July 1995.
- ⁷⁵ As it is well known, the cantilever spring constant determines the mechanical resonance and the contact force between tip and sample.
- ⁷⁶ J.A. Christman, R.R. Woolcott Jr., A.I. Kingon, R.J. Nemanich, *Appl. Phys. Lett.* **73**, 3851 (1998).
- ⁷⁷ A. Pignolet, M. Alexe, K.M. Satyalakshmi, S. Senz, D. Hesse, and U. Gösele, *Ferroelectrics* **225**, 201 (1999).
- ⁷⁸ A. Pignolet, C. Curran, M. Alexe, N.D. Zakharov, D. Hesse, and U. Gösele, *Integr. Ferroelectr.* **21**, 485 (1998).
- ⁷⁹ A. Pignolet, C. Schäfer, K.M. Satyalakshmi, C. Harnagea, D. Hesse, and U. Gösele, *Appl.Phys. A* **70**, 283 (2000).
- ⁸⁰ M. Alexe, C. Harnagea, D. Hesse, and U. Gösele, *Appl. Phys. Lett.* **75**, 1793 (1999).
- ⁸¹ H.G. Craighead and L.M. Schiavone, *Appl. Phys. Lett.* **48**, 1748 (1986).
- ⁸² R.E. Jones, *Semicond. Sci. Technol.* **40**, 201 (1997).
- ⁸³ S. Okamura, K. Mori, T. Tsukamoto, and T. Shiosaki, *Integr. Ferroelectr.* **18**, 311 (1997).

- ⁸⁴ J. Lohau, S. Friedrichowski, G. Dumpich, E.F. Wassermann, M. Winter, and T.A. Reetz, *J. Vac. Sci. Technol. B* **16**, 77 (1998).
- ⁸⁵ L.M. Eng, M. Abplanalp, P. Günter, and H.-J. Güntherodt, *J. de Physique IV* **8**, 201 (1998).
- ⁸⁶ C. Harnagea et al., in preparation.
- ⁸⁷ G. Sorge and H. Beige, *Experimentelle Technik der Physik* **23**, 489 (1975).
- ⁸⁸ H. Beige, G. Sorge, G. Schmidt, and M. Glogarova, *Experimentelle Technik der Physik* **26**, 297 (1978).
- ⁸⁹ A.L. Kholkin, E.L. Colla, A.K. Tagantsev, D.V. Taylor, and N. Setter, *Appl. Phys. Lett.* **68**, 2577 (1996).
- ⁹⁰ G. Zavala, J.H. Fendler, and S. Trolrier-McKinstry, *J. Appl. Phys.* **81**, 7480 (1997).
- ⁹¹ C. Alemany, R. Jimenez, J. Revilla, J. Mendiola, and M.L. Calzada, *J. Phys. D: Appl. Phys.* **32**, L79 (1999).
- ⁹² S. Nomura and K. Uchino, *Ferroelectrics* **41**, 117 (1982); K. Uchino, S. Nomura, L.E. Cross, S.J. Jang, and R.E. Newnham, *J. Appl. Phys.* **51**, 1142 (1980), for bulk PMN-based compounds.
- ⁹³ A. Kholkin, C. Tantigate, and A. Safari, *Integr. Ferroelectr.* **22**, 515 (1998).
- ⁹⁴ A.L. Kholkin, K.G. Brooks, and N. Setter, *Appl. Phys. Lett.* **71**, 2044 (1998).
- ⁹⁵ V. Bobnar, Z. Kutnjak, A. Levstik, J. Holc, M. Kosec, T. Hauke, R. Steinhausen, and H. Beige, *J. Appl. Phys.* **85**, 622 (1999).
- ⁹⁶ K. Takata, H. Miki, K. Torii, K. Kushida-Abdelghafar, and Y. Fujisaki, *Appl. Phys. Lett.* **75**, 3126, (1999).
- ⁹⁷ K. Uchino, *Ferroelectric devices*, Marcel Dekker Inc., New York – Basel 2000.
- ⁹⁸ A. von Hippel et. al., NDRC Rep No 300 (1944), cited by: A. von Hippel, *Rev. Mod. Phys.* **22**, 221 (1950).
- ⁹⁹ B. Wul, *Nature* **156**, 480 (1945); B. Wul and I.M. Goldman, *Compt. rend. Acad. Sci. URSS* **46**, 139 (1946).
- ¹⁰⁰ J.P. Remeika, *J. Am. Chem. Soc.* **76**, 940 (1954).
- ¹⁰¹ C.B. Sawyer and C.H. Tower, *Phys. Rev.* **35**, 269 (1930).
- ¹⁰² Landolt-Börnstein: *Numerical Data and Functional Relationships in Science and Technology*, Group III, Vol. **16**, subvol. A. Springer Berlin, Heidelberg, New York 1981.
- ¹⁰³ L.M. Eng, D. Hesse, and A. Pignolet, private communication. The phenomenon of Figure 18a is well known as “watermarks”.
- ¹⁰⁴ L.M. Eng, *Nanotechnology* **10**, 405 (1999).
- ¹⁰⁵ J.W. Hong, Sang-il Park, and Z.G. Khim, *Rev. Sci. Instrum.* **70**, 1735 (1999).
- ¹⁰⁶ D.M. Taylor, *Thin Solid Films* **331**, 1 (1998).
- ¹⁰⁷ H. Maiwa, J.P. Maria, J.A. Christman, S.H. Kim, K. Streiffer, and A.I. Kingon, *Integr. Ferroelectr.* **24**, 139 (1999).
- ¹⁰⁸ H. Maiwa, J.A. Christman, S.-H. Kim, D.-J. Kim, J.-P. Maria, B. Chen, S.K. Streiffer and A.I. Kingon, *Jpn. J. Appl. Phys.* **38**, Part 1, 5402 (1999).
- ¹⁰⁹ W.L. Warren, D. Dimos, G.E. Pike, B.A. Tuttle, and M.V. Raymond, R. Ramesh, and J.T. Evans Jr., *Appl. Phys. Lett.* **67**, 866 (1995).
- ¹¹⁰ M. Grossmann, D. Bolten, O. Lohse, U. Boettger, R. Waser, and S. Tiedke, *Appl. Phys. Lett.* **77**, 1894 (2000).
- ¹¹¹ C. Durkan, D.P. Chu, P. Migliorato, and M.E. Welland, *Appl. Phys. Lett.* **76**, 366 (2000).
- ¹¹² R. Steinhausen, T. Hauke, W. Seifert, V. Müller, H. Beige, S. Seifert, and P. Lobmann, *Proc. 11th IEEE-ISAF (Montreux, Aug. 24-27, 1998)*, Cat. No.98CH36245, 93 (IEEE, 1998).

- ¹¹³ J.C. Burfoot and G.W. Taylor, *Polar Dielectrics and Their Applications*. London, Macmillan 1979.
- ¹¹⁴ M. Hoffmann, D. Bolten, U. Hasenkox, O. Lohse, and R. Waser, *Integr. Ferroelectr.* **26**, 331 (1999).
- ¹¹⁵ O. Lohse, D. Bolten, M. Grossmann, R. Waser, W. Hartner, and G. Schindler, *Mater. Res. Soc. Symp.* **493** (*Ferroelectric Thin Films VI*), 267 (1998).
- ¹¹⁶ A. Amin, M.J. Haun, B. Badger, H. McKinstry, and L.E. Cross, *Ferroelectr.* **65**, 107 (1985).
- ¹¹⁷ S.E. Park, S. Wada, L.E. Cross, and T.R. Shrout, *J. Appl. Phys.* **86**, 2746 (1999).
- ¹¹⁸ A. Gruverman, A. Pignolet, K.M. Satyalakshmi, M. Alexe, N.D. Zakharov, and D. Hesse, *Appl. Phys. Lett.* **76**, 106 (2000).
- ¹¹⁹ X. Du, U. Belegundu, and K. Uchino, *Jpn. J. Appl. Phys.* **36** Part 1, 5580 (1997).
- ¹²⁰ J.F. Scott and C.A. Paz de Araujo, *Science* **246**, 1400 (1989).
- ¹²¹ E.L. Colla, A.K. Tagantsev, D.V. Taylor, and A.L. Kholkin, *Integr. Ferroel.* **18**, 19 (1997).
- ¹²² M. Grossmann, D. Bolten, O. Lohse, U. Boettger, R. Waser, and S. Tiedke, *Appl. Phys Lett.* **77**, 1894 (2000).
- ¹²³ J.M. Bell, P.C. Knight, and G.R. Johnston, page 93 in: *Ferroelectricity and related phenomena*, Vol. 10 (*Integrated ferroelectric devices and technologies*). Part 1: *Ferroelectric thin films: synthesis and basic properties*. Eds. C. Paz de Araujo, J.F. Scott, and G.W. Taylor. Gordon and Breach, Amsterdam 1996.
- ¹²⁴ C.A. Paz de Araujo, J.D. Cuchiaro, L.D. McMillan, M.C. Scott, and J.F. Scott, *Nature* **374**, 627 (1995).
- ¹²⁵ P.C. Fazan, *Integr. Ferroelectr.* **4**, 247 (1994).
- ¹²⁶ H.N. Lee, Y.T. Kim, and S.H. Choh, *Ferroelectr.* **197**, 733 (1997).
- ¹²⁷ R. Ramesh, A. Inam, W.K. Chan, B. Wilkens, K. Myers, K. Reimann, D.L. Hart, and J.M. Tarascon, *Science* **252**, 944 (1991).
- ¹²⁸ V.Ya. Shur, N.Yu. Ponomarev, N.A. Tonkacheva, S.D. Makarov, E.V. Nikolaeva, E.I. Shishkin, L.A. Suslov, N.N. Salashchenko, and E.B. Klyuenkov, *Phys. Solid State* **39**, 609 (1997).
- ¹²⁹ Q.Y. Jiang, E.C. Subbarao, and L.E. Cross, *J. Appl. Phys.* **75**, 7433 (1994).
- ¹³⁰ J.J. Lee, C.L. Thio, and S.B. Desu, *Physica Status Solidi A* **151**, 171 (1995).
- ¹³¹ B. Aurivillius, *Arkiv Kemi* **1**, 463 (1949)
- ¹³² G.A. Smolenskii, V.A. Isupov, A.I. Agranovskaya, *Sov. Phys. Solid State* **3**, 651 (1961).
- ¹³³ E.C. Subbarao, *J. Phys. Chem. Solids* **23**, 665 (1962).
- ¹³⁴ E.C. Subbarao, *Phys. Rev.* **122**, 804 (1961).
- ¹³⁵ L.G. Van Uitert and L. Egerton, *J. Appl. Phys.* **32**, 959 (1961).
- ¹³⁶ R.E. Newnham, R.W. Wolfe, and J.F. Dorrian, *Mater. Res. Bull.* **6**, 1029 (1971).
- ¹³⁷ R.E. Newnham, R.W. Wolfe, R.S. Horsey, F.A. Diaz-Colon, and M.I. Kay, *Mater. Res. Bull.* **8**, 1183 (1973).
- ¹³⁸ Y. Shimakawa, Y. Kubo, Y. Nakagawa, T. Kamiyama, H. Asano, and F. Izumi, *Appl. Phys. Lett.* **74**, 1904 (1999).
- ¹³⁹ H. Tabata, T. Yanagita, and T. Kawai, *IEICE Trans. Electron.* **E81-C**, 566 (1998).
- ¹⁴⁰ S.K. Kim, M. Miyayama, and H. Yanagida, *J. Ceram. Soc. Japan* **102**, 722 (1994).
- ¹⁴¹ M. Tachiki, K. Yamamuro, and T. Kobayashi, *Mater. Sci. Eng. B* **41**, 131 (1996).
- ¹⁴² T. Takenaka, K. Sakata, and K. Toda, *Jpn. J. Appl. Phys.* **24**, 730 (1985).
- ¹⁴³ A.R. James, A. Pignolet, D. Hesse, and U. Gösele, *J. Appl. Phys.* **87**, 2825 (2000).

- ¹⁴⁴ A. Pignolet, K.M. Satyalakshmi, M. Alexe, N.D. Zakharov, C. Harnagea, St. Senz, D. Hesse, and U. Gösele, *Integr. Ferroelectr.* **26**, 21 (1999).
- ¹⁴⁵ K.M. Satyalakshmi, M. Alexe, A. Pignolet, N.D. Zakharov, C. Harnagea, S. Senz, and D. Hesse, *Appl. Phys. Lett.* **74**, 603 (1999).
- ¹⁴⁶ J.F. Scott, C.A. Paz de Araujo, L.D. McMillan, H. Yoshimori, H.T. Watanabe, T. Mihara, M. Azuma, T. Ueda, T. Ueda, D. Ueda, and G. Kano, *Ferroelectr.* **133**, 47 (1992).
- ¹⁴⁷ A. Gruverman, *Appl. Phys. Lett.* **75**, 1452, (1999).
- ¹⁴⁸ G.D. Hu, J.B. Xu, and I.H. Wilson, *Appl. Phys. Lett.* **75**, 1610 (1999).
- ¹⁴⁹ A. Gruverman, A. Pignolet, K.M. Satyalakshmi, M. Alexe, N.D. Zakharov, and D. Hesse, *Appl. Phys. Lett.* **76**, 106, (2000).
- ¹⁵⁰ I.P. Batra, P. Würfel, B.D. Silverman, *Phys. Rev. Lett.* **30**, 384 (1973); I.P. Batra, P. Würfel, B.D. Silverman, *J. Vac. Sci. Technol.* **10**, 687 (1973).
- ¹⁵¹ J. Zhu, X. Zhang, Y. Zhu, and S.B. Desu, *J. Appl. Phys.* **83**, 1610 (1998).
- ¹⁵² C.L. Canedy, Hao Li, S.P. Alpay, L. Salamanca-Riba, A.L. Roytburd, and R. Ramesh, *Appl. Phys. Lett.* **77**, 1695 (2000).
- ¹⁵³ S.B. Ren, C.J. Lu, J.S. Liu, H.M. Shen, and Y.N. Wang, *Phys. Rev. B* **54**, 14337 (1996).
- ¹⁵⁴ Xin Liang Lu and David A. Payne, "Structure-property relationships for single crystal strontium bismuth tantalate", presented at *7th International Conference on Electronic Ceramics and Their Applications*. (Electroceramics VII – 2000, Sept. 3 - 6, 2000 in Portorož, Slovenia).
- ¹⁵⁵ S.-K. Kim, M. Miyayama, and H. Yanagida, *J. Ceram. Soc. Jap.* **102**, 722 (1994).
- ¹⁵⁶ S.E. Cummins and L.E. Cross, *J. Appl. Phys.* **39**, 2268 (1968).
- ¹⁵⁷ A. Pignolet, C. Harnagea, A.R. James, S. Senz, N.D. Zakharov, and D. Hesse, *Mater. Res. Soc. Symp. Proc.* **596**, (*Ferroelectric Thin Films VIII*), 415 (2000).
- ¹⁵⁸ K. Franke, H. Huelz, and M. Weihnacht, *Surf. Sci.* **416**, 59 (1998).
- ¹⁵⁹ A. Sa Neto and L.E. Cross, *J. Mater. Sci.* **17**, 1409 (1982).
- ¹⁶⁰ K. Abe, S. Komatsu, N. Yanase, K. Sano, and T. Kawakubo, *Jpn. J. Appl. Phys.* **36**, 5846 (1997).
- ¹⁶¹ J. Lee, R. Ramesh, V.G. Keramidas, W.L. Warren, G.E. Pike, and J.T. Evans Jr., *Appl. Phys. Lett.* **66**, 1337 (1995).
- ¹⁶² J. Lee and R. Ramesh, *Appl. Phys. Lett.* **68**, 484 (1996).
- ¹⁶³ Radiant Technologies Inc., RT66A Standardized ferroelectric test system V2.1 operating manual.
- ¹⁶⁴ W.L. Warren, H.N. Al-Shareef, D. Dimos, B.A. Tuttle, and G.E. Pike, *Appl. Phys. Lett.* **68**, 1681 (1996).
- ¹⁶⁵ E.L. Colla, A.L. Kholkin, D. Taylor, A.K. Tagantsev, K.G. Brooks, and N. Setter, *Microelectron. Eng.* **29**, 145 (1995).
- ¹⁶⁶ S. Hong, E.L. Colla, E. Kim, D.V. Taylor, A.K. Tagantsev, P. Muralt, K. No, and N. Setter, *J. Appl. Phys.* **86**, 609 (1999).
- ¹⁶⁷ C. Harnagea, A. Pignolet, M. Alexe, D. Hesse, and U. Gösele, *Mater. Res. Soc. Symp. Proc.* **596** (*Ferroelectric Thin Films VIII*), 351 (2000).
- ¹⁶⁸ M. Abplanalp and P. Günter, *Proc. of 11th IEEE-ISAF (Montreux, Aug. 24-27, 1998)*, Cat. No. 98CH36245, 423 (IEEE 1998).
- ¹⁶⁹ C. S. Ganpule, V. Nagarajan, H. Li, A. S. Ogale, D. E. Steinhauer, S. Aggarwal, E. Williams, R. Ramesh, and P. De Wolf, *Appl. Phys. Lett.* **77**, 292 (2000).
- ¹⁷⁰ D. Ricinchi, C. Harnagea, C. Papusoi, L. Mitoseriu, V. Tura, and M. Okuyama, *J. Phys.: Condens. Matter* **10**, 477 (1998).

-
- ¹⁷¹ D. Ricinschi, C. Harnagea, and M. Okuyama, *Ferroelectr.* **219**, 225 (1998).
V. Tura, D. Ricinschi, L. Mitoseriu, C. Harnagea, S. Ando, T. Tsukamoto, and M. Okuyama, *Jpn. J. Appl. Phys.* **36**, 2183 (1997).
- ¹⁷² B. Jaffe, W.R. Cook, and H. Jaffe, *Piezoelectric ceramics*. Academic Press, London 1971.
- ¹⁷³ M.A. Dubois, P. Muralt, D.V. Taylor, and St. Hiboux, *Integr. Ferroelectr.* **22**, 535 (1998).
- ¹⁷⁴ X.-H. Du, Q.-M. Wang, U. Belegundu, A. Bhalla, and K. Uchino, *Mater. Lett.* **40**, 109 (1999).
- ¹⁷⁵ Y. Saya, S. Watanabe, M. Kawai, H. Yamada, and K. Matsushige, *Jpn. J. Appl. Phys.* **39**, 3799 (2000).
- ¹⁷⁶ W.L. Warren, D. Dimos, G.E. Pike, B.A. Tuttle, M.V. Raymond, R. Ramesh, and J. T. Evans, Jr., *Appl. Phys. Lett.* **67**, 866 (1995).
- ¹⁷⁷ O.N. Tufte and P.W. Chapman, *Phys. Rev.* **155**, 796 (1967).
- ¹⁷⁸ R. Waser and M. Klee, *Integr. Ferroelectr.* **2**, 23 (1992).
- ¹⁷⁹ J. Lee, C.H. Choi, B.H. Park, T.W. Noh, and J.K. Lee, *Appl. Phys. Lett.* **72**, 3380 (1998).
- ¹⁸⁰ G.E. Pike, W.L. Warren, D. Dimos, B.A. Tuttle, R. Ramesh, J. Lee, V. G. Keramidas, and J.T. Evans, Jr., *Appl. Phys. Lett.* **66**, 484 (1995).
- ¹⁸¹ For example, J.D. Jackson, *Classical Electrodynamics*, 3rd ed., Wiley, New York 1999.
- ¹⁸² X. Du, U. Belegundu, and K. Uchino, *Jpn. J. Appl. Phys.* **36**, Part 1, 5580 (1997).
- ¹⁸³ K. Lefki and G.J.M. Dormans, *J. Appl. Phys.* **76**, 1764 (1994).

Lebenslauf

Catalin HARNAGEA, B.Sc., M.Sc.

An der Uferstraße 7

06120 Halle (Saale)

verheiratet, 1 Kind

22. 09.1970	Geboren in Iasi (Rumänien)
1977 bis 1985	Besuch der Grundschule Nr. 22 in Iasi
1985 bis 1989	Besuch des Gymnasiums „National-Hochschule“ in Iasi
Juni 1989	Abschluß der Schulausbildung mit dem Abitur
1989 bis 1990	Ableistung des Grundwehrdienstes
1990 bis 1995	Studium im Fach <i>Physik</i> an der Universität „Alexandru Ioan Cuza“ in Iasi
Juni 1995	Diplomprüfung
1995 bis 1996	Magister-Studium im Fach <i>Elektrische und magnetische Eigenschaften der feinen und ultrafeinen Strukturen</i> an der Universität „Alexandru Ioan Cuza“ Iasi
Juni 1996	Magisterprüfung
1996 bis 1997	Physik-Lehrer im „Emil Racovita“ Gymnasium in Iasi
November 1997	Beginn einer Promotionsarbeit in der Abteilung von Prof. Dr. U. Gösele am Max-Planck-Institut für Mikrostrukturphysik in Halle (Saale)

Eidesstattliche Erklärung

Hiermit versichere ich, die vorliegende Dissertation

*Local piezoelectric response and domain structures in
ferroelectric thin films
investigated by voltage-modulated force microscopy*

selbständig verfaßt und keine anderen als die von mir angegebenen Quellen und Hilfsmittel verwendet zu haben. Den benutzten Werken wörtlich oder inhaltlich entnommene Stellen sind als solche gekennzeichnet.

Halle, den 6. Dezember 2000



Catalin HARNAGEA

Acknowledgement

My work at the Max-Planck-Institut für Mikrostrukturphysik was made possible by Professor Gösele to whom I am grateful for his constant encouragement, for his confidence and continuous support that allowed me to enter the Ferroelectric World.

One of my big chances during the Ph.D. work was to be under the leadership of Priv. Doz. Dr. Hesse, whose supervision extended much over the professional limits. His guidance, as well as the valuable help in solving organizational problems are highly appreciated.

I have been fortunate to have Dr. A. Pignolet and Dr. M. Alexe as advisors throughout the whole work. First, their important role in introducing me into this hot research topic, as well as their help in setting up the experiment and their continuous support are highly acknowledged. Second, I am grateful for their time spent during the long discussions that materialized in most of the ideas and interpretations of the experimental results.

Definitely, the present work benefited from the good quality of the epitaxial films made by the other group members including Dr. K. M. Satyalakshmi. The interpretation of the piezoresponse in epitaxial films would have not been possible without the XRD and TEM analyses that were made possible through the work of Dr. S. Senz, Dr. N.D. Zakharov and Dr. C. Schäfer.

I would like to thank Prof. L. Eng (TU Dresden) for his helpful suggestions, as well as Dr. L. Mitoseriu, Dr. V. Tura, Professor C. Papusoi and Professor A. Stancu (“Al. I. Cuza” University of Iasi) and Mr. D. Ricinschi (University of Osaka) for fruitful discussions and encouragement.

Last but not least, a special gratitude to my wife Hermina, for her patience, her enthusiastic support and her continuous understanding.

List of publications in the field of the thesis

(reverse chronological order)

1. D. Hesse, H.N. Lee, A. Pignolet, N.D. Zakharov, C. Harnagea, and S. Senz
Microstructure and properties of epitaxial ferroelectric bismuth-layered perovskite thin films grown on Si(001) with a polarization component perpendicular to the film plane
(accepted) Proceedings of ISAF 2000, Hawaii, July 30 - August 2, 2000.
2. M. Alexe, C. Harnagea, A. Visinoiu, D. Hesse, and U. Gösele
Patterning and switching of nano-size ferroelectric memory cells
(Submitted as invited paper to) 5th International Conference on Nanostructured Materials, NANO 2000 Sendai, Japan, August 20th – 25th 2000.
3. H. N. Lee, S. Senz, N.D. Zakharov, C. Harnagea, A. Pignolet, D. Hesse, and U. Gösele
Growth and characterization of non-c-oriented epitaxial ferroelectric SrBi₂Ta₂O₉ films on buffered Si(110)
Appl. Phys. Lett. **77** (20), 3260 (2000).
4. H. N. Lee, A. Visinoiu, S. Senz, C. Harnagea, A. Pignolet, D. Hesse, and U. Gösele
Structural and electrical anisotropy of (001)-, (116)-, and (103)-oriented epitaxial SrBi₂Ta₂O₉ thin films on SrTiO₃ substrates grown by pulsed laser deposition
J. Appl. Phys. **88** (11), 6658-6664 (2000).
5. Marin Alexe, Catalin Harnagea und Dietrich Hesse
Nano-Engineering fuer ferroelektrische Speicher
Neue Methoden der Mikrostrukturphysik ermoeglichen Fortschritte bei Nichtfluessigen ferroelektrischen Speicherbauelementen
Physikalische Blaetter **56** (10), 47 (2000).
6. C. Harnagea, A. Pignolet, M. Alexe, D. Hesse, and U. Gösele
Domain imaging, polarization hysteresis and switching in nano-size ferroelectric structures
Mater. Res. Soc. Symp. Proc. **596** (Ferroelectric thin films VIII), 351 (2000).
7. A. Pignolet, C. Harnagea, A.R. James, S. Senz, N.D. Zakharov, and D. Hesse
Structure-property relationships of epitaxial ferroelectric thin films of various bismuth-layered perovskites with even and odd Aurivillius parameters
Mater. Res. Soc. Symp. Proc. **596** (Ferroelectric thin films VIII), 415-426 (2000).
8. C. Harnagea, A. Pignolet, M. Alexe, D. Hesse, and U. Gösele:
Quantitative ferroelectric characterization of single submicron grains in Bi-layered perovskite thin films,
Appl.Phys. A **70** (3), 261 (2000).

9. A. Pignolet, C. Schäfer, K.M. Satyalakshmi, C. Harnagea, D. Hesse, and U. Gösele:
Orientation dependence of ferroelectricity in pulsed laser deposited epitaxial bismuth-layered perovskite thin films,
Appl.Phys. A **70** (3), 283 (2000).
10. M. Alexe, C. Harnagea, W. Erfurth, D. Hesse and U. Gösele:
100 nm lateral size ferroelectric memory cells fabricated by electron beam direct writing,
Appl.Phys. A **70** (3), 247 (2000).
11. C. Harnagea, M. Alexe, A. Pignolet, K.M. Satyalakshmi, D. Hesse and U. Gösele:
Switching of ferroelectric nanostructures
In: "Piezoelectric Materials: Advances in Science, Technology and Applications"
eds: C. Galassi, M. Dinescu, K. Uchino, and M. Sayer. NATO Science Series
No.3 - High Technology, vol. 76, p. 169, Kluwer Academic Publishers, Dordrecht,
Boston, London 2000.
12. M. Alexe, C. Harnagea, A. Pignolet, D. Hesse, and U. Gösele:
Nano-size ferroelectric structures
In: "Piezoelectric Materials: Advances in Science, Technology and Applications"
eds: C. Galassi, M. Dinescu, K. Uchino, and M. Sayer. NATO Science Series
No.3 - High Technology, vol. 76, p. 49, Kluwer Academic Publishers, Dordrecht,
Boston, London 2000.
13. V. Tura, L. Mitoseriu, C. Harnagea, and D. Ricinschi:
Ferroelectricity in (Hf, Zr)-doped barium titanate ceramics
Ferroelectr. **239** (1-4), 265 (2000).
14. L. Mitoseriu, V. Tura, D. Ricinschi, and C. Harnagea:
Grain-size dependence of the Rayleigh coefficients of barium titanate ceramics,
Ferroelectr. **240** (1-4), 1317 (2000).
15. C. Harnagea, A. Pignolet, M. Alexe, K.M. Satyalakshmi, D. Hesse, and U. Gösele:
Nanoscale switching and domain structure of ferroelectric BaBi4Ti4O15 thin films
Jpn. J. Appl. Phys. **38** (11A), L1255 (1999).
16. M. Alexe, C. Harnagea, D. Hesse, and U. Gösele:
Patterning and switching of nano-size ferroelectric memory cells
Appl. Phys. Lett. **75** (12), 1793 (1999).
17. M. Alexe, A. Gruvermann, C. Harnagea, N.D. Zakharov, A. Pignolet, D. Hesse, and J.F. Scott:
Switching properties of self-assembled ferroelectric memory cells
Appl. Phys. Lett. **75** (8), 1158 (1999).
18. K.M. Satyalakshmi, A. Pignolet, M. Alexe, N.D. Zakharov, C. Harnagea, S. Senz, S. Reichelt, D. Hesse, and U. Gösele:

All epitaxial BaBi₄Ti₄O₁₅ - LaNiO₃ heterostructures
Mater. Res. Soc. Symp. Proc. **541** (*Ferroelectric thin films VII*), 205 (1999).

19. A. Pignolet, K. M. Satyalakshmi, M. Alexe, N. D. Zakharov, C. Harnagea, S. Senz, D. Hesse, and U. Gösele,
Epitaxial bismuth-layer-structured perovskite ferroelectric thin films grown by pulsed laser deposition
Integr. Ferroel. **26** (1-4), 21 (1999).
20. K.M. Satyalakshmi, M. Alexe, A. Pignolet, N.D. Zakharov, C. Harnagea, S. Senz, and D. Hesse:
BaBi₄Ti₄O₁₅ ferroelectric thin films grown by pulsed laser deposition
Appl. Phys. Lett. **74** (4), 603 (1999).
21. L. Mitoseriu, D. Ricinschi, C. Harnagea, and V. Tura:
Grain size effects on the polarization reversal process in ferroelectric ceramics
Balkan Phys. Lett. **6** (4), 277 (1998).
22. D. Ricinschi, C. Harnagea, and M. Okuyama:
Grain size-dependent switching in barium titanate ferroelectric ceramics analyzed by means of their Landau coefficients
Ferroelectrics **219** (1-4), 225 (1998).
23. Ricinschi, C. Harnagea, C. Papusoi, L. Mitoseriu, V. Tura, and M. Okuyama:
Analysis of ferroelectric switching in finite media as a Landau-type phase transition,
J. Phys.: Condens. Matter **10** (2), 477 (1998).
24. Tura, D. Ricinschi, L. Mitoseriu, C. Harnagea, S. Ando, T. Tsukamoto, and M. Okuyama:
Simulation of switching properties of ferroelectrics on the basis of dipole lattice model,
Jpn. J. Appl. Phys. **36** (4A) 2183 (1997).
25. Mitoseriu, D. Ricinschi, C. Harnagea, M. Okuyama, T. Tsukamoto, and V. Tura:
Grain Size Dependence of Switching Properties of Ferroelectric BaTiO₃ Ceramics,
Jpn. J. Appl. Phys **35** (9B) 5210 (1996).
26. L. Mitoseriu, V. Tura, C. Papusoi, D. Ricinschi, and C. Harnagea:
Thermal Dependences of the Switching Properties of Barium Titanate Ceramics,
Mater. Lett. **29** (1-3), 25 (1996).